# DESIGN OF WIDEBAND ON-BOARD TERAHERTZ INTERCONNECTS, CIRCUITS AND SENSORS

By

Jennifer Anne Byford

A DISSERTATION

Submitted to
Michigan State University
in partial fulfillment of the requirements
for the degree of

Electrical Engineering – Doctor of Philosophy

2018

# ABSTRACT

## DESIGN OF WIDEBAND ON-BOARD TERAHERTZ INTERCONNECTS, CIRCUITS AND SENSORS

By

Jennifer Anne Byford

With the advent of better terahertz (THz) sources and detectors in the last few decades this frequency range has increasingly been investigated to provide solutions in fields such as nondestructive evaluation, security imaging, health monitoring, biological tissues and sample inspection, and electronic circuits and systems. THz radiation holds great potential for these varied applications because it is non-ionizing, or safe for use with biological tissues, and because it offers the highest frequencies and largest bandwidth while still accommodating all electrical solutions (i.e. non-optical). One of the building blocks in using THz radiation in such applications is having a low-loss, ultra-wide bandwidth waveguide, or interconnect, with which to connect other circuits into a larger system.

Current trends in data consumption are driving a need to further increase the rate and bandwidth at which common electrical devices transmit data. Many solutions have been proposed using optical and electrical interconnects to address this problem but an ideal solution has yet to be realized. This is primarily due to optical interconnects inherent latency in needing to convert between electrical and optical signals, and because electrical solutions either suffer from metal losses, crosstalk, or narrow bandwidth. In this thesis a waveguide design is proposed as a possible solution to address this need that combines the design of a traditional metal waveguide and that of a ribbon waveguide.

Theoretical analysis, simulations, fabrication, and measured results are presented for waveguides of both a circular and rectangular cross-section. Theoretical expressions have been derived by hand and simulations were performed using finite element tool ANSYS Electronics Desktop HFSS® to create and simulate waveguide models. Fabrication processes used here have utilized 3D printed plastics to quickly and inexpensively create prototypes, and a frequency domain THz system was used to measure devices. Results show low-loss transmission up to 0.5 THz. Applications for passive THz components, sensors, and transmission line circuits are explored. This work includes additional circuits the waveguide design can be extended to including a power splitter, band-pass and band-stop filters, and a modified version of a dielectric rod antenna. Sensor applications are shown through a probe design and demonstrating how imaging could be performed with the probe. This work has implications for future integrated circuits ability in meeting the data transmission needs of the future.

To the memory of my Busha, Joanne Byford.

# ACKNOWLEDGMENTS

I started as an undergraduate freshman here at Michigan State in 2009 and as a graduate student in 2014. Even before stepping foot as an official student on campus MSU has long been a part of my family as I am a third generation Spartan and grew up in the Lansing area. Now that my formal education has come to a close I would like to acknowledge the many people who have helped me get here.

I would like to thank, first and foremost, Dr. Premjeet Chahal. He was my first introduction to Electromagnetics in ECE 305 and I have been working and studying with him ever since. He has provided a tremendous amount of his time, guidance, and advice to me all of which I have tried my best to take and greatly appreciate. He has always given me the time and encouragement to pursue my interests which I am so thankful for.

I am also thankful for the help of my other committee members Dr. Edward J. Rothwell, Dr. Shanker Balasubramaniam, Dr. Christina Chan, and Dr. Robert McGough. I am especially grateful for Ed and Shanker who I've taken a great deal of EM courses with, had give me lots of additional guidance on my research and advice for my future professional plans. Everything I know about Electromagnetics I've learned from Prem, Ed, and Shanker. Together they have pushed me technically and professionally and I will always be grateful.

I would like to thank the many people in the Department of Electrical and Computer Engineering, College of Engineering, and the Graduate School at MSU for helping me secure travel funding for conferences, receive scholarships and fellowships for much of my graduate funding, and for coordinating workshops and programs that really helped my transition to graduate school and the pursuit of my professional development so much easier. Specifically I'd like to thank Dr. Katy Luchini Colbry for helping me navigate the graduate school application process and for creating and running many of the programs in the college that help students, to Dr. Percy Pierre who brought me into the Alfred Sloan scholars student group and helped secure funding for my studies many semesters, Dr. Tim Hogan for being a friendly and helpful point of contact for the ECE Department

when I was leadership in LEEGS, on the graduate studies committee or for my own individual issues, to the FAST Fellowship Steering Committee who were all amazing and helped me learn and grow so much as an educator. Also a huge thanks and recognition is owed to the ECE Shop technicians Gregg Mulder and Brian Wright without whom, I would never have been able to make almost anything presented (or not) in this thesis.

I would like to thank my fellow (and alumni) members of the Electromagnetics Research Group. My colleagues taught me how to do everything around the lab and their friendships have been very meaningful and made most of graduate school actually fun. I am especially indebted to former members Dr. Kyoung Youl Park and Dr. Nophadon Wiwatcharagoses who trained and taught me as an undergrad and really allowed me to integrate into the group. Saranraj Karuppuswami, Chris Oakley, Michael Craton, Vinny Gjokaj, John Doroshewitz, Zane Crawford, Scott O'Connor, Ifwat Ghazali, Aman Kaur, Saikat Mondal, Pratik Chatterjee, Yuxiao He, Stavros Vakalis, Serge Mghabghab, Sean Ellison, Billy Stevers, Nithya Krithi, and everyone else who has passed through the EMRG while I've been here, you have all been great friends and colleagues and I look forward to seeing all the great things you do! Thank you all so much.

Finally I would like to thank my family, my parents Karen and Mark Byford as well as my brother Greg Byford. They have provided invaluable lifelong support and sacrifice for which I am deeply grateful.

## TABLE OF CONTENTS

# LIST OF TABLES

# LIST OF FIGURES

# CHAPTER 1

# INTRODUCTION

## 1.1 Terahertz overview

### 1.1.1 Definition

The work in this thesis is primarily targeting the terahertz (THz) frequency range which acts as a divide between electronics and optics on the familiar “electromagnetic spectrum” diagram, a version of which can be seen in Figure 1.1. At its broadest definition the THz range is defined as frequencies from 0.1 to 10 THz (which would be $10^{11}$ to $10^{13}$ cycles per second). Although in the literature it is increasingly being defined as 0.3 to 3 THz, as this range corresponds to the submillimeter wavelength band, defined as a wavelength ($\lambda$) of 1 mm to 100 µm.

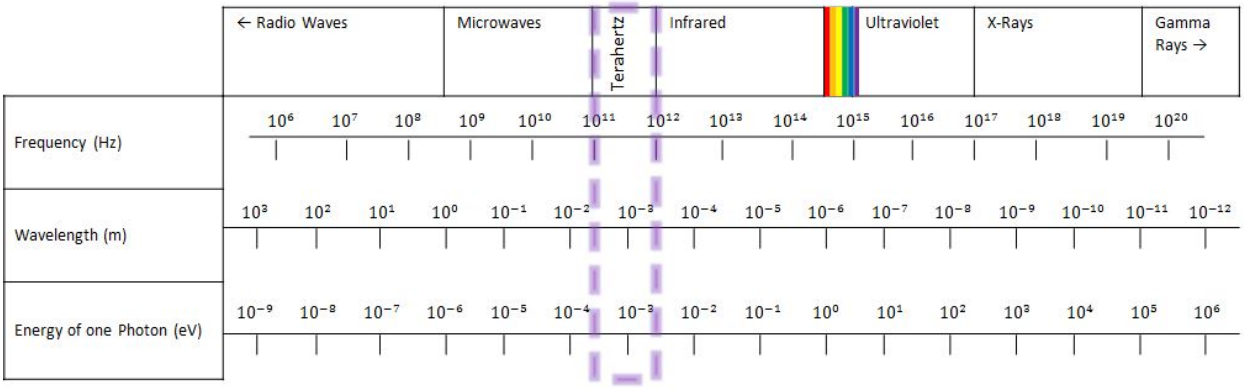

Figure 1.1: A diagram illustrating the electromagnetic spectrum, showing which parts correspond to which frequencies, wavelengths, and energies.

Given where the THz range falls in the electromagnetic spectrum, the energy levels of the radiation in the range are very low, on the scale of milli-electron volts. For example, there is an energy of only 4 meV at 1 THz, as indicated in Figure 1.1, making it non-ionizing and therefore non-damaging to biological tissues or cells. This would, importantly, include the safety of human tissues and cells which makes it a possible frequency range for medical applications. THz waves also have a longer wavelength than other regions used for imaging, such as infrared or optical wavelengths, which makes it able to have a greater penetration depth and be less susceptible to the effects of scattering. As compared to optical or infrared wavelengths which would suffer greatly from Rayleigh scattering, THz wavelengths would only be affected by Mie or Tyndall scattering which is much less severe. Lastly, the THz region is very spectrally rich and excites intermolecular vibrations in many molecules. These interactions allow many substances to have a unique fingerprint in this region which can make characterization and identification of substances much easier than in other frequency regions.

### 1.1.2 Applications

Due to these properties, to date, much of the research using THz radiation has focused on imaging and spectroscopy. However, trends in consumer and non-consumer electronics have led to an emerging need for THz technology to be applied to electronic circuits, systems, and packaging. In this field, THz designed components could provide a path for wide-bandwidth, high-speed circuits that still provide an all electrical solution to modern electronics needs.

Although THz radiation use has expanded into many fields and applications, here, a few examples of its main applications will be briefly covered for the purposes of providing the reader with context into where the work presented in this thesis fits into an overall larger THz research field. An overview of the majority of THz research and applications are in the fields of spectroscopy and medical imaging which will first be covered, then, the more emerging areas of nondestructive evaluation (NDE) and circuits and systems.

#### 1.1.2.1 Spectroscopy

Spectroscopy near the infrared range became possible, and has subsequently been pursued in research, starting in the 1950's with the advent of Fourier transform infrared (FTIR) spectroscopy. FTIR determines a spectrum by taking the Fourier transform of an interferogram, the record produced by a two beam interferometer as the path difference between the beams is varied from zero to some arbitrary maximum value [3]. The very first spectra investigated with FTIR were stellar spectra and the technique's application has endured to investigate solar, planetary, and chemical absorption spectra [4].

However, the development of the femtosecond laser in 1989, as first described in [5], is what truly granted access to the THz range. This technique used the optical excitation of photoconductive antennas (or switches) to generate THz transient radiation as is discussed in more detail later in Section 1.1.3, an excellent overview of the technology can by found in [6], and an extensive overview in [7]. This difference of technique to observe samples within the THz range (THz spectroscopy) as opposed to the infrared range (FTIR) is most distinct in the ability to observe intermolecular vibrations of chemicals and molecules where their intramolecular mode appears in the infrared region [8].

THz spectroscopy has been used to obtain chemical and structural information about concealed substances such as in [9] where its use to detect illicit drugs and various explosives was investigated. Here, the difference between even very similar substances such as cocain free base and cocaine hydrochloride, "crack" and "coke" respectively, can be seen in their spectral signatures.

Spectroscopic information in the THz range can also be applied to deoxyribose nucleic acid (DNA). It has been shown that for the four nucleobases and their corresponding nucleosides a distinct pattern of vibrational motion resonances can be identified between 0.5 to 3.5 THz [10]. This sort of information is not only important for understanding the nature of the bonds between these molecules but it also reveals information about their molecular conformation (spatial arrangement) as well.

Application of this technology has also been applied to art conservation and determining authenticity. THz spectroscopy can be used to determine artists materials as most pigments and some synthetic polymers have spectral fingerprints in the THz regime [11]. Due to this, it can be used for the purposes of conserving art by being able to distinguish what materials were used and boundaries between pigments [12].

#### 1.1.2.2 Medical imaging

In addition to being nonionizing another key benefit to THz radiation is the amount it can penetrate a biological sample for the specific application of biomedical imaging for use with human (or animal) subjects. Although spatial resolution is important for the level of detail that can be achieved the penetration depth is even more key for *in vivo* imaging since this limits what areas of the body can be imaged. It has been reported that a terahertz pulse can be detected through 1.5 mm of human skin [13] but more realistic results have shown depths of 82 µm at 1 THz [14]. The epidermis (topmost layer) ranges from 0.5 mm thickness on eyelids to 1.5 mm on the palms of hands, the dermis (middle layer) varies from about 0.3 mm on eyelids to 3 mm on the shoulder blade area and the hypodermis (lowermost layer of skin) is either negligible or somewhat indeterminable since it is mixed in with the underlying adipose (fat) layer and blood veins. The typical thickness of the whole skin around the body is around 0.7-0.9 mm [15] - [16]. THz radiation has consistently shown the ability to fully penetrate the epidermis and often the upper region of the dermis. Given that the average depth of the epidermis is 82 µm and the measured depth of THz radiation at 1 THz is also about 82 µm these results make sense and show that THz is best suited for interrogating the upper layers of skin.

As shown in results from [17], THz has the capability to interrogate much of human skin showing notable pulse strength well into the epidermis. THz radiation has also been demonstrated to be useful for, due to the high penetration depth achieved in adipose (fat) samples, intra-operative imaging for breast cancers, the breast being effectively all adipose tissue [18]-[19].

Overall THz imaging capabilities have resolutions that are competitive with other established medical imaging methods and have a penetration depth into human tissues that is both deep enough to resolve skin level ailments and is unique to that frequency band. No other imaging method or frequency range can image so well at such shallow depths. This allows for many applications such as the noninvasive imaging of basal cell carcinoma [20, 21], squamous cell carcinoma [22], skin level ailments like psoriasis [23], monitoring topical drug penetration [24] and characterizing burn wounds [25, 26, 27, 28].

#### 1.1.2.3 Non-destructive evaluation

Non-destructive evaluation (NDE) is the study of analysis techniques which are used to evaluate the properties of a material, components, or system without causing damage to the sample under test or needing to disassemble it. Similar to how human medicine uses imaging techniques like magnetic resonance imaging (MRI) or computed tomography (CT) scans to determine root failures in human health instead of performing "exploratory surgeries" advancements in this area are very important for being able to quickly and harmlessly investigate non-biological samples. Many materials such as commonly used in clothing or food packaging are effectively transparent to THz radiation which has allowed it to be a useful tool for expanding the NDE area.

THz time domain spectroscopy has been used to determine the properties of materials which are relevant to the electronics packaging industry. It has been shown useful to investigate silicon semiconductor wafers determining properties such as mobility and conductivity [29]. A wide variety of polymer-ceramic composite dielectric substrates have also been characterized which are commonly used in microstrip based circuit design and fabrication along with many other substrate materials including alumina, high-density polyethylene, and poly(ethylene) terephthalate (PET) [30].

THz-NDE has been used to inspect aircraft composites [31, 32] revealing uneven thicknesses, burns, mechanical stresses, and hidden defeats. THz radiation is also particularly sensitive to moisture and can reveal defeats in corks used to seal liquids [33]. Cork itself is transparent at THz frequencies but if there is a defect present which allows the liquid sample to become exposed to the surrounding environment, or vice versa, using THz imaging such a defect can be exposed. The National Aeronautics and Space Administration (NASA) uses THz radiation to inspect sprayed on foam insulation on space shuttles to detect, for example, voids [34].

Other applications are as varied as inspecting the 3D internal structures of pharmaceutical tablets [35] to detecting foreign bodies in chocolate [36], both of which use a THz pulsed imaging technique in order to retrieve depth information. Overall, THz imaging capabilities paired with the subset of materials transparent to its radiation and its unique sensitivity to moisture provide a powerful tool for NDE.

#### 1.1.2.4 Circuits and systems

THz technology has been applied to a wide variety of areas such as wireless communications, high-speed data processing and satellite communications [8]. THz waves are seen as a competitive solution to broadband wireless communications, especially because many frequency bands above 275 GHz have yet to be allocated at specific active services. Overall, most solutions for signal generation, modulation, and detection have employed photonics technologies in order to push for data rates towards 100 Gb/s [37]. This can be seen in works such as [38] where coherent THz signal transmission is demonstrated using an optical sub-harmonic IQ mixer and optical fiber technologies to realize a high-speed wireless link. Other related works have explored the improvement of subcomponents within such systems such as low-dispersive dielectric mirrors [39]. Even THz integrated CMOS circuits on silicon-based technologies have been proposed [40] including field-effect transistors for the detection of 0.2 - 4.3 THz radiation [41] which are implemented using a 150 nm process technology.

Notably in the works discussed the solutions are all optically based, however, system cost and power efficiency of the entire link for optical solutions remain as major obstacles for optical interconnects in the short to medium range (less than 50 m) due to the large over-head power consumption in the electro-optic converters and high complexity/precision needed for packaging and implementation. For electrical solutions which avoid this problem, the most common interconnect solutions are microstrip based designs. Unfortunately, designing microstrip based circuits in the THz range is nearly impossible due to crippling skin effect losses. The general formula for the skin depth is given in Equation 1.1 although practically is generally abbreviated to only the first radical in the expression as that term tends to dominate. The skin effect describes the behavior of alternating current to generally become distributed within a conductor such that the current density is the largest near the surface of the conductor and decreases with depth. The skin depth, as can be calculated using Equation 1.1, is the depth where the current density is about 37 %, or 1/e where e is the base of the natural logarithm, of the value at the surface. Therefore, over 98 % of the current in a conductor will flow within four skin depths from the conductor surface. However, as can be seen by looking at Equation 1.1, the skin depth and frequency of a signal are inversely proportional, which means at higher frequencies the current is confined to an increasingly smaller volume within the conductor thereby greatly increasing the amount of loss attributed to the conductor.

$$\delta = \sqrt{\frac{2\rho}{\omega\mu}}\sqrt{\sqrt{1+(\rho\omega\epsilon)^2}+\rho\omega\epsilon} \tag{1.1}$$

In Equation 1.1 $\rho$ is the resistivity of the conductor, $\omega$ is the angular frequency of the signal, $\mu$ is the product of the relative magnetic permeability of the conductor and the permeability of free space, and $\epsilon$ is the product of the relative permittivity of the material of the medium and the permittivity of free space. As an example, the skin depth in popular electronics metals have been calculated in Table 1.1 for THz range frequencies using Equation 1.1. From these values it is clear that THz frequencies would remain confined in too small a volume of metal and therefore suffer conductive losses heavily.

| Material | Resistivity ($\Omega\cdot$ m) | $\delta$ at 0.1 THz | $\delta$ at 0.3 THz | $\delta$ at 1 THz |
|---|---|---|---|---|
| Copper (Cu) | $1.68\times10^{-8}$ | 0.203 µm | 0.119 µm | 65.23 nm |
| Silver (Ag) | $1.58\times10^{-8}$ | 0.200 µm | 0.115 µm | 63.26 nm |
| Gold (Au) | $2.44\times10^{-8}$ | 0.248 µm | 0.143 µm | 78.61 nm |

Table 1.1: Skin depths ($\delta$) calculated for THz frequencies.

Microstrips, as well as traditional metal waveguides, also suffer from high dispersion at higher frequencies. There have been a few notable solutions which are compatible with substrate integration that are not microstrip based including the ribbon waveguide and substrate integrated waveguide (SIW) which will be further discussed in Section 1.2.2.

### 1.1.3 Current measurement systems

Because THz frequencies lie between electronics and optics, designing and implementing reliable sources and detectors for these frequencies had remained illusive until the last few decades. Methods from an electronics circuits approach, as are used in the microwave region, could at best cover the lower end of the terahertz region. Photonic approaches, such as using lasers, photoconductive dipole antennas and optical mixing, as are used in the infrared region, can cover the terahertz region much more fully and have been refined greatly over the last two decades. Although research is still continuing in the area of THz sources and detectors, this problem as been solved sufficiently that commercial THz, or “T-ray”, systems are available and research into designing and fabricating electric and photonic devices and applications for THz frequencies has grown.

Instead of using cumbersome equipment like free electron lasers or liquid helium cooled bolometers, solid-state devices operating at room temperature can generate and detect THz waves, a typical frequency domain system setup is depicted in Figure 1.2. Although systems are still relatively expensive, their cost and size has been reduced significantly over time so that they are much more accessible. Two main types of systems are available, continuous wave (CW) or using pulsed lasers, where measurements are taken in the frequency domain or time domain (TD) respectively.

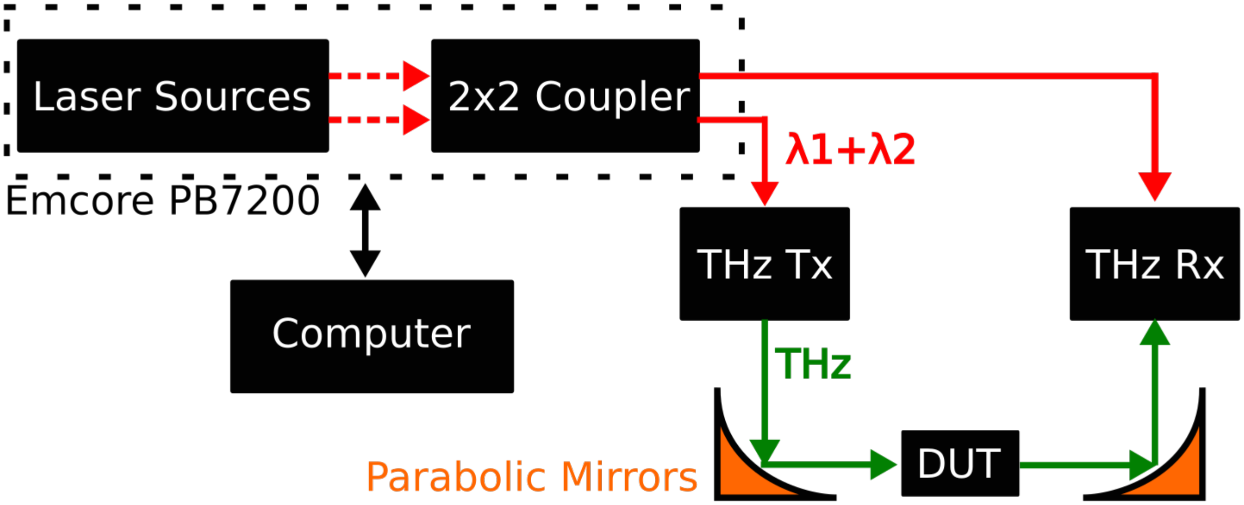

Figure 1.2: A basic diagram of a typical frequency domain THz measurement system. In pulsed laser systems the laser source would typically be a Ti:Sapphire laser and for continuous wave systems, as is shown here, it would be the photomixing of two separate lasers, their difference resulting in a THz wave.

In TD systems terahertz pulses are generated and detected using ultrashort pulsed Ti:Sapphire lasers. These pulses, from around 10 to 100 fs in pulse width with center wavelengths around 800 nm and duration of around 1 ps with a repetition rate of 80 MHz, are used in conjunction with a photoconductive emitter, typically a semiconductor like gallium arsenide, which has two planar metal electrodes. The electrodes are geometrically designed like a dipole antenna and can support a large electric field across their surface. When the Ti:Sapphire laser is focused at the gap between these electrodes the electron-hole pairs generated on the surface of the semiconductor will, effectively, “close the circuit” since a photon from 800 nm light is above the bandgap of gallium arsenide, making the dipole undergo a rapid change in current density. This will produce a THz transient in the antenna which is radiated into free space. This resultant transient can cover a large range of frequencies in the THz region, typically systems have a usable range of 0.1 - 3 THz. These pulsed laser systems give the capability to measure the transient electric field as well as the intensity so that, when a Fourier Transform is taken, both amplitude and phase information is present in order to extract material properties such as the refractive index, absorption coefficient and complex permittivity of samples.

In CW systems photomixing is used between two lasers with identical polarization to generate a THz wave in their beat. Together the lasers are used to illuminate a semiconductor, commonly gallium arsenide, which will result in the modulation of the conductivity at the desired THz frequency. This technique allows for continuous tuning and spectral resolutions of 4 MHz to be achieved [42] which is much better than TD systems whose resolutions are typically closer to 12 GHz.

There are key advantages each system offers, CW systems are less expensive, light weight, less complicated, have more straight forward data interpretation and have acquisition speeds around 25× faster than TD systems. TD systems, however, make much more information available by being spectrally broadband, providing phase and amplitude contrast as well as providing depth profiling capabilities when in reflection mode. Typically TD systems are a better choice when looking to identify unknown substances or objects where CW systems are better for screening items with similar properties [43].

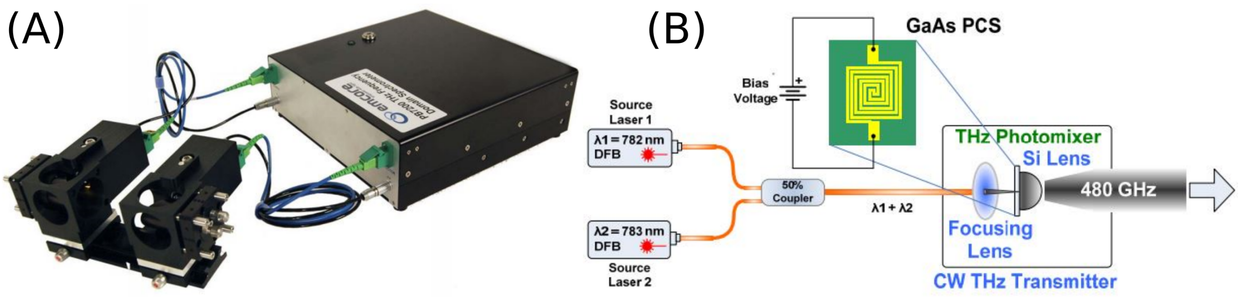

Figure 1.3: The (A) Emcore model PB7200 THz Frequency Domain Spectrometer used in this thesis as well as (B) a block diagram of how it works. Both images are from the user manual [1].

Here in this work a continuous wave THz system is used because it is what is available in our laboratory, specifically, an Emcore model PB7200 THz Frequency Domain Spectrometer which can be seen in Figure 1.3 (A). As can also be seen in Figure 1.3 (B) is a diagram from the instrument user manual [1] of how the photomixing is done in the system to achieve a continuous wave. This system can measure over a frequency range from 0.1 to 1.7 THz with a frequency resolution of 100 MHz. The THz radiation is achieved by combining the output of two single frequency diode lasers to optically excite a photo-conductive switch (PCS). The THz radiation, whose frequency will be at the beat frequency, see Equation 1.2, of the two lasers, is subsequently focused through a silicon lens and reflected off a parabolic mirror to direct a collimated beam towards the receiver head, in between which, any sample can be placed to measure. For example, if one laser has a wavelength of 783 nm and the other 782 nm, then by using Equation 1.2 the radiated frequency will be about 0.48 THz. The wavelength of the lasers is tuned in order to vary the THz output frequency.

$$f_{beat} = f_{laser_2} - f_{laser_1} \tag{1.2}$$

The PCS is an especially important part of the THz system as it is what allows it to have coherent detection. The square spiral antennas used in this system produce a circularly polarized wave, by having matching PCSs, each receiving a current bias, at each the transmitting and receiving heads the signal transmittance between them can be coherently detected because the frequencies used for mixing can be detected and subsequently removed from measured results.

Although this equipment is inexpensive and provides a high frequency resolution it only provides amplitude information when taking measurements. This system can be configured to take measurements in either a reflection or transmission mode but only the transmission mode is used here. This system, as well as all other THz systems to the best of my knowledge at the time of the writing of this thesis, cannot take reflection and transmission measurements simultaneously like a network analyzer can. This does greatly limit what can be measured definitively with this instrument when measuring circuits.

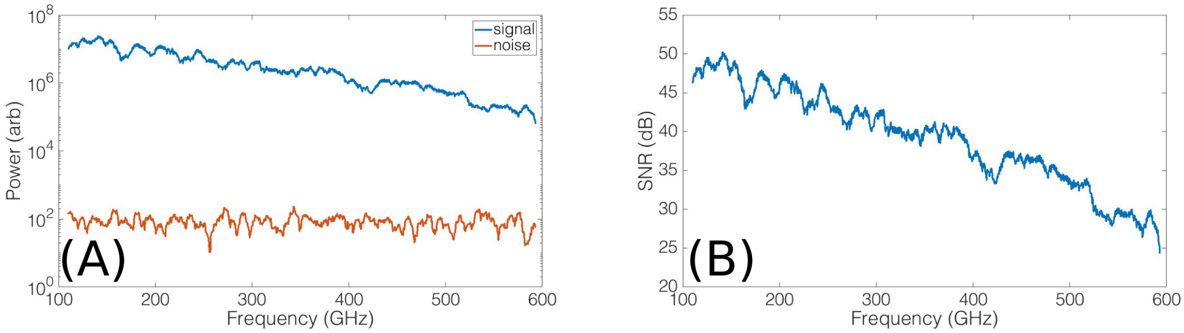

Figure 1.4: The (A) normal signal and noise floor of the THz measurement system and (B) the SNR of the system calculated using Eq 1.3.

$$SNR_{dB} = 10 \times \log_{10}\left(\frac{Signal}{Noise}\right) \tag{1.3}$$

Ultimately the transmission only measurements, when normalized to an appropriate background measurement to find a transmission parameter ($S_{21}$), still give a good comparison with which to compare simulation or theoretical results of the devices presented in this thesis. As shown in Figure 1.4 (A), the system measures the total power, in arbitrary units, between its transmitting and receiving heads on a logarithmic scale. The signal in (A) is a measurement taken with each of the heads directly opposite one another while the noise floor measurement was taken with a slab of metal between them in such a way that it completely blocks the signal path between the heads. In Figure 1.4 (B) the signal to noise ratio (SNR) does decrease with frequency but is very good and should allow some confidence in our measurements even if it falls short of the 70 dB-Hz SNR given in the equipment manual [1].

## 1.2 Wide-band circuits

Moving forward, to specifically see where THz frequencies can fit into solving larger problems within the circuits and systems sub-area first a background in high-speed, or wide-band, circuits will be provided. Shannon's theorem establishes that for any given amount of noise in a communication channel it is possible to send/receive discrete data error-free up to a maximum rate through that channel. That maximum rate, known as Shannon's limit, is directly related to the bandwidth of the channel and the signal to noise ratio (SNR). Since integrated circuits (IC) are limited in power, the SNR for a given system we could consider fixed, so in order to increase data rates the bandwidth must be increased, therefore, the frequency must be increased. Thus providing the motivation to develop THz range circuits and components in order to achieve wide bandwidths.

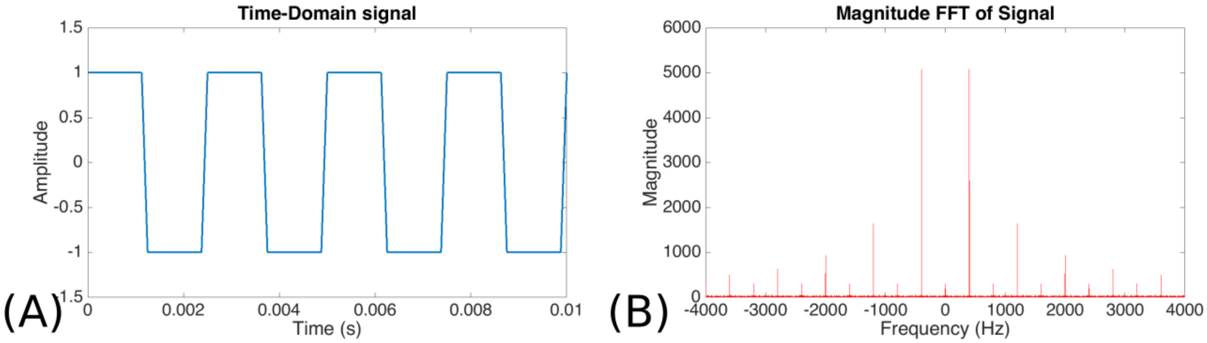

Figure 1.5: An example of the relationship between (A) a periodic rectangular pulse signal in the time domain and the (B) corresponding spectral content in the frequency domain.

An illustration of how digital data signals rely on a wide bandwidth can be seen in Figure 1.5. On the left is a periodic rectangular pulse signal which represents a digital data signal, for this example only a 400 Hz signal with an amplitude of 1 is used. Then, on the right, is the corresponding Fourier Transform of the signal which results in displaying the magnitude of the frequency spectrum present in the signal. Although here a perfect rectangular pulse is shown, in reality the pulse shape from a digital clock is trapezoidal in nature due to its relation to a clock signal, having a finite rising, or leading, edge and a falling, or trailing, edge and a duty cycle. Typically the lowest frequency spectra present, or the fundamental frequency, is the frequency of the data signal (or the inverse of time in units of seconds for one period of the signal to occur) and the higher order frequencies will be integer multiples of the fundamental frequency. The highest frequency spectral content present will be related to the duration of the rise or fall time, depending on which ever is shorter. If the rise or fall time is very short, the frequency needed to support that data to be fully recovered and not corrupted can be very high.

Here, bandwidth is defined as the difference between the upper and lower frequencies in a continuous band of frequencies, measured in hertz, that can be supported in a communication channel. Wideband circuits and systems refers to those whose bandwidth significantly exceeds the coherence bandwidth of he channel and ultra-wideband circuits are more specifically defined as those whose bandwidth exceeds the lesser of 500 MHz or 20 % of the arithmetic center frequency. For the work presented here with respect to the base waveguide design, the goal was to create a guide that could support frequencies from its cut off to 500 GHz with low-loss. These bandwidth goals address a need to have circuits which can operate from microwave frequencies into the millimeter and THz range as well as accommodating the harmonic content needed for next generation interconnects as further discussed in Section 1.2.2. Additionally, 500 GHz was chosen as the highest frequency to investigate due to limits in computational resources for simulation as well as capabilities to measure prototype devices reliably above the noise floor of the measurement equipment used.

### 1.2.1 Definition and motivation

As mentioned previously, THz designed components could provide a path for wide-bandwidth, high-speed circuits that still provide an all electrical solution to modern electronics needs. Here, some context for why that is needed will be explained. Americans are using an ever increasing amount of data and bandwidth. Trends show that every year more Americans are cutting their landlines and only using mobile data, and, are watching movies and television shows through streaming services and cutting their cable cords [44, 45]. They are also increasingly purchasing electronic devices that require internet connection such as gaming consoles, smart watches, smart appliances, and intelligent personal assistants such as Google Home or Amazon Alexa. Not only will these trends continue, but looking farther into the future, the United States is not the only place experiencing these technological shifts. Over the coming decades as more countries continue to modernize the world wide need for internet traffic will burgeon. Another reality that will likely occur within the near future, is a revolution of smart automobiles which will need a lot of data at very fast speeds. For an application like transportation, network latency would literally become an issue of life or death.

Specifically in this work, the THz regions greatest benefit is plainly that it provides potential for the highest frequencies and greatest possible bandwidth for electronic circuit applications. For commercial electronics, or systems that rely on them, there is increasing pressure to operate at higher frequencies with greater bandwidth. Given that these devices and systems are already being designed, fabricated, and implemented from an electronics perspective greater usability of the THz region would allow electrical engineers the greatest flexibility in solving these speed and bandwidth problems without needing to change the paradigm of the consumer electronics industry.

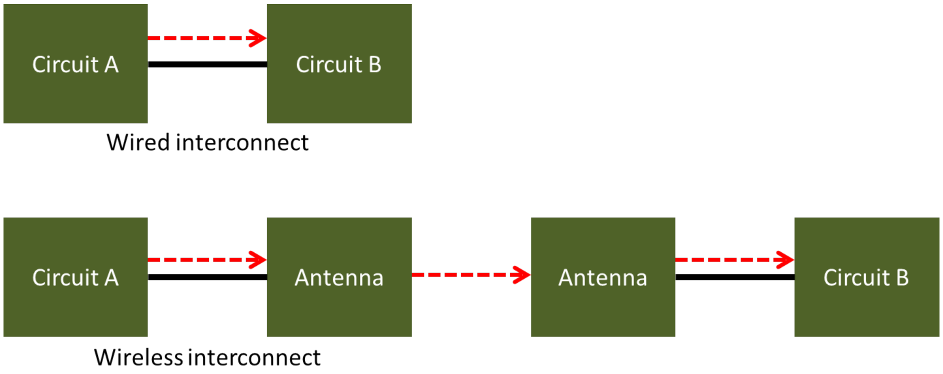

Figure 1.6: An illustration of the basic definition of an interconnect.

### 1.2.2 Literature review on interconnects

More specifically, a fundamental circuit building block that is needed to realize high-speed circuits that can accommodate THz range frequencies is an interconnect. An interconnect is a waveguiding structure, which can be wired or wireless, as shown in Figure 1.6 which connects two or more circuits or systems together. The type of interconnect discussed here is one that is on a semiconductor wafer (“on-wafer”) or on an integrated circuits board (“on-board”) such as would be used in the electronics packaging field.

What is “high speed”? Let’s look at the trends in the data rate of electrical interface standard OIF-CEI (common electrical I/O). In 2005 this standard specified 6 and 11 Gb/s serial links, in 2011 it specified 25 and 28 Gb/s links, specifications for 56 Gb/s links are expected to be completed in 2018 [46, 47], and, as of late 2016, standards for 100 Gb/s links are being developed [48]. In the frequency domain, a single pulse of signal of data at 25 Gb/s has harmonic content well above 100 GHz and data transfer rates above 100 Gb/s would have harmonics well above 300 GHz (which is 0.3 THz). Data rates above 25 Gb/s, and especially above at or above 100 Gb/s are “high speed” and, as discussed in [47], there are many challenges for moving to 56 Gb/s and beyond such as specifying channel return loss, device return loss, and near and far end cross-talk that were not considered in the previous standards which only considered differential insertion loss of the forward channel versus frequency. It has been observed that the transceiver density and speed doubles every two generations and the bandwidth requirements of transmission lines will continue to grow, reaching terabyte/s (Tb/s) bandwidth in the next decade [49, 50, 51].

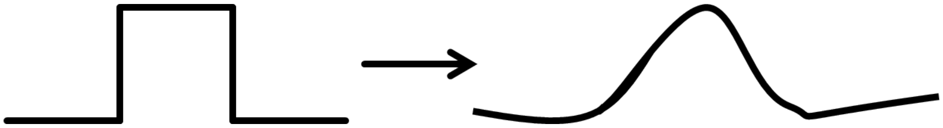

Figure 1.7: An illustration of dispersion of a single digital data pulse.

In order to minimize dispersion of these signals a low-loss interconnect that can handle terahertz (THz) frequencies is needed. Dispersion is the phenomenon of different frequency components of a propagating wave traveling at different velocities through a waveguide. This phenomena can be seen in Figure 1.7 where a single digital data pulse is distorted after traveling through a dispersive medium. In digital circuits, dispersion leads to distortion of the digital pulse which can lead to error (or corruption) in transmitted information.

Currently in industry and academia there are three main approaches being pursued to solve this problem:

1. optical interconnects,
2. electrical interconnects in parallel, and
3. electrical interconnects that use dielectrics such as ribbon waveguides.

Many optical based solutions have been proposed to address the need for high data rates. In [52] researchers demonstrated a multicore fiber with linear arrays of 4 cores compatible with edge coupling and rectangular arrays of 8 cores handling standard bidirectional transmission bandwidths of 40 or 100 Gb/s with 4 cores carrying 10 or 25 Gb/s per direction. Another optical technique is to use multilevel pulse amplitude modulation (PAM), as done in [53] where an 8-PAM setup is used to achieve 56 Gb/s. Commonly a vertical cavity surface emitting laser (VCSEL) is used as the source for optical solutions and, as shown in [54], the highest data rate in a single channel using such a laser has been reported at 56.1 Gb/s. Even more impressive as a novel solution, is using silicon photonic microring links which could provide bandwidth densities as high as 1.8 Tb/s on a single optical link [55], although, this solution is highly sensitive to alignment and requires amplification to achieve its bandwidth.

Ultimately, even with some of the impressive results shown for optical designs, it is inherently non-ideal due to the necessary conversion from electrical to optical and back to electrical to use these solutions in integrated systems. Even if the conversion is fast, the conversion requires additional power and real-estate when implemented on-board. Much of this work has been targeted for specific applications such as in high performance computing centers as in [52] but due to its limitations it is less feasible as a solution in consumer electronics as an all electrical alternative.

Overall, there has been significant advances made in the area of optical interconnects to meet the need of Tb/s data transfer. However, the implementation of optical devices on silicon (Si) chips is a major challenge as well as the increase in energy dissipation when up converting digital data to optics and back. Electrical interconnects that can reach Tb/s will allow data transfer at lower power costs per bit and will require less complex circuits.

When using electrical interconnects the state of the art tends to rely on the use of running lines in parallel to create an effective data transmission rate of 25, 56 or 100 Gb/s. As an example, Ultra-High Definition Television (UHDTV) uses 3840 pixels by 2160 pixels at each frame which requires transfer of large data in a very short time. To meet this need, four lanes each carrying 25.78 Gb/s are being implemented [56]. Several types of waveguides operating in the millimeter and THz frequency regions have been demonstrated [57, 58, 59, 60, 61, 62, 63, 64, 65]. This includes microstrips, substrate integrated waveguides (SIW) and dielectric ribbon waveguides. Among these, for < 25 Gb/s, microstrip transmission lines are popular as they are simple to design and fabricate, and are compatible with high density thin film integration of digital interconnects. At high signal speeds (> 25 Gb/s), signal loss and dispersion become a major challenge in these transmission lines. Generally, dispersion through waveguides is modeled as an effective dispersive filter, and both passive and active methods have been investigated to mitigate dispersion in data transfer. Microstrip transmission lines with engineered dielectric properties have been investigated as a passive method to reduce dispersion. However, the loss of microstrip transmission lines is high at higher frequencies due to skin effect losses. Thus, alternate waveguide approaches to design high-speed digital interconnects are desirable.

SIWs also have been demonstrated to be low-loss compared to microstrip transmission lines and are compatible with wafer-level integration. SIWs can be designed to operate at a single mode over a frequency range of approximately 100 GHz but tend to be narrowband. Dielectric ribbon waveguides, which are comprised of a high dielectric constant core surrounded by a low dielectric constant cladding, are another option which are attractive for their low-loss, ultra-wide bandwidth and low dispersion at high frequencies. But, cross-talk is a challenge due to evanescent waves in these waveguides as they are comprised purely of dielectric materials. The advantage of SIWs over ribbon waveguides is that the cross-talk between the neighboring lines can be minimized and waveguide transitions are simpler to design. Thus, a hybrid solution is needed which combines the advantages of both of these waveguide designs.

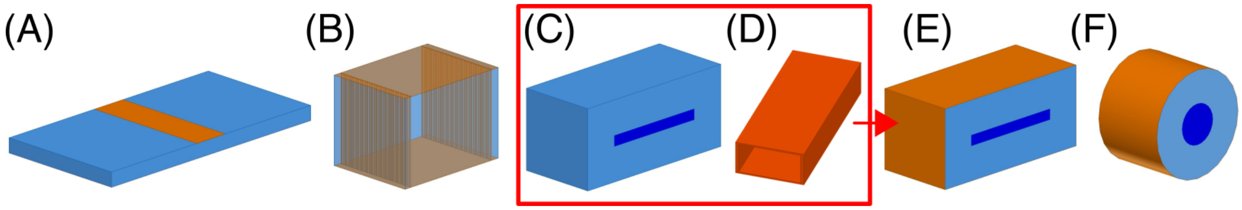

Figure 1.8: Illustration of the proposed waveguide and its competitors where (A) is a microstrip line, (B) a substrate integrated waveguide (SIW), (C) a dielectric ribbon, (D) a traditional metal waveguide, and (E) and (F) are the rectangular and circular cross-sectioned proposed waveguides respectively.

As can be seen in Figure 1.8, models of the waveguiding structures discussed in this introduction are shown. Specifically of note are models (C) and (D) which show depictions of a ribbon waveguide and traditional metal waveguide of rectangular cross-section respectively. The proposed waveguide design proposed to explore in this thesis work is a combinations of these two well known designs to create a substrate integrated ribbon waveguide (SIRW) which is depicted in Figure 1.8 (E) and (F).

The new waveguide design, as first introduced in [66], fills an imminent need for high-speed, wide-bandwidth data transmission in consumer and industrial electronics. This design combines that of a dielectric ribbon waveguide with a traditional metallic waveguide. It holds more promise than optical solutions by avoiding the need for conversion between optical and electrical signals. As compared to other electrical interconnect solutions it allows the potential for 100 Gb/s data rates in a single series link but without the main drawbacks of SIWs and ribbon waveguides by maintaining a wide bandwidth and being resistant to cross-talk respectively.

## 1.3 Overview of research

### 1.3.1 Challenges addressed in this work

With the provided background in the THz research field in mind, as well as the background in the area of high-speed circuits, there are many challenges to specifically contribute to this sub-area. Namely:

1. designing wide-band circuits that are compatible with wafer or board level integration,
2. realizing wide-band circuits especially with a low-cost fabrication technique, and
3. improving measurement techniques and needed passive components to reliably measure devices.

The proposed waveguiding structure and its derivatives in this work specifically address the need for circuits with a wide bandwidth. Wide-band circuits are nontrivial to design and realize as well as necessary to accommodate high data transfer rates and systems that need to communicate across several frequency bands. Furthermore, the actual fabrication of such wide-band circuits proves challenging and/or expensive. The use of low-cost, additive manufacturing based fabrication techniques in this work provides a path to realizing such designs. Lastly, given that the THz range is still emerging there are few, if any, off the shelf components for use in measurements and measurement techniques are still developing. There is little work that utilizes CW THz systems but the work in this thesis demonstrates the possibilities and limitations of applying a CW THz system to a broad variety of measurement tasks. Additionally, passive components such as probes are improved upon in this work as well as a technique to measure an antenna.

### 1.3.2 Thesis statement

The goal of this work is to contribute to the existing body of knowledge on THz circuits and systems design, simulation, fabrication, and measurement specifically for wide-band, passive device applications, which could be applied to the consumer electronic market. Specifically a new waveguiding design is proposed, theoretically analyzed, and applied to different basic RF circuit building blocks. Additionally, low-cost fabrication methods are explored and the use of low-cost measurement systems are used, a commercially available CW system, and its effectiveness is evaluated.

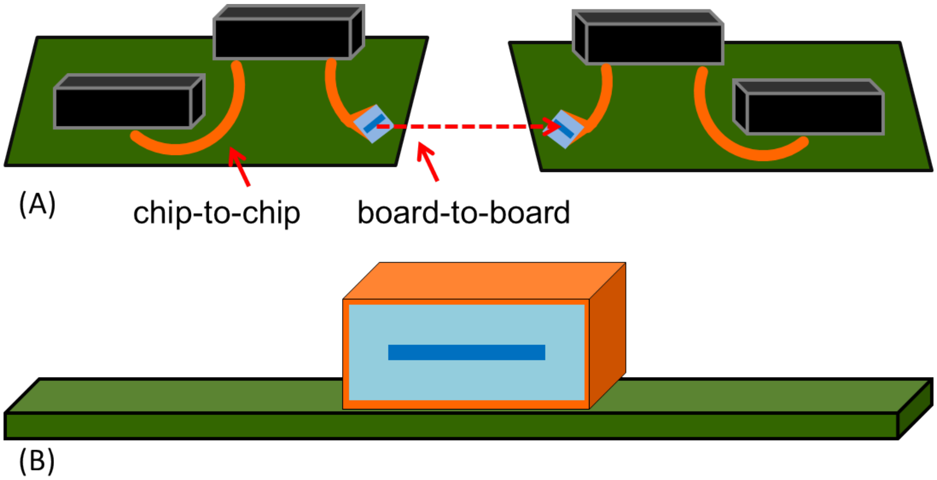

Figure 1.9: An (A) illustration of the future possible application of the work in this thesis and (B) a visual of the proposed waveguide when direct printed on-board as intended for its future use.

As seen in Figure 1.9, a possible future application of the work presented in this thesis provided. The proposed waveguiding structure could be manufactured on an electronics package to provide wired and wireless connects for chip-to-chip and board-to-board communication is a larger system while minimizing design complexity and the materials and fabrication processing needed.

### 1.3.3 Dissertation layout

Now, given the background provided in this chapter, in the following Chapter 2 the design and simulation results for two different cross-sections, circular and rectangular, will be provided. A finite element analysis tool will be used to investigate propagation characteristics, electric field confinement, confinement around bends, and their comparison to conventional designs. The measurement of the fundamental waveguiding design will also be presented and a theoretical

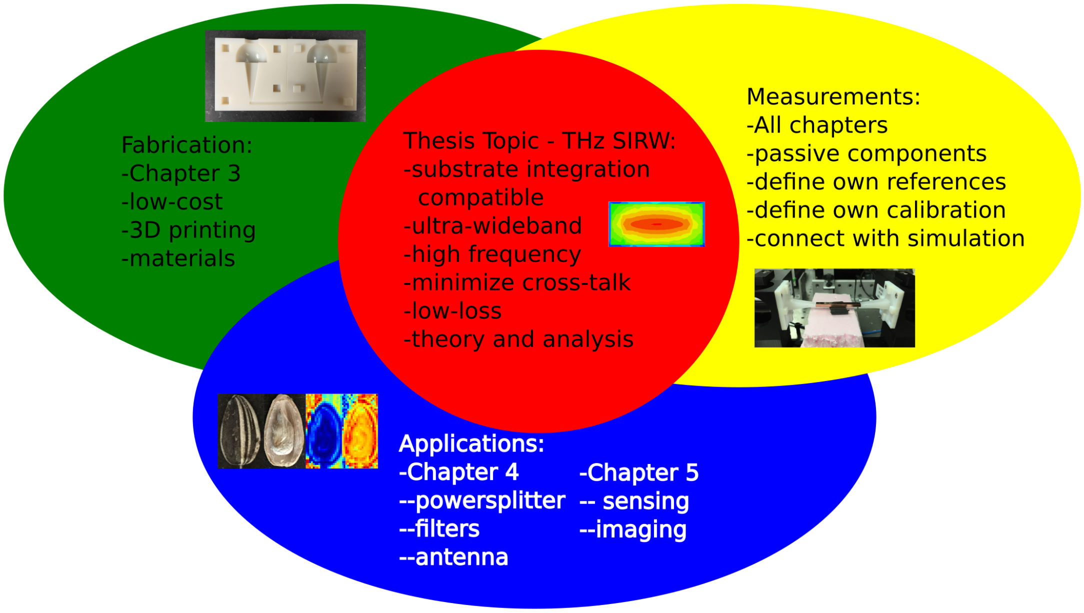

Figure 1.10: A holistic view of the contents within this thesis to provide understanding that this work is taking a "big picture" approach to a practical problem.

analysis of the proposed waveguiding structures will be detailed. This will include the derivation of the structures' characteristic equations and numerical results for their fundamental and higher order modes. Chapter 3 will give details on the related work of using low-cost fabrication methods for making passive THz components which will include using 3D printing, injection molding, and investigating 3D printed plastics material properties. Chapter 4 will extend the basic waveguiding design for other circuits which will include a power splitter, a wireless interconnect (antenna), and three different integrated filter designs. Lastly, Chapter 5 will extend the design to sensors including work in probes and imaging. Chapter 6 will conclude this work and detail the further work that could be explored from that presented here. Extended details of certain laboratory procedures and codes used will be provided in the appendices.

A diagram to illustrate the holistic view this work takes on addressing the need for a new waveguiding structure can be seen in Figure 1.10. In order to address the need for a different waveguiding design, many aspects of the design needed to be considered including theory and design, simulation, fabrication, measurement, and applications. Any one of these areas could be vetted thoroughly to the extend that they could complete a thesis in their own right, however, the aim in this work is to explore each of these areas in concert to achieve the more holistic goal of providing a preliminary proof of concept to this idea.

# CHAPTER 2

# DESIGN AND THEORETICAL ANALYSIS

## 2.1 Overview

The waveguiding design proposed in this work is introduced in detail beginning with the design implementation used to be fabricated and measured as well as simulated to compare with measured results. Next, a theoretical analysis is given looking more into the literature for dielectric ribbon waveguides and a comparison to other conventional designs is provided through simulation. For both the circular and rectangular cross-sections the characteristic equations are found. Lastly, simulations are presented to investigate the potential issues with higher order modes being excited or supported within the proposed waveguide as well as considering what modes could have been excited by the method of feeding the fabricated guides in measurement.

## 2.2 General waveguide design

The basic design of the proposed structure for both cross-sections, seen in Figure 2.1, is to have a high dielectric constant core surrounded by a lower dielectric constant cladding with a thin layer of copper around the outside. Such a waveguide structure is simple to implement at the wafer level in planar form similar to a SIW. To simplify fabrication, 3D printing is invoked to produce the cladding layer which is then surrounded by a continuous thin metal film.

Two basic wave guiding geometries, cylindrical and rectangular, have been employed and four lengths, 10, 20, 30, and 50 mm were fabricated. The simulated models use a length of one wavelength, in free space, at the solution frequency in order to reduce simulation time and computational cost, additionally, no difference was seen in simulation results for models with a length of one wavelength and those with much longer lengths up to three wavelengths. Alumina, with a dielectric constant ($\epsilon_r$) of 9.2 and tan$\delta$ of 0.003, and VeroWhitePlus®, with a dielectric constant ($\epsilon_r$) of 2.8 and tan$\delta$ of 0.04 were used for the cores and claddings respectively. Both are relatively low loss for the frequency range investigated. Further details on the material properties on VeroWhitePlus® will be discussed in Section 3.4.

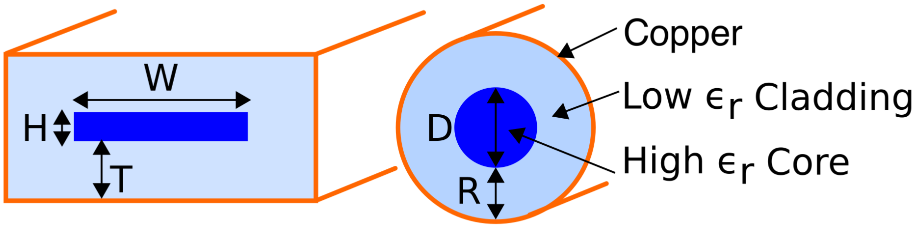

Figure 2.1: Cross-sectional view of the two waveguide structures presented.

The rectangular alumina has a width ($W$) of 3.8 mm and a height ($H$) of 0.4 mm. The cylindrical alumina has a diameter ($D$) of 1.588 mm. The cladding thickness for the rectangular waveguide ($T$) and the cylindrical waveguide ($R$) were both a value of 1.3 mm. The copper layer is approximately 1 µm thick. The dimensions used here were determined by optimizing, in simulation, for what could be realized to be fabricated and measured using supplies in the lab and the 3D printing resources available as are further discussed in Section 3.3. If a waveguide design using this proposed approach here were to be actually realized, much smaller dimensions with a smaller core to cladding ratio would be used, this is also further discussed in Section 2.7.

### 2.2.1 Simulation

Simulations were performed using the commercial FEM tool ANSYS Electronics Desktop High Frequency Structure Simulator (HFSS®). For each of the proposed structures discussed in the design section, transmission ($S_{21}$) and reflection ($S_{11}$) coefficients, propagation phase ($\beta$) and loss ($\alpha$) constants, as well as electric field confinement were investigated. The structures were meshed at 500 GHz and solved at frequencies between 100 and 500 GHz discretely to calculate these parameters across a wide frequency range with the most accuracy. The structures were simulated for a length of $1\lambda$, 0.6 mm, at the meshing frequency to limit computational cost where the wavelength is in free space which is longer than a wavelength in the guided medium. All of the simulation results discussed and presented here at at the fundamental mode, a discussion of higher order modes will be presented in Section 2.7.

#### 2.2.1.1 Wave propagation characteristics

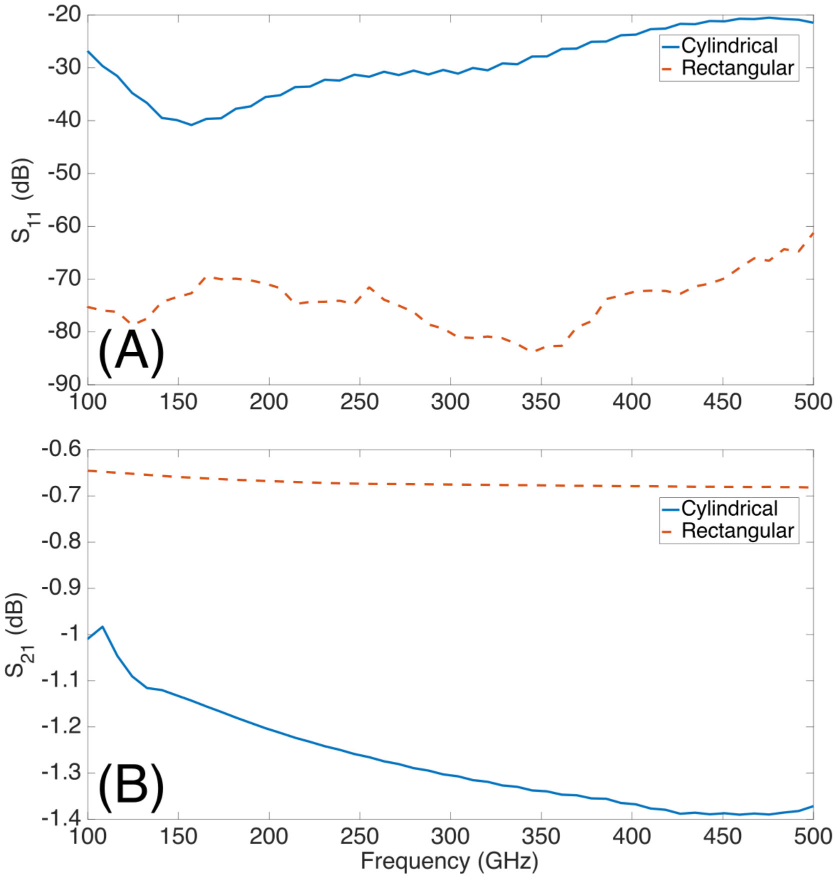

Figure 2.2: Simulated (A) $S_{11}$ and (B) $S_{21}$ of the waveguide structures for $1\lambda$, or 0.6 mm, of length.

As seen in Figure 2.2, both of the proposed structures showed very low reflection and high transmission at low THz frequencies, as a reference point, at 300 GHz the circular and rectangular cross-sectioned guides have an $S_{11}$ of -30.4 and -79.4 and $S_{21}$ of -1.3 and -0.7 dB, respectively. Slightly better performance from the rectangular cross-section as compared to the circular cross-section guide is expected given that [67] has shown that for a ribbon guide operated in its dominant mode the loss factor for a ribbon guide could be as much as 100 times smaller as that for a circular rod. In simulation, losses due to the dielectric materials were included as well as potential loss due to surface roughness and skin effects. The dielectrics were modeled using real values for the dielectric constants and loss tangents. The metal layer was modeled as a finite conductivity boundary using copper as the material with a thickness of 1 µm and a surface roughness of 5 µm to be as realistic as possible. Surface roughness for 3D printed parts varies greatly depending on the resolution of the 3D printer and the mechanism by which the part is metallized. For the fabrication process used here, a surface roughness between 5 to 10 µm, maximum peak, is typical for the printed plastic and then the 1 µm of copper is conformally coated onto its surface.

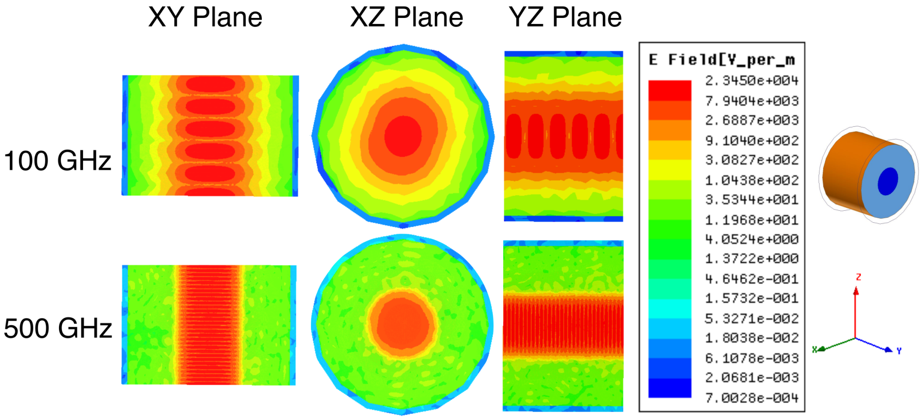

Figure 2.3: Simulated E-field confinement for the cylindrical waveguide design.

#### 2.2.1.2 Electric field confinement

To demonstrate how this structure can accommodate frequencies from the upper microwave region to the low terahertz region, electric field confinement was investigated in simulation. Referring to Figures 2.3 and 2.4, electric fields were computed in HFSS® for 100 and 500 GHz on the XY, XZ and YZ viewing planes. It is clear in these samples of the electric field that at low frequencies the field is mostly confined by the outer metal layer whereas at high frequencies the wave is confined by the alumina core like a traditional ribbon waveguide. This indicates that these waveguides can fit a niche in allowing high microwave frequencies to increase into low terahertz frequencies without any additional loss. Additionally, because of the good field confinement, these waveguides can provide minimal cross-talk with neighboring lines which allows a higher density of interconnects to be realized.

As a note to the reader, the field overlays shown are the magnitude of the electric field, in V/m, on a logarithmic scale as plotted on sheets bisecting the model geometry where the sheets have no material or boundary assignment and therefore do not affect the simulation results. HFSS solves in the frequency domain and obtains a phasor representation of the steady-state FEM solution where the electric field plotted here is $E(x, y, z, t) = E(x, y, z) \times \cos(\omega t + \theta)$ where $\omega$ is the solution frequency of the simulation. The electric field shown in Figure 2.4 and any other figure in this work where fields are plotted is showing the field at some fixed time and phase. The fields appear to have a standing wave pattern, which could indicate problems such as poor matching at the ports of the model, but this effect is an artifact of some part of the HFSS software's processing of the results. A sanity check was performed where a perfectly matched microstrip line of multiple wavelengths was simulated and a similar standing wave type pattern was observed indicating that this is not actually a standing wave pattern but due to some other effect.

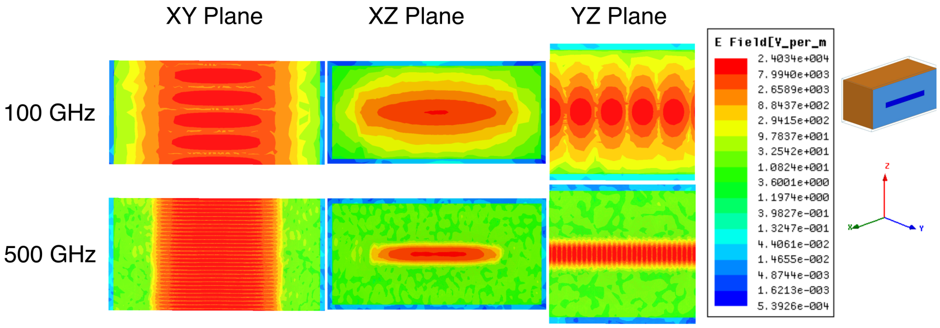

Figure 2.4: Simulated E-field confinement for the rectangular waveguide design.

These waveguides also confine fields well through bends. Bends can results in significant radiation if confinement is not maintained [68]. In HFSS® 90° bends, with bend radii of 10 mm, for both geometries were modeled and simulated at 100 and 300 GHz. The field confinement, which can be seen in Figure 2.5 on a linear scale, shows that for both frequencies and geometries the field is very confined through the bend. It is also clear that the boundary between the core and the cladding confines most of the field, but that the metal coating does significantly improve field confinement over results seen for ribbon waveguides in the literature [61].

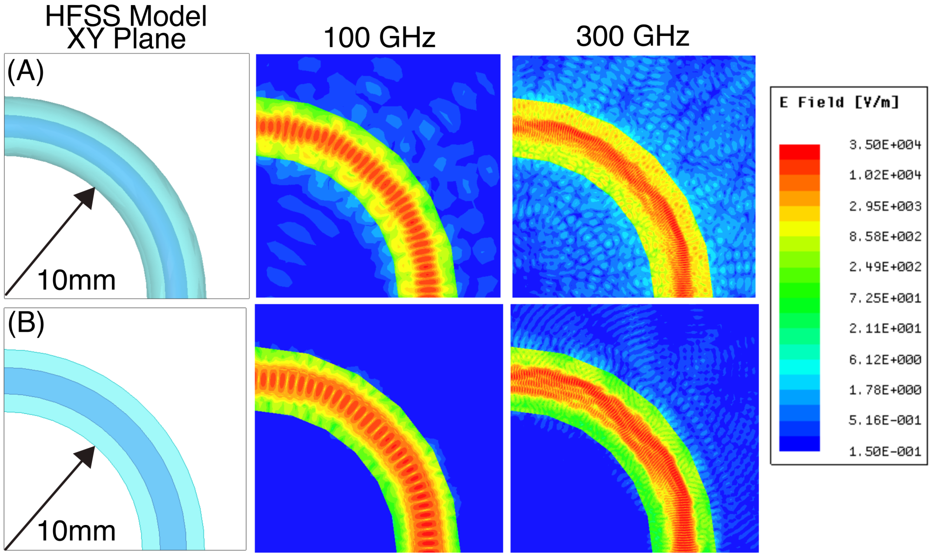

Figure 2.5: Simulated E-field confinement through a 90° bend, with bend radii of 10 mm, for the (A) cylindrical and (B) rectangular waveguide designs.

#### 2.2.1.3 Possibilities with 3D printing: gradient dielectric

As fabrication techniques and technologies continue to improve for additive manufacturing more exotic structures can be realized. Work has been done in the past to create polymer-ceramic nanocomposites [61], but recent work has demonstrated the possibilities to 3D print these composites directly [69]. As this technology improves, this would allow the ability to print dielectric substrates or structures using a gradient of dielectric materials.

Although currently such a structure could not be realized, the concept can be demonstrated through simulation. As seen in Figure 2.6, the proposed SIRW structures, which have two dielectric layers, can be compared to structures with more dielectric layers thus providing a gradient. Here, a model with five layers is used for each where $r = 0.42$ mm, $t = 0.65$ mm, and the core has a $W$ of 3.8 mm and $H$ of 0.4 mm same as in the original structure. HFSS® was used for simulation,

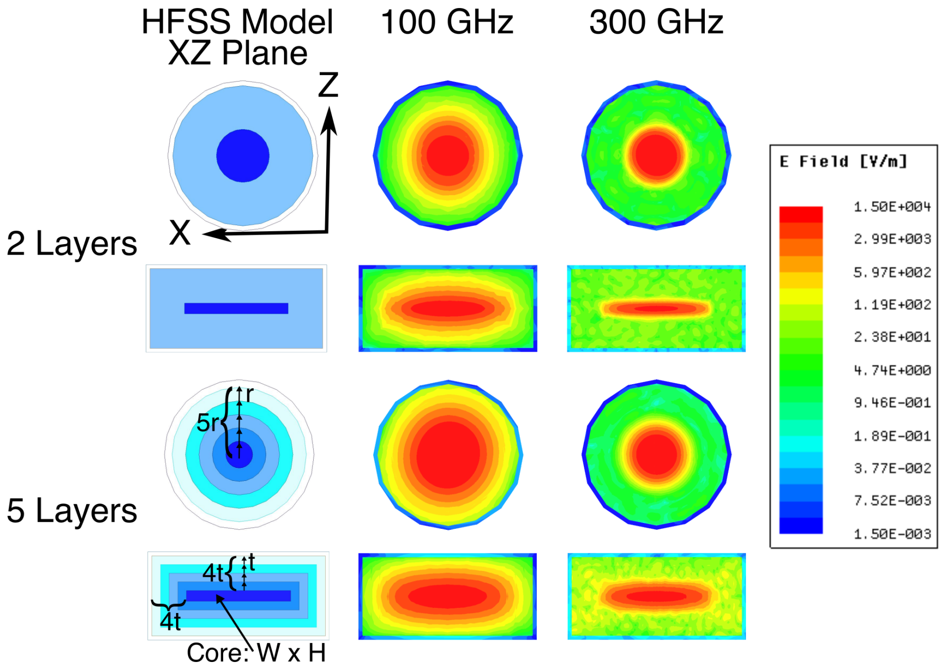

Figure 2.6: Simulated gradient dielectric waveguides for the cylindrical waveguide design showing the field confinement as compared to the SIRW design.

the structures were solved and meshed at 300 GHz, and losses from dielectrics and metals were included. The dielectric layers were comprised of Roger's substrate materials to be realistic. The five layer structure is comprised of, from inner most to outer most, RO3210 ($\epsilon_r$ = 10.2 and tan$\delta$ = 0.003), Rogers TMM 10 ($\epsilon_r$ = 9.2 and tan$\delta$ = 0.0022), RO3006 ($\epsilon_r$ = 6.15 and tan$\delta$ = 0.0025), Rogers TMM 4 ($\epsilon_r$ = 4.5 and tan$\delta$ = 0.002), and RT/duriod 5880 ($\epsilon_r$ = 2.2 and tan$\delta$ = 0.0009). For this comparison, the SIRW structures were re-simulated using RO3210 as the core material and RT/duriod 5880 as the cladding material in order to be reasonably compared to the gradient structures.

Figure 2.6 shows that the gradient dielectric waveguide provides comparable electric field confinement as the original two dielectric structures. However, in Figure 2.7, the benefits of the dielectric gradient are more clear. In Figure 2.7 (A) the propagation loss constant of the proposed SIRW structures is compared to structures with five step gradients. Although the change seen here is small, the simulation results do show that using a gradient dielectric can reduce propagation loss. Loss reduction could be further improved by having a more gradual gradient or optimizing the gradient in some fashion. Additionally, in Figure 2.7 (B), increasing the number of gradient dielectric layers does not seem to produce much change in the propagation phase constant. In Figure 2.7 (C) the effective dielectric constant for these structures shows that at high frequency the dielectric constant looks similar for the two and five layer structures, however, on the lower end of the frequency range investigated the dielectric constant is higher for the gradient structures. Therefore, being able to have a gradient structure could improve propagation loss, improve electric field confinement at lower frequencies while not effecting the propagation phase constant.

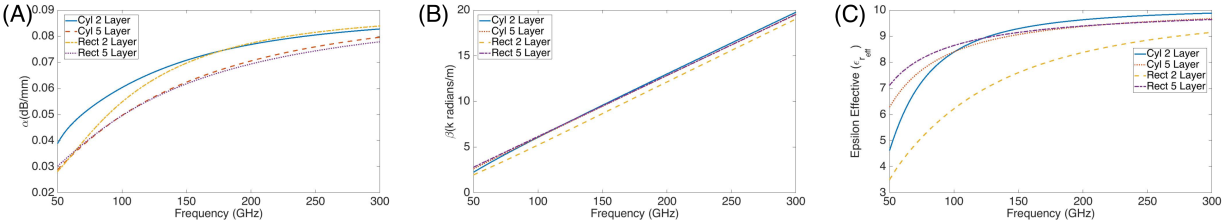

Figure 2.7: Simulated gradient dielectric waveguides as compared to the SIRW design for propagation (A) loss and (B) phase constants and (C) effective dielectric constant

### 2.2.2 Measurements and results

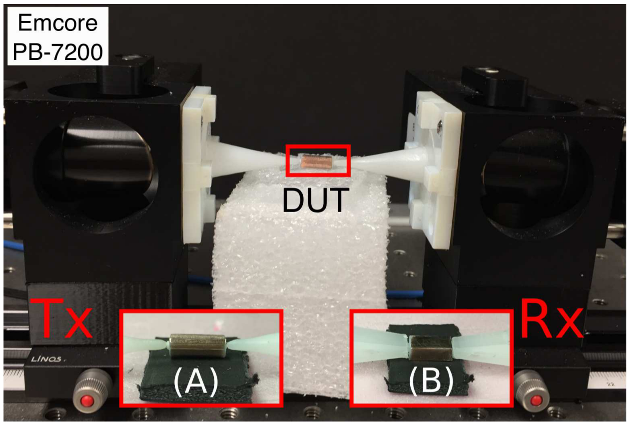

Figure 2.8: Measurement setup: (A) close up of probes coupling into the 10 mm cylindrical waveguide and (B) close up of probes coupling into the 10 mm rectangular waveguide.

Measurements were made using a quasi-optical THz measurement setup with the commercial frequency domain Emcore PB-7200 system. The measurement setup uses high and low density polyethylene based dielectric focusing probes to couple the waveguides to the Emcore system as seen in Figure 2.8. This system measures the total transmitted power between the transmitting and receiving heads in arbitrary units. Therefore, the measured transmitted signal for the fabricated structures includes effects from any misalignment of the quasi-optical setup and the dielectric focusing probes. The probes for the rectangular waveguide feed the entire face and the probes used for the cylindrical waveguides only feed the core material. From the simulation results presented in the Section 2.3, it can be assumed that this difference will not make any effect on the measured results.

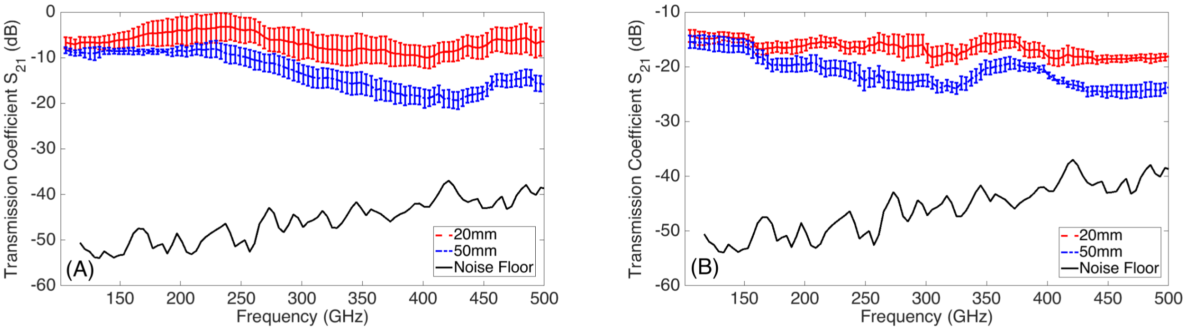

Figure 2.9: Measured transmission coefficient ($S_{21}$) for the (A) cylindrical waveguides and (B) the rectangular waveguides.

Terahertz frequency domain spectroscopy was performed from 100 to 500 GHz with a resolution of 0.5 GHz, and results can be seen in Figure 2.9. The reference signal used in each plot to calculate the transmission coefficient is the measured signal of the reference probes used to coupled into the waveguides positioned tip to tip. Probes with round tips and ones with rectangular tips were used to couple into the cylindrical and rectangular waveguides respectively. Each waveguide and reference measurement was taken five times and the traces in Figure 2.9 represent the average of those measurements where the error bars represent one standard deviation. The most consistent measurements were seen for the 20 and 50 mm length waveguides of each cross sections so only their results are shown.

Results show higher loss for the rectangular waveguides than the cylindrical devices for two main reasons. The THz system used for measurements transmits a circularly polarized wave which is much better coupled into the rounded probes used for the cylindrical waveguides. Secondly, a small amount of difference can be attributed to the difference in dielectric constant of the probes used. The rounded tip probes are made of high density polyethylene which was a slightly higher dielectric constant than low density polyethylene, which composes the rectangular tipped probes.

Additionally, some loss for both structures can be attributed to imperfect coupling between the structures and the probes used to measure them. Since the alumina rods were manufactured to size by hand their ends were not perfectly flat. The probes for measuring the rectangular waveguides were manufactured using a recently proposed injection molding process [70] which utilizes 3D printing to create custom injection molds. This process allowed the rectangular tip of the probe to be custom made to fit the waveguide structure in this work, but, the inherent surface roughness of the 3D printed molds used to create the probe could be affecting the coupling by leaving the tip surface not perfectly flat. Although the coupling is not ideal, the work in [71] shows that using these probes for a similar DUT, an alumina rod, the dominate contribution to the received signal is the one transmitted through the waveguiding DUT.

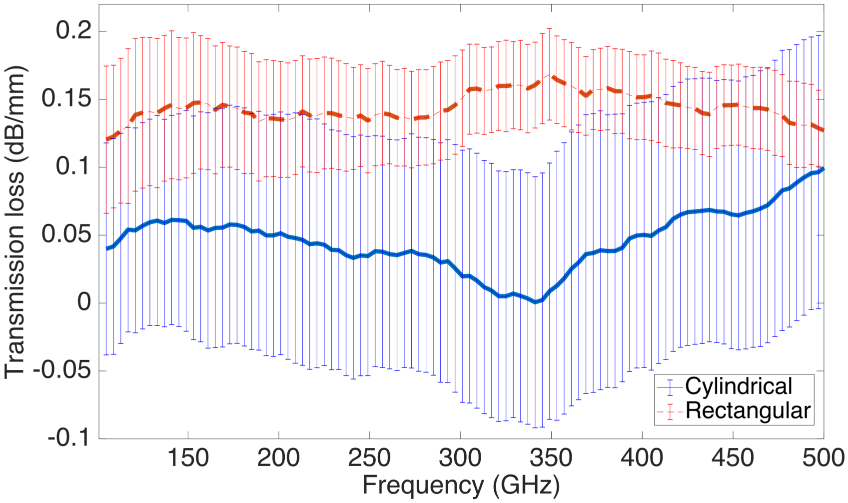

Figure 2.10: Measured loss in dB/mm versus frequency for the proposed structures. The error bars show one standard deviation away from the mean valued trace.

A notable result from the measurements is that there is not a significant difference in signal strength for the waveguides of different lengths as frequency increases. This indicates that these waveguides are very low loss per unit length. The loss per unit length, in dB/mm, can be calculated from the transmission measurements using the probe tip to tip measurement as a reference and can be seen in Figure 2.10. In Figure 2.10, the difference in the power (in dB) of two different measured lengths, the 50 and 20 mm length guides were used for both cross-sections, was taken and divided by the difference in length to get the loss per unit length across the frequency range measured, overall, both structures showed low loss across the range investigated. Additionally, here, to give an indication of the uncertainty of our measurements error bars have been included so the two main traces in Figure 2.10 are the mean of five separate measurements, were the guides were re-seated for each measurement, and the error bars show one standard deviation away from the mean. The loss per unit length, on average, found here is about the same as work for ribbon waveguides [61], and much less than that shown for microstrips where [72] found losses in a traditional 50 Ω microstrip of 0.2 dB/mm at 10 GHz.

## 2.3 Theoretical analysis

The proposed structures present a two-dielectric problem for a filled cylindrical and rectangular waveguide. The copper layer on both fabricated structures was 1 µm thick which is, using the standard formula for skin depth where $\mu_r = 1$ and $\sigma$ is the conductivity of copper, approximately 5 skin depths at 100 GHz and 11 skin depths at 500 GHz. Therefore, the metal thickness of these structures is sufficiently thick to consider it as a perfect electrical conductor. This allows these geometries to be treated as dielectric filled waveguides.

The cylindrical structure presented is a solved problem and can be found in popular electromagnetic textbooks [73] and within the literature [74, 75, 76]. A closed form solution for the cylindrical structure is readily solved for because it can be completely defined in cylindrical coordinates. In [73] it is shown that with the exception of rotationally symmetric fields, the modes present in this structure are neither TE nor TM to any cylindrical coordinate. Additionally, only

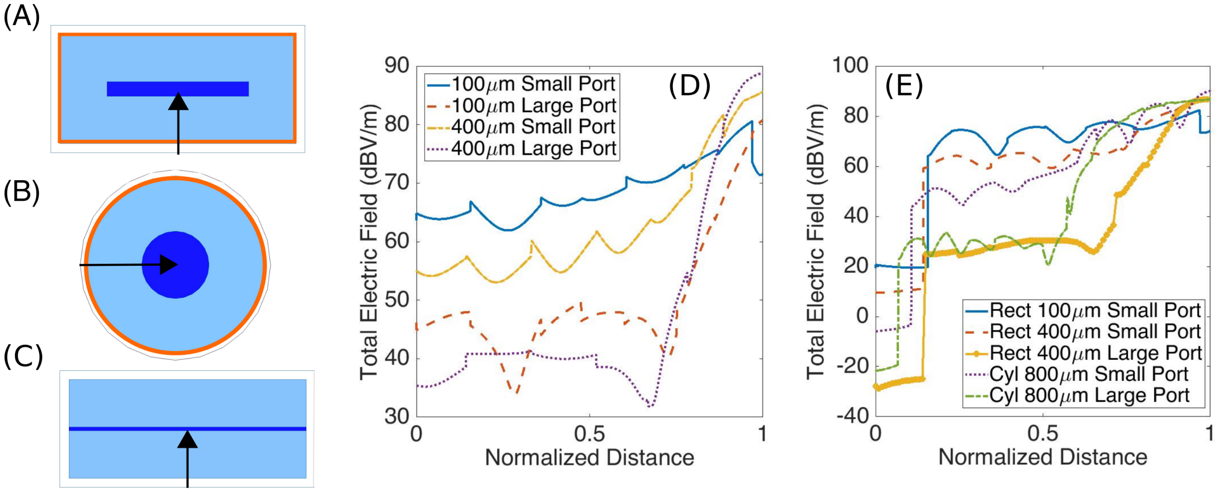

Figure 2.11: Simulated (A) rectangular and (B) cylindrical proposed waveguides, and (C) traditional ribbon waveguide models denoting the distance for which the total near electric field was calculated, and the near electric field versus normalized distanced for the (D) traditional ribbon waveguide and (E) the cylindrical and rectangular proposed waveguides. The small port refers to only feeding the core and the large port refers to feeding the entire waveguide face.

at the fundamental mode does the field separate into TE and TM to z modes, all other modes are hybrids. A partial derivation for the characteristic equation of the cylindrical structure can be found in [73] and a full derivation can be found in [74].

The cylindrical waveguide structure has also been well investigated in [77] where they note that as frequency increases (goes towards infinity) the electric field will tightly confine to the material with the greater $\epsilon\mu$ value, which would be the inner dielectric material here, and that at lower frequencies the structure functions similarly to a homogeneously filled waveguide.

The literature is prolific with solutions to dielectric filled rectangular waveguides of nearly every configuration [78, 79, 80]. But, a closed form solution for the rectangular structure presented here, by treating it as a dielectric filled waveguide similarly to the cylindrical structure, is difficult because boundary conditions cannot be clearly defined at the interfaces between the dielectric core and cladding. However, it is clear that the structure will behave similarly and have similar properties to the cylindrical structure. At higher frequencies, as are used here, it is indicated from the cylindrical waveguides known behavior to confine the electric fields to the higher dielectric constant material that the rectangular waveguide would behave similarly, and, therefore, behave somewhat like a dielectric ribbon waveguide.

Dielectric ribbon waveguides have been well explored in the literature for their use and application to millimeter wave [81] and THz [62, 61] circuits. But, these structures typically show the electric field as being confined in the cladding region directly near the boundary between the cladding and core layers as opposed to within the core. This difference in where the electric field is confined is due to the thinness of the core layer, and the way in which the waveguides are fed. In [62, 61] the core layer is very thin, around 100 µm thick, and only the core layer, not the entire face which includes the cladding layers, is excited in simulation. However, here a waveguiding structure that is a hybrid between a traditional ribbon waveguide and a SIW is proposed, and for SIWs the entire face of the waveguide is excited. Therefore, for the proposed waveguiding structures in this work the entire face is excited in simulation. For the traditional ribbon waveguides and the proposed structures if the core is sufficiently thin, here 100 µm is used, then it can be seen in Figure 2.11 that feeding the core only in simulation produces similar results for electric field confinement where the greatest amount of electric field is found at the boundary between the core and cladding.

The simulation results shown in Figure 2.11 were done in HFSS®, the structures in Figure 2.11 (A)-(C) were simulated at 300 GHz and the electric field was calculated along a polyline drawn as indicted by the arrows in the figure. The beginning of the arrow, at the waveguiding structures' edge correspond to a normalized distance of 0 and the end of the arrow, the point with the arrow head, corresponds to a normalized distance of 1. The rectangular and cylindrical structures in Figure 2.11 (A)-(B) have the same geometry and materials as in Figure 2.1 and the traditional ribbon has 1.3 mm thick cladding layers using VeroWhitePlus® and alumina as the cladding and core materials respectively. The electric field for the rectangular structure and the traditional ribbon is only plotted in the lateral direction of the waveguide face so that it can readily be compared to results presented in [62]. As seen in [62], when a traditional ribbon is simulated and only the core is excited the field is confined primarily to the cladding layer near its boundary with the core. But for the same structure if the entire face of the ribbon is fed the field is primarily confined to the

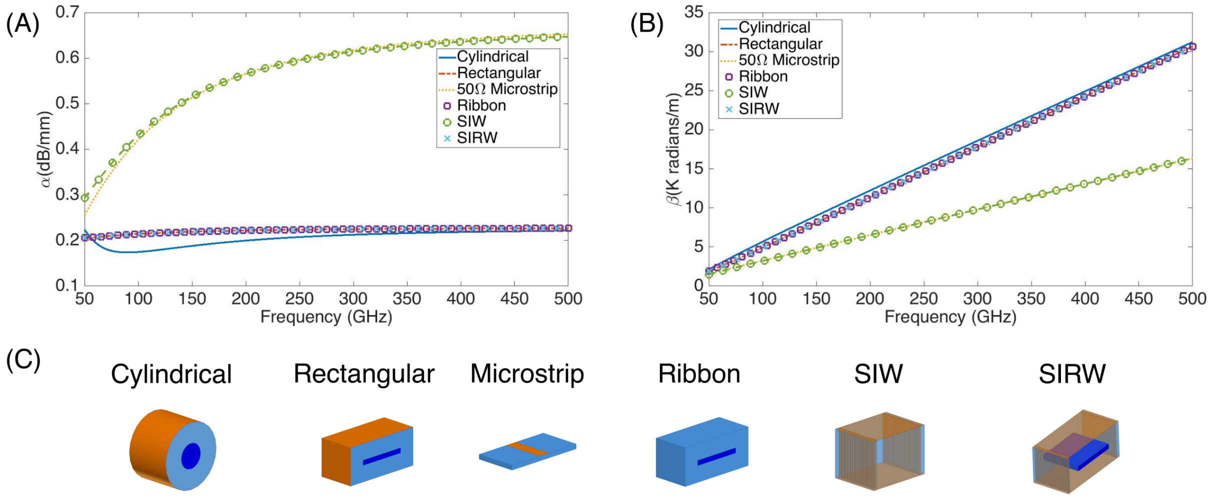

Figure 2.12: Simulated propagation: (A) loss ($\alpha$) and (B) phase ($\beta$) constant for the proposed structures as compared to other popular waveguiding structures whose models are shown in (C).

core. Additionally, as core thickness is increased to the thickness used for the proposed structure in this work, 400 µm for the rectangular waveguide and 800 µm core radius for the cylindrical waveguide, then the field is primarily confined to the core region despite the feeding method used. Ergo, for the thicker core geometries used here the two feeding methods yield the same results with respect to electric field confinement. In this work thicker core geometries were used primarily to accommodate the 3D printing manufacturing method which had a limited feature size.

## 2.4 Comparison to Conventional Designs

When investigating the propagation phase and loss constants the proposed structures were compared with a 50 Ω microstrip on a VeroWhitePlus® substrate, a ribbon waveguide comprised of a VeroWhitePlus® cladding and an alumina core, a substrate integrated waveguide, and a substrate integrated ribbon waveguide. The ribbon waveguide used here is not a traditional ribbon waveguide but the proposed rectangular structure with the metal boundaries removed. The substrate integrated waveguide had a VeroWhitePlus® substrate, the top and bottom metal layers were modeled as a finite conductivity boundary using copper material, and the via diameter and pitch were found using the design rules presented in [82]. The rules in [82] specify that the via diameter should be less than 1/5 the guided wavelength and the pitch less than or equal to twice the via diameter, here for for a frequency of 500 GHz in a dielectric of constant 2.8 the via diameter was 60.94 µm with a pitch of 104 µm. The substrate integrated ribbon waveguide model was the same as the rectangular waveguide model used for the structures proposed here but with vias instead of solid metal sidewalls. Only the fundamental mode of each waveguiding structure was considered.

The propagation loss constant, $\alpha$, can be seen in Figure 2.12 (A). Notably, the propagation loss for the proposed structures is maintained as frequency increases. This indicates that the structures do not suffer from additional conductor loss with frequency which would indicate that as frequency increases the wave becomes primarily bound by the alumina core of the inner dielectric ribbon and does not interact much or at all with the metal coating. This behavior is expected given the theoretical results for similar structures in the literature. It is expected that the ribbon waveguide would perform similarly to the proposed structures at this frequency range with no bends present, and it is also expected that the rectangular waveguide and the SIRW version of it would perform similarly given the confinement of the electric field to the alumina core for all those structures at these frequencies. The loss for the microstrip and SIW are much worse since the field is primarily confined by the metal in those structures which leads to high conductor loss in this frequency range.

Additionally, in Figure 2.12 (B), the propagation phase constant, $\beta$, is compared to simulated results for the same alternative waveguiding structures as the propagation loss. Ideally, the propagation constant, traditionally defined as $\beta = \frac{2\pi}{\lambda}$, would be proportional to frequency for the transmission of a wave to be undistorted in the time domain. So the propagation phase constant seen in the proposed SIRW structures, showing much more linear behavior with respect to frequency, indicates that the signal experiences less dispersion than the microstrip and SIW.

## 2.5 Circular cross-section

### 2.5.1 Description of problem

Although the general design presented in the previous sections provides a good proof of concept and demonstrates the design strategy's potential it is important to do an actual analysis of the waveguiding structure. Figure 2.13 provides an overview of the geometry to be analyzed where there are two concentric dielectric materials within a metal waveguide, all of which are of circular cross-section. It is assumed that the materials are perfectly centered in the guide, that their boundaries do not overlap, that there are no air gaps between the layers, that the metal boundary is a perfect electrical conductor, that the dielectric materials are non-magnetic and isotropic, that the region is source free (homogeneous), and that the waveguide extends infinitely in the z-direction.

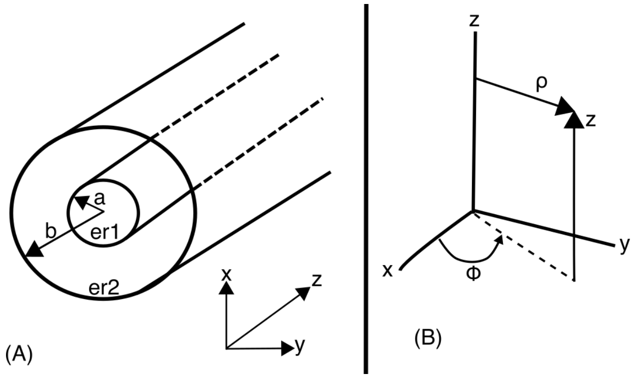

Figure 2.13: Problem geometry, walls of the waveguide are PEC and material is non-magnetic and perfectly fills the cross-section (etc.).

Following the procedure found in [73], the scalar wave functions for this structure must obey the scalar Helmholz equation, which, written in the cylindrical coordinate system is given in (2.1).

$$\frac{1}{\rho}\frac{\partial}{\partial\rho}\left(\rho\frac{\partial\psi}{\partial\rho}\right)+\frac{1}{\rho^2}\frac{\partial^2\psi}{\partial\phi^2}+\frac{\partial^2\psi}{\partial z^2}+k^2\psi=0 \tag{2.1}$$

Where $\psi$ is the scalar wave function, $\rho$ is the radial variable, $\phi$ is the azimuthal variable, $z$ is the axial variable, and $k$ is the propagation constant. The standard method for solving (2.1) for $\psi$ is to use separation of variables where a solution of the form (2.2) is found.

$$\psi = R(\rho)\,\Phi(\phi)\,Z(z) \tag{2.2}$$

Substituting (2.2) into and dividing $\psi$ out of (2.1) the following can be solved for:

$$\frac{1}{\rho}\frac{\partial}{\partial\rho}\left(\rho\frac{\partial\psi}{\partial\rho}\right)+\frac{1}{\rho^2}\frac{\partial^2\psi}{\partial\phi^2}+\frac{\partial^2\psi}{\partial z^2}+k^2\psi=0 \tag{2.3}$$

$$\begin{gathered}\frac{1}{\rho}\frac{\partial}{\partial\rho}\left(\rho\frac{\partial\left[R(\rho)\Phi(\phi)Z(z)\right]}{\partial\rho}\right)+\frac{1}{\rho^2}\frac{\partial^2\left[R(\rho)\Phi(\phi)Z(z)\right]}{\partial\phi^2}+\dots\\ \frac{\partial^2\left[R(\rho)\Phi(\phi)Z(z)\right]}{\partial z^2}+k^2\left[R(\rho)\Phi(\phi)Z(z)\right]=0\end{gathered} \tag{2.4}$$

$$\frac{1}{\rho}\frac{\partial}{\partial\rho}\left(\rho\frac{\partial R}{\partial\rho}\right)+\frac{1}{\rho^2}\frac{\partial^2\Phi}{\partial\phi^2}+\frac{\partial^2 Z}{\partial z^2}+k^2\left[R(\rho)\Phi(\phi)Z(z)\right]=0 \tag{2.5}$$

thus resulting in (2.6).

$$\frac{1}{R\rho}\frac{\partial}{\partial\rho}\left(\rho\frac{\partial R}{\partial\rho}\right)+\frac{1}{\Phi\rho^2}\frac{\partial^2\Phi}{\partial\phi^2}+\frac{1}{Z}\frac{\partial^2 Z}{\partial z^2}+k^2=0 \tag{2.6}$$

The third term is independent of $\phi$ and $\rho$ and so must be equal to a constant if the equation is to hold for all $z$, thus we can define (2.7).

$$\frac{1}{Z}\frac{\partial^2 Z}{\partial z^2}=-k_z^2 \tag{2.7}$$

Substituting this into (2.6) and multiplying through by a term of $\rho^2$ gives:

$$\frac{1}{R\rho}\frac{\partial}{\partial\rho}\left(\rho\frac{\partial R}{\partial\rho}\right)+\frac{1}{\Phi\rho^2}\frac{\partial^2\Phi}{\partial\phi^2}-k_z^2+k^2=0 \tag{2.8}$$

$$\frac{1}{R\rho}\frac{\partial}{\partial\rho}\left(\rho\frac{\partial R}{\partial\rho}\right)+\frac{1}{\Phi\rho^2}\frac{\partial^2\Phi}{\partial\phi^2}+(k^2-k_z^2)=0 \tag{2.9}$$

$$\frac{\rho^2}{R\rho}\frac{\partial}{\partial\rho}\left(\rho\frac{\partial R}{\partial\rho}\right)+\frac{\rho^2}{\Phi\rho^2}\frac{\partial^2\Phi}{\partial\phi^2}+\rho^2(k^2-k_z^2)=0 \tag{2.10}$$

which results in (2.11).

$$\frac{\rho}{R}\frac{\partial}{\partial\rho}\left(\rho\frac{\partial R}{\partial\rho}\right)+\frac{1}{\Phi}\frac{\partial^2\Phi}{\partial\phi^2}+\rho^2(k^2-k_z^2)=0 \tag{2.11}$$

Now the second term is independent of $\rho$ and $z$, which was the purpose of multiplying through by $\rho^2$, so similarly we can set the second term equal to some constant $n$ in the same fashion as seen in (2.12).

$$\frac{1}{\Phi}\frac{\partial^2\Phi}{\partial\phi^2} = -n^2 \tag{2.12}$$

We can also define a term $k_\rho$ for our terms related to propagation as in (2.13).

$$k_\rho^2 + k_z^2 = k^2 \tag{2.13}$$

Substituting (2.12) and (2.13) into (2.11), will result in an equation only in terms of $\rho$ and $R$ equal to zero.

$$\begin{align}
\frac{\rho}{R}\frac{\partial}{\partial\rho}\left(\rho\frac{\partial R}{\partial\rho}\right) + \frac{1}{\Phi}\frac{\partial^2\Phi}{\partial\phi^2} + \rho^2(k^2 - k_z^2) = 0 \tag{2.14}\\
\frac{\rho}{R}\frac{\partial}{\partial\rho}\left(\rho\frac{\partial R}{\partial\rho}\right) - n^2 + \rho^2(k_\rho^2) = 0 \tag{2.15}\\
\frac{\rho}{R}\frac{\partial}{\partial\rho}\left(\rho\frac{\partial R}{\partial\rho}\right) + \left[\rho^2 k_\rho^2 - n^2\right] = 0 \tag{2.16}\\
\rho\frac{\partial}{\partial\rho}\left(\rho\frac{\partial R}{\partial\rho}\right) + R\left[\rho^2 k_\rho^2 - n^2\right] = 0 \tag{2.17}\\
\rho\frac{d}{d\rho}\left(\rho\frac{dR}{d\rho}\right) + \left[\sqrt{k_\rho\rho} - n^2\right] R = 0 \tag{2.18}
\end{align}$$

Now (2.11) is only in terms of $R$ and $\rho$ and (2.12) can be rearranged only in terms of $\phi$ and $\Phi$ equal to zero.

$$\begin{align}
\frac{1}{\Phi}\frac{\partial^2\Phi}{\partial\phi^2} = -n^2 \tag{2.19}\\
\frac{\partial^2\Phi}{\partial\phi^2} = -n^2\Phi \tag{2.20}\\
\frac{d^2\Phi}{d\phi^2} + n^2\Phi = 0 \tag{2.21}
\end{align}$$

Lastly, (2.7) can be arranged in terms only of $z$ and $Z$ equal to zero.

$$\frac{1}{Z}\frac{\partial^2 Z}{\partial z^2} = -k_z^2 \tag{2.22}$$

$$\frac{\partial^2 Z}{\partial z^2} = -k_z^2 Z \tag{2.23}$$

$$\frac{d^2 Z}{dz^2} + k_z^2 Z = 0 \tag{2.24}$$

These three equations then are (2.25) - (2.27) and form a system of separated equations.

$$\rho\frac{d}{d\rho}\left(\rho\frac{dR}{d\rho}\right) + \left[\sqrt{k_\rho \rho} - n^2\right] R = 0 \tag{2.25}$$

$$\frac{d^2\Phi}{d\phi^2} + n^2\Phi = 0 \tag{2.26}$$

$$\frac{d^2 Z}{dz^2} + k_z^2 Z = 0 \tag{2.27}$$

We can see right away that (2.26) and (2.27) have solutions that are harmonic such as sinusoidal or exponential functions. The solution to (2.25) will be a Bessel function ((2.25) is actually Bessel's equation) and can be generally referred to as $R = B_n\left(k_\rho \rho\right)$. Therefore, a general solution for $\psi$ can be written as in (2.2) where:

$$Z(z) = e^{-jk_z z} \text{ for outgoing traveling waves (both TE and TM waves)} \tag{2.28}$$

$$Z(z) = e^{jk_z z} \text{ for incoming traveling waves} \tag{2.29}$$

$$\Phi(\phi) = \cos(n\phi) \text{ for TM or TE waves (normally used for TM)} \tag{2.30}$$

$$\Phi(\phi) = \sin(n\phi) \text{ for TM or TE waves (normally used for TE)} \tag{2.31}$$

The most commonly used functions in place of $B_n\left(k_\rho \rho\right)$ are Bessel functions of the first kind ($J_n\left(k_\rho \rho\right)$), Bessel functions of the second kind ($N_n\left(k_\rho \rho\right)$), Hankel functions of the first kind ($H_n^{(1)}\left(k_\rho \rho\right)$), and Hankel functions of the second kind ($H_n^{(2)}\left(k_\rho \rho\right)$). Since Hankel functions can be written as complex combinations of $J_n$ and $N_n$, any two of the above four functions can be taken as linearly independent solutions to (2.25). Therefore, the most general choice for $B_n\left(k_\rho \rho\right)$ is:

$$B_n\left(k_\rho \rho\right) = AJ_n\left(k_\rho \rho\right) + BN_n\left(k_\rho \rho\right) \tag{2.32}$$

where $A$ and $B$ are some unknown constants. Here, the lowest order mode (HE$_{11}$ mode) will be considered propagating in the $+z$-direction where the definition in (2.33) will be used.

$$k_\rho^2 + k_z^2 = k^2 \tag{2.33}$$

Vector field potentials in cylindrical coordinates systems take the following general form in (2.34).

$$\psi\left(\rho, \phi, z\right) = B_n\left(k_\rho \rho\right) h\left(n\phi\right) h\left(k_z z\right) \tag{2.34}$$

### 2.5.2 Determining vector potentials

The Bessel function will be most appropriately represented by a Bessel function of the first kind, $J_n\left(k_\rho \rho\right)$, because we know our fields should be finite at $\rho = 0$ and be a standing wave. A good representation for describing the field behavior with respect to $\phi$ is $\cos\left(n\phi\right)$ because we want a cylindrical region containing all $\phi$ from 0 to $2\pi$ making it necessary that $\psi\left(\phi\right) = \psi\left(\phi + 2\pi\right)$ if $\psi$ is to be single valued. This means that $h\left(n\phi\right)$ must be periodic in $\phi$ and n must be an integer. Instead of $\cos\left(n\phi\right)$, $\sin\left(n\phi\right)$ could also be equivalently used. Lastly, $h\left(k_z z\right)$ needs to represent a traveling plane wave in the positive z direction so $e^{-jk_z z}$ will be used. Thus, with some unknown coefficients *A*-*D* the wave functions for the two dielectric regions can be written where, for now, the Bessel function(s) used will be kept generic and the most appropriate choices will be selected later.

The total vector field potential for the core region, region 1, will be composed of the components in (2.35) where the superscript indicates the region and the superscript $e$ and $m$ indicate the electric and magnetic field potential components respectively.

$$
\begin{aligned}
\psi^{1} &= \psi^{e1} + \psi^{m1} \\
\psi^{e1} &= A B_n^{e1}\left(k_{\rho_1}\rho\right)\cos\left(n\phi\right)e^{-jk_z z} \\
\psi^{m1} &= B B_n^{m1}\left(k_{\rho_1}\rho\right)\sin\left(n\phi\right)e^{-jk_z z}
\end{aligned}
\tag{2.35}
$$

The total vector field potential for the cladding region, region 2, will be composed of the components in (2.36) where the same superscript convention is used as in (2.35).

$$
\begin{aligned}
\psi^{2} &= \psi^{e2} + \psi^{m2} \\
\psi^{e2} &= C B_n^{e2}\left(k_{\rho_2}\rho\right)\cos\left(n\phi\right)e^{-jk_z z} \\
\psi^{m2} &= D B_n^{m2}\left(k_{\rho_2}\rho\right)\sin\left(n\phi\right)e^{-jk_z z}
\end{aligned}
\tag{2.36}
$$

### 2.5.3 Solving for field components

Using the wave functions, all the field components for the two regions can be written. First the electric field components will be found, where, here, we will be using the formulas for field components for a TE$^{z}$ cylindrical coordinate system. This will be the same for each dielectric region, because the Bessel functions have been left generic until later, except for the constant out front. For finding the field components here the constant $A$ is used as a stand-in for $A$ and $C$ for the core and cladding regions respectively.

$$E_\rho = -\frac{1}{\rho}\frac{\partial \psi}{\partial \phi} \tag{2.37}$$

$$= -\frac{1}{\rho}\frac{\partial}{\partial \phi}\left(AB_n^e\left(k_\rho \rho\right)\cos\left(n\phi\right)e^{-jk_z z}\right) \tag{2.38}$$

$$= \frac{An}{\rho}B_n^e\left(k_\rho \rho\right)\sin\left(n\phi\right)e^{-jk_z z} \tag{2.39}$$

$$E_\phi = \frac{\partial \psi}{\partial \rho} \tag{2.40}$$

$$= \frac{\partial}{\partial \rho}\left(AB_n^e\left(k_\rho \rho\right)\cos\left(n\phi\right)e^{-jk_z z}\right) \tag{2.41}$$

$$= Ak_\rho B_n^{e'}\left(k_\rho \rho\right)\cos\left(n\phi\right)e^{-jk_z z} \tag{2.42}$$

$$E_z = 0 \tag{2.43}$$

$$H_\rho = \frac{1}{j\omega\mu}\frac{\partial^2 \psi}{\partial \rho \partial z} \tag{2.44}$$

$$= \frac{1}{j\omega\mu}\frac{\partial}{\partial \rho}\left[\frac{\partial}{\partial z}\left(AB_n^e\left(k_\rho \rho\right)\cos\left(n\phi\right)e^{-jk_z z}\right)\right] \tag{2.45}$$

$$= -\frac{Ak_z k_\rho}{\omega\mu}B_n^e\left(k_\rho \rho\right)\cos\left(n\phi\right)e^{-jk_z z} \tag{2.46}$$

$$H_\phi = \frac{1}{j\omega\mu}\frac{1}{\rho}\frac{\partial^2 \psi}{\partial \phi \partial z} \tag{2.47}$$

$$= \frac{1}{j\omega\mu}\frac{1}{\rho}\frac{\partial}{\partial \phi}\left[\frac{\partial}{\partial z}\left(AB_n^e\left(k_\rho \rho\right)\cos\left(n\phi\right)e^{-jk_z z}\right)\right] \tag{2.48}$$

$$= \frac{Ank_z}{\omega\mu\rho}B_n^e\left(k_\rho \rho\right)\sin\left(n\phi\right)e^{-jk_z z} \tag{2.49}$$

$$H_z = \frac{1}{j\omega\mu}\left(\frac{\partial^2}{\partial z^2} + k^2\right)\psi \tag{2.50}$$

$$= \frac{1}{j\omega\mu}\left(\frac{\partial^2}{\partial z^2} + k^2\right)(AB_n^e\left(k_\rho \rho\right)\cos\left(n\phi\right)e^{-jk_z z}) \tag{2.51}$$

$$= \frac{A}{j\omega\mu}\left(k^2 - k_z^2\right)(B_n^e\left(k_\rho \rho\right)\cos\left(n\phi\right)e^{-jk_z z}) \tag{2.52}$$

Next, the magnetic field components will be solved for where, here, we will use the formulas for field components for a TM$^z$ cylindrical coordinate system. Same as with the electric field components, they will be the same for each dielectric region because the Bessel functions have been left generic until later except for the constants out front. For finding the field components here the constant $B$ will be used as a stand-in for $B$ and $D$ for the core and cladding regions respectively.

$$\begin{aligned}
E_\rho &= \frac{1}{j\omega\epsilon}\frac{\partial^2\psi}{\partial\rho\partial z} && (2.53)\\
&= \frac{1}{j\omega\epsilon}\frac{\partial}{\partial\rho}\left[\frac{\partial}{\partial z}\left(BB_n^m\left(k_\rho\rho\right)\sin\left(n\phi\right)e^{-jk_z z}\right)\right] && (2.54)\\
&= -\frac{Bk_z k_\rho}{\omega\epsilon}B_n^{m\prime}\left(k_\rho\rho\right)\sin\left(n\phi\right)e^{-jk_z z} && (2.55)\\
E_\phi &= \frac{1}{j\omega\epsilon}\frac{1}{\rho}\frac{\partial^2\psi}{\partial\phi\partial z} && (2.56)\\
&= \frac{1}{j\omega\epsilon}\frac{\partial}{\partial\phi}\left[\frac{\partial}{\partial z}\left(BB_n^m\left(k_\rho\rho\right)\sin\left(n\phi\right)e^{-jk_z z}\right)\right] && (2.57)\\
&= -\frac{Bnk_z}{\omega\epsilon}B_n^m\left(k_\rho\rho\right)\cos\left(n\phi\right)e^{-jk_z z} && (2.58)\\
E_z &= \frac{1}{j\omega\epsilon}\left(\frac{\partial^2}{\partial z^2}+k^2\right)\psi && (2.59)\\
&= \frac{1}{j\omega\epsilon}\left(\frac{\partial^2}{\partial z^2}+k^2\right)\left(BB_n^m\left(k_\rho\rho\right)\sin\left(n\phi\right)e^{-jk_z z}\right) && (2.60)\\
&= \frac{B}{j\omega\epsilon}\left(k^2-k_z^2\right)\left(B_n^m\left(k_\rho\rho\right)\sin\left(n\phi\right)e^{-jk_z z}\right) && (2.61)
\end{aligned}$$

$$\begin{aligned}
H_\rho &= \frac{1}{\rho}\frac{\partial\psi}{\partial\phi} && (2.62)\\
&= \frac{1}{\rho}\frac{\partial}{\partial\phi}\left(BB_n^m\left(k_\rho\rho\right)\sin\left(n\phi\right)e^{-jk_z z}\right) && (2.63)\\
&= \frac{Bn}{\rho}B_n^m\left(k_\rho\rho\right)\cos\left(n\phi\right)e^{-jk_z z} && (2.64)\\
H_\phi &= -\frac{\partial\psi}{\partial\rho} && (2.65)\\
&= -\frac{\partial}{\partial\rho}\left(BB_n^m\left(k_\rho\rho\right)\sin\left(n\phi\right)e^{-jk_z z}\right) && (2.66)\\
&= -Bk_\rho B_n^{m\prime}\left(k_\rho\rho\right)\sin\left(n\phi\right)e^{-jk_z z} && (2.67)\\
H_z &= 0 && (2.68)
\end{aligned}$$

### 2.5.4 Apply boundary conditions

In applying the boundary conditions to the previously solved for field components we know without needing to perform the appropriate calculations that the sinusoidal and exponential terms will cancel each other out as they are the same for each of the dielectric regions. It is just the coefficients and Bessel functions that must be related. First the tangential boundary condition for the electric field as given in (2.69) will be applied.

$$E_{\phi_1}\left(\rho = a\right) = E_{\phi_2}\left(\rho = a\right) \tag{2.69}$$

$$\begin{aligned} A k_{\rho_1} B_n^{e_1\prime}\left(k_{\rho_1} a\right) + \frac{B}{j\omega\epsilon_1 a}\left(-jk_z\right) n B_n^{m_1}\left(k_{\rho_1} a\right) = \\ C k_{\rho_2} B_n^{e_2\prime}\left(k_{\rho_2} a\right) + \frac{D}{j\omega\epsilon_2 a}\left(-jk_z\right) n B_n^{m_2}\left(k_{\rho_2} a\right) \end{aligned} \tag{2.70}$$

$$A k_{\rho_1} B_n^{e_1\prime}\left(k_{\rho_1} a\right) - \frac{nBk_z}{\omega\epsilon_1 a} B_n^{m_1}\left(k_{\rho_1} a\right) = C k_{\rho_2} B_n^{e_2\prime}\left(k_{\rho_2} a\right) - \frac{nDk_z}{\omega\epsilon_2 a} B_n^{m_2}\left(k_{\rho_2} a\right)$$

Next the boundary condition for the electric field as given in (2.71) will be applied.

$$E_{z_1}\left(\rho = a\right) = E_{z_2}\left(\rho = a\right) \tag{2.71}$$

$$\frac{1}{j\omega\epsilon_1}\left(k_1^2 - k_z^2\right)\left[B B_n^{m_1}\left(k_{\rho_1} a\right)\right] = \frac{1}{j\omega\epsilon_2}\left(k_2^2 - k_z^2\right)\left[D B_n^{m_2}\left(k_{\rho_2} a\right)\right] \tag{2.72}$$

$$k_{\rho_1}^2 B B_n^{m_1}\left(k_{\rho_1} a\right) = k_{\rho_2}^2 D B_n^{m_2}\left(k_{\rho_2} a\right) \tag{2.73}$$

Next the boundary condition for the magnetic field as given in (2.74) will be applied.

$$H_{\phi_1}\left(\rho = a\right) = H_{\phi_2}\left(\rho = a\right) \tag{2.74}$$

$$\begin{aligned} \frac{A}{j\omega\mu_1 a} njk_z B_n^{e1}\left(k_{\rho_1}a\right) + \left(-k_{\rho_1}B\right) B_n^{m_1\prime}\left(k_{\rho_1}a\right) = \\ \frac{C}{j\omega\mu_2 a} njk_z B_n^{e2}\left(k_{\rho_2}a\right) + \left(-k_{\rho_2}D\right) B_n^{m_2\prime}\left(k_{\rho_2}a\right) \\ \frac{nk_z A}{\omega\mu_1 a} B_n^{e1}\left(k_{\rho_1}a\right) - k_{\rho_1} B B_n^{m_1\prime}\left(k_{\rho_1}a\right) = \frac{nk_z C}{\omega\mu_2 a} B_n^{e2}\left(k_{\rho_2}a\right) - k_{\rho_2} D B_n^{m_2\prime}\left(k_{\rho_2}a\right) \end{aligned} \tag{2.75}$$

Last, the boundary condition for the magnetic field as given in (2.76) will be applied.

$$H_{z_1}(\rho = a) = H_{z_2}(\rho = a) \tag{2.76}$$

$$\frac{1}{j\omega\mu_1}\left(k_1^2 - k_z^2\right)\left[AB_n^{e1}\left(k_{\rho_1}a\right)\right] = \frac{1}{j\omega\mu_2}\left(k_2^2 - k_z^2\right)\left[CB_n^{e2}\left(k_{\rho_2}a\right)\right] \tag{2.77}$$

$$k_{\rho_1}^2 AB_n^{e1}\left(k_{\rho_1}a\right) = k_{\rho_2}^2 CB_n^{e2}\left(k_{\rho_2}a\right) \tag{2.78}$$

### 2.5.5 Solve for characteristic equation

To solve for the characteristic equation a linear system of equations from the relations found when applying the boundary conditions must be formed. From the linear system of equations a matrix relating the equation terms can be arranged and taking the determinant of that matrix will yield the characteristic equation. Choosing specific Bessel Functions will still be delayed and the definitions in (2.79) will be set.

$$\begin{aligned} F_1 &= B_n^{e1}\left(k_{\rho_1}a\right) \\ F_2 &= B_n^{m_1}\left(k_{\rho_1}a\right) \\ F_3 &= B_n^{e2}\left(k_{\rho_2}a\right) \\ F_4 &= B_n^{m_2}\left(k_{\rho_2}a\right) \end{aligned} \tag{2.79}$$

Here, a system of equations is formed to solve for the unknown coefficients:

$$\begin{aligned}
A\,(0) + B\left(k_{\rho_1}^2 F_2\right) + C\,(0) - D\left(k_{\rho_2}^2 F_4\right) &= 0 \\
A\left(k_{\rho_1}^2 F_1\right) + B\,(0) - C\left(k_{\rho_2}^2 F_3\right) + D\,(0) &= 0 \\
A\left(k_{\rho_1} F_1'\right) - B\left(\frac{nk_z}{\omega\epsilon_1 a} F_2\right) - C\left(k_{\rho_2} F_3'\right) + D\left(\frac{nk_z}{\omega\epsilon_2 a} F_4\right) &= 0 \\
A\left(\frac{nk_z}{\omega\mu_1 a} F_1\right) - B\left(k_{\rho_1} F_2'\right) - C\left(\frac{nk_z}{\omega\mu_2 a} F_3\right) + D(k_{\rho_2} F_4') &= 0
\end{aligned}$$

Which can be written in matrix form as:

$$\begin{bmatrix} 0 & k_{\rho_1}^2 F_2 & 0 & -k_{\rho_2}^2 F_4 \\ k_{\rho_1}^2 F_1 & 0 & -k_{\rho_2}^2 F_3 & 0 \\ k_{\rho_1} F_1' & -\frac{nk_z}{\omega\epsilon_1 a} F_2 & -k_{\rho_2} F_3' & \frac{nk_z}{\omega\epsilon_2 a} F_4 \\ \frac{nk_z}{\omega\mu_1 a} F_1 & -k_{\rho_1} F_2' & -\frac{nk_z}{\omega\mu_2 a} F_3 & k_{\rho_2} F_4' \end{bmatrix} \begin{bmatrix} A \\ B \\ C \\ D \end{bmatrix} = 0$$

If $n = 0$ then the field separates into $\mathrm{TE}^{\mathrm{z}}$ and $\mathrm{TM}^{\mathrm{z}}$ modes:

$$\begin{bmatrix} 0 & k_{\rho_1}^2 F_2 & 0 & -k_{\rho_2}^2 F_4 \\ k_{\rho_1}^2 F_1 & 0 & -k_{\rho_2}^2 F_3 & 0 \\ k_{\rho_1} F_1' & 0 & -k_{\rho_2} F_3' & 0 \\ 0 & -k_{\rho_1} F_2' & 0 & k_{\rho_2} F_4' \end{bmatrix} \begin{bmatrix} A \\ B \\ C \\ D \end{bmatrix} = 0$$

which yields a TE characteristic equation of:

$$k_{\rho_2} F_1' F_3 - k_{\rho_1} F_1 F_3' = 0 \tag{2.80}$$

and a TM characteristic equation of:

$$k_{\rho_1} F_2 F_4' - k_{\rho_2} F_2' F_4 = 0 \tag{2.81}$$

However if $n \neq 0$, the $4 \times 4$ matrix can be broken down into 4, $3 \times 3$ and then into 6 $2 \times 2$ to solve as shown:

$$\left|\begin{bmatrix} 0 & b & 0 & d \\ e & 0 & g & 0 \\ i & j & k & l \\ m & n & o & p \end{bmatrix}\right| = 0$$

$$(0) - b\left|\begin{bmatrix} e & g & 0 \\ i & k & l \\ m & o & p \end{bmatrix}\right| + (0) = 0$$

$$-b\left(e\left|\begin{bmatrix} k & l \\ o & p \end{bmatrix}\right| - g\left|\begin{bmatrix} i & l \\ m & p \end{bmatrix}\right|\right) = 0$$

$$-b\left[e\left(kp - lo\right) - g\left(ip - lm\right)\right] = 0$$

$$e\left(kp - lo\right) - g\left(ip - lm\right) = 0$$

Plugging in values and simplifying:

$$\begin{aligned} e\left(kp - lo\right) - g\left(ip - lm\right) &= 0 \\ k_{\rho_1}^2 F_1\left[\left(-k_{\rho_2}F_3'\right)\left(k_{\rho_2}F_4'\right) - \left(\frac{nk_z}{\omega\epsilon_2 a}F_4\right)\left(\frac{-nk_z}{\omega\mu_2 a}F_3\right)\right] &= \\ -k_{\rho_2}^2 F_3\left[\left(k_{\rho_1}F_1'\right)\left(k_{\rho_2}F_4'\right) - \left(\frac{nk_z}{\omega\epsilon_2 a}F_4\right)\left(\frac{nk_z}{\omega\mu_1 a}F_1\right)\right] & \\ k_{\rho_1}^2 F_1\left[\frac{n^2k_z^2}{\omega^2\epsilon_2\mu_2 a^2}F_3F_4 - k_{\rho_2}^2F_3'F_4'\right] = -k_{\rho_2}^2F_3\left[k_{\rho_1}k_{\rho_2}F_1'F_4' - \frac{n^2k_z^2}{\omega^2\epsilon_2\mu_1 a^2}F_1F_4\right] & \end{aligned} \tag{2.82}$$

Lastly the Bessel functions can be chosen. Since the fields must be finite at $\rho = 0$ we will choose $F_1$ and $F_2 = J_n\left(k_{\rho_1}a\right)$. Additionally, since $E_z = 0$ at $\rho = b$ we can choose

$$F_4 = J_n\left(k_{\rho_2}a\right)N_n\left(k_{\rho_2}b\right) - N_n\left(k_{\rho_2}a\right)J_n\left(k_{\rho_2}b\right) \tag{2.83}$$

and as $E_\phi = 0$ at $\rho = b$ we can choose:

$$F_3 = J_n\left(k_{\rho_2}a\right)N_n'\left(k_{\rho_2}b\right) - N_n\left(k_{\rho_2}a\right)J_n'\left(k_{\rho_2}b\right) \tag{2.84}$$

Thus, making the final characteristic equation for the circular-cross section to be Equation 2.85.

$$k_{\rho_1}^2 F_1 \left[ \frac{n^2 k_z^2}{\omega^2 \epsilon_2 \mu_2 a^2} F_3 F_4 - k_{\rho_2}^2 F_3' F_4' \right] + k_{\rho_2}^2 F_3 \left[ k_{\rho_1} k_{\rho_2} F_1' F_4' - \frac{n^2 k_z^2}{\omega^2 \epsilon_2 \mu_1 a^2} F_1 F_4 \right] = 0 \tag{2.85}$$

## 2.6 Rectangular cross-section

### 2.6.1 Description of problem

In a very similar procedure as was performed in Section 2.5, the geometry for the guide of rectangular cross-section will be evaluated to determine its characteristic equation. The procedure most closely followed here can be found in [83]. Figure 2.14 shows the geometry to be used in this evaluation where three dielectric layers fill a metal waveguide. It is assumed that the materials boundaries do not overlap, that there are no air gaps between the layers, that the metal boundary is a perfect electrical conductor, that the dielectric materials are non-magnetic and isotropic, that the region is source free (homogeneous), and that the waveguide extends infinitely in the z-direction.

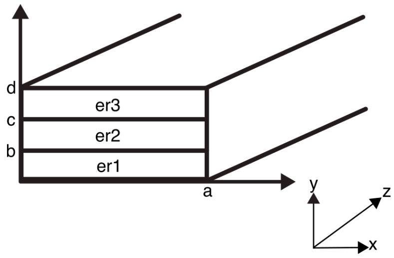

Figure 2.14: Problem geometry, walls of the waveguide are PEC and material is non-magnetic and perfectly fills the cross-section.

The geometry of the guide as it would be realized in a real implementation, as was shown in Figure 2.1, would have the middle dielectric layer narrower than the top and bottom layers. Although such a cross-section can be investigated using software tools or numerical methods, analytically it cannot be described in such a way as to result in a closed form solution for a characteristic equation. The core layer must fully extend to the waveguide walls in the y-direction or else the core-cladding boundary cannot be defined at the two points along the x-direction where the core and cladding would both exist. Extending the core layer to fully fill the guide is taken to be a valid simplification here because this simplification is used in the literature on ribbon waveguides and because the core layer is much wider than it is thick with an aspect ratio (ratio of width to height) of 9.5 used for the prototypes in this work.

### 2.6.2 Determining vector potentials

For a wave traveling in the positive z-direction in each dielectric region the wave potentials will be given as in (2.86)-(2.88) where the superscript of the potential denotes the dielectric region in which it is associated.

$$\begin{aligned}\psi_y^1\left(x, 0 \leq y \leq b, z\right) = &\left[C_1^1 \cos\left(\beta_{x_1} x\right) + D_1^1 \sin\left(\beta_{x_1} x\right)\right] \times \ldots \\ &\left[C_2^1 \cos\left(\beta_{y_1} y\right) + D_2^1 \sin\left(\beta_{y_1} y\right)\right] A_3^1 e^{-j\beta_z z}\end{aligned} \tag{2.86}$$

$$\begin{aligned}\psi_y^2\left(x, b \leq y \leq c, z\right) = &\left[C_1^2 \cos\left(\beta_{x_2} x\right) + D_1^2 \sin\left(\beta_{x_2} x\right)\right] \times \ldots \\ &\left[C_2^2 \cos\left(\beta_{y_2}\left[c - y\right]\right) + D_2^2 \sin\left(\beta_{y_2}\left[c - y\right]\right)\right] A_3^2 e^{-j\beta_z z}\end{aligned} \tag{2.87}$$

$$\begin{aligned}\psi_y^3\left(x, c \leq y \leq d, z\right) = &\left[C_1^3 \cos\left(\beta_{x_3} x\right) + D_1^3 \sin\left(\beta_{x_3} x\right)\right] \times \ldots \\ &\left[C_2^3 \cos\left(\beta_{y_3}\left[d - y\right]\right) + D_2^3 \sin\left(\beta_{y_3}\left[d - y\right]\right)\right] A_3^3 e^{-j\beta_z z}\end{aligned} \tag{2.88}$$

In (2.86)-(2.88) the propagation relations are further defined as in (2.89).

$$\begin{aligned}\beta_{x_1}^2 + \beta_{y_1}^2 + \beta_z^2 &= \beta_1^2 = \omega\mu_1\epsilon_1 \\ \beta_{x_2}^2 + \beta_{y_2}^2 + \beta_z^2 &= \beta_2^2 = \omega\mu_2\epsilon_2 \\ \beta_{x_3}^2 + \beta_{y_3}^2 + \beta_z^2 &= \beta_3^2 = \omega\mu_3\epsilon_3\end{aligned} \tag{2.89}$$

### 2.6.3 Define boundary conditions and solve for field components

The independent boundary conditions are defined in (2.90) - (2.98). The superscript denotes the dielectric region in which the field resides.

$$E_z^1\left(0,0 \le y \le b,z\right) = E_z^1\left(a,0 \le y \le b,z\right) = 0 \tag{2.90}$$

$$E_z^2\left(0,b \le y \le c,z\right) = E_z^2\left(a,b \le y \le c,z\right) = 0 \tag{2.91}$$

$$E_z^3\left(0,c \le y \le d,z\right) = E_z^3\left(a,c \le y \le d,z\right) = 0 \tag{2.92}$$

$$E_z^1\left(0 \le x \le a,0,z\right) = 0 \tag{2.93}$$

$$E_z^3\left(0 \le x \le a,d,z\right) = 0 \tag{2.94}$$

$$E_z^1\left(0 \le x \le a,b,z\right) = E_z^2\left(0 \le x \le a,b,z\right) \tag{2.95}$$

$$E_z^2\left(0 \le x \le a,c,z\right) = E_z^3\left(0 \le x \le a,c,z\right) \tag{2.96}$$

$$H_z^1\left(0 \le x \le a,b,z\right) = H_z^2\left(0 \le x \le a,b,z\right) \tag{2.97}$$

$$H_z^2\left(0 \le x \le a,c,z\right) = H_z^3\left(0 \le x \le a,c,z\right) \tag{2.98}$$

The equations for TE$^y$ modes can be used, as can be found in (2.99), to solve for the field components necessary to apply the boundary conditions.

$$\begin{aligned}
E_x &= \frac{1}{\epsilon}\frac{\partial\psi}{\partial z} \\
E_y &= 0 \\
E_z &= -\frac{1}{\epsilon}\frac{\partial\psi}{\partial x} \\
H_x &= -j\frac{1}{\omega\mu\epsilon}\frac{\partial^2\psi}{\partial x\partial y} \\
H_y &= -j\frac{1}{\omega\mu\epsilon}\left(\frac{\partial^2}{\partial y^2}+\beta^2\right)\psi \\
H_z &= -j\frac{1}{\omega\mu\epsilon}\frac{\partial^2\psi}{\partial y\partial z}
\end{aligned} \tag{2.99}$$

The electric field components in the z-direction are found as shown in (2.100)-(2.102).

$$\begin{aligned}
E_z^1 = -\frac{\beta_{x_1}}{\epsilon_1}&\left[-C_1^1\sin\left(\beta_{x_1}x\right)+D_1^1\cos\left(\beta_{x_1}x\right)\right]\times\ldots \\
&\left[C_2^1\cos\left(\beta_{y_1}y\right)+D_2^1\sin\left(\beta_{y_1}y\right)\right]A_3^1 e^{-j\beta_z z}
\end{aligned} \tag{2.100}$$

$$\begin{aligned}E_z^2 &= -\frac{\beta_{x_2}}{\epsilon_2}\left[-C_1^2 \sin\left(\beta_{x_2} x\right) + D_1^2 \cos\left(\beta_{x_2} x\right)\right] \times \ldots \\ &\left[C_2^2 \cos\left(\beta_{y_2}\left[c-y\right]\right) + D_2^2 \sin\left(\beta_{y_2}\left[c-y\right]\right)\right] A_3^2 e^{-j\beta_z z}\end{aligned} \tag{2.101}$$

$$\begin{aligned}E_z^3 &= -\frac{\beta_{x_3}}{\epsilon_3}\left[-C_1^3 \sin\left(\beta_{x_3} x\right) + D_1^3 \cos\left(\beta_{x_3} x\right)\right] \times \ldots \\ &\left[C_2^3 \cos\left(\beta_{y_3}\left[d-y\right]\right) + D_2^3 \sin\left(\beta_{y_3}\left[d-y\right]\right)\right] A_3^3 e^{-j\beta_z z}\end{aligned} \tag{2.102}$$

### 2.6.4 Apply boundary conditions

First the boundary conditions where the tangential field must go to zero will be applied and used to simplify the vector field potentials and their associated electric field components. Then, the boundary conditions where the field must be continuous across a dielectric boundary will be applied to form a system of equations. First, the left-hand side of (2.90) will be applied to (2.100) resulting in (2.103)

$$E_z^1\left(0, 0 \le y \le b, z\right) = -\frac{\beta_{x_1}}{\epsilon_1}\left[0 + D_1^1\right] \times \left[C_2^1 \cos\left(\beta_{y_1} y\right) + D_2^1 \sin\left(\beta_{y_1} y\right)\right] A_3^1 e^{-j\beta_z z} = 0 \tag{2.103}$$

which implies that $D_1^1 = 0$. Further, applying the right-hand side of (2.90) to (2.100) yields (2.104)

$$\begin{aligned}E_z^1\left(a, 0 \le y \le b, z\right) &= -\frac{\beta_{x_1}}{\epsilon_1}\left[-C_1^1 \sin\left(\beta_{x_1} a\right)\right] \times \ldots \\ &\left[C_2^1 \cos\left(\beta_{y_1} y\right) + D_2^1 \sin\left(\beta_{y_1} y\right)\right] A_3^1 e^{-j\beta_z z} = 0\end{aligned} \tag{2.104}$$

which implies that $\sin\left(\beta_{x_1} a\right) = 0$ so $\beta_{x_1} = \frac{m\pi}{a}$ where $(m = 0, 1, 2 \ldots)$. Likewise, applying the similar boundary conditions in regions 2 and 3 will results in $D_1^1 = D_1^2 = D_1^3 = 0$ and $\beta_{x_1} = \beta_{x_2} = \beta_{x_3} = \frac{m\pi}{a}$ where $(m = 0, 1, 2 \ldots)$ [84]. Next, (2.93) can be applied to yield (2.105)

$$E_z^1\left(0 \le x \le a, 0, z\right) = -\frac{\beta_{x_1}}{\epsilon_1}\left[-C_1^1 \sin\left(\beta_{x_1} x\right)\right] \times \left[C_2^1\right] A_3^1 e^{-j\beta_z z} = 0 \tag{2.105}$$

which implies that $C_2^1 = 0$. Likewise applying (2.94) will result in $C_2^3 = 0$. These findings allow the wave potentials to be simplified as seen in (2.106)-(2.108).

$$\psi_y^1\left(x, 0 \leq y \leq b, z\right) = A_3^1 \cos\left(\beta_{x_1} x\right) \sin\left(\beta_{y_1} y\right) e^{-j\beta_z z} \tag{2.106}$$

$$\begin{gathered}\psi_y^2\left(x, b \leq y \leq c, z\right) = A_3^2 \cos\left(\beta_{x_2} x\right) \times \ldots \\ \left[C_2^2 \cos\left(\beta_{y_2}\left[c - y\right]\right) + D_2^2 \sin\left(\beta_{y_2}\left[c - y\right]\right)\right] e^{-j\beta_z z}\end{gathered} \tag{2.107}$$

$$\psi_y^3\left(x, c \leq y \leq d, z\right) = A_3^3 \cos\left(\beta_{x_3} x\right) \sin\left(\beta_{y_3}\left[d - y\right]\right) e^{-j\beta_z z} \tag{2.108}$$

where the propagation relations are also simplified to (2.109).

$$\begin{aligned}\left(\frac{m\pi}{a}\right)^2 + \beta_{y_1}^2 + \beta_z^2 = \beta_1^2 = \omega\mu_1\epsilon_1 \\ \left(\frac{m\pi}{a}\right)^2 + \beta_{y_2}^2 + \beta_z^2 = \beta_2^2 = \omega\mu_2\epsilon_2 \\ \left(\frac{m\pi}{a}\right)^2 + \beta_{y_3}^2 + \beta_z^2 = \beta_3^2 = \omega\mu_3\epsilon_3\end{aligned} \tag{2.109}$$

Thus allowing the electric field components to be re-found as shown in (2.110).

$$\begin{aligned}E_z^1 &= \frac{\beta_{x_1}}{\epsilon_1} A_3^1 \sin\left(\beta_{x_1} x\right) \sin\left(\beta_{y_1} y\right) e^{-j\beta_z z} \\ E_z^2 &= \frac{\beta_{x_2}}{\epsilon_2} A_3^2 \sin\left(\beta_{x_2} x\right) \times \left[C_2^2 \cos\left(\beta_{y_2}\left[c - y\right]\right) + D_2^2 \sin\left(\beta_{y_2}\left[c - y\right]\right)\right] e^{-j\beta_z z} \\ E_z^3 &= \frac{\beta_{x_3}}{\epsilon_3} A_3^3 \sin\left(\beta_{x_3} x\right) \sin\left(\beta_{y_3}\left[d - y\right]\right) e^{-j\beta_z z}\end{aligned} \tag{2.110}$$

Now, the boundary conditions will be applied beginning with (2.95) which results in (2.111).

$$\frac{\beta_{x_1}}{\epsilon_1} A_3^1 \sin\left(\beta_{y_1} b\right) = \frac{\beta_{x_2}}{\epsilon_2} A_3^2 \times \left[C_2^2 \cos\left(\beta_{y_2}\left[c - b\right]\right) + D_2^2 \sin\left(\beta_{y_2}\left[c - b\right]\right)\right] \tag{2.111}$$

Where, for the purposes of simplification and later organizing terms into a system of four equations with four unknowns, new unknown constants will be defined where $A_3^2 \times C_2^2 = F_2$ and $A_3^2 \times D_2^2 = G_2$ so that (2.111) can be written as in (2.112).

$$\frac{\beta_{x_1}}{\epsilon_1} A_3^1 \sin\left(\beta_{y_1} b\right) = \frac{\beta_{x_2}}{\epsilon_2}\left[F_2 \cos\left(\beta_{y_2}\left[c-b\right]\right) + G_2 \sin\left(\beta_{y_2}\left[c-b\right]\right)\right] \tag{2.112}$$

Next, (2.96) will be applied resulting in (2.113) which, using the same definitions as were used to simplify (2.111) into (2.112), can be simplified into (2.114).

$$\frac{\beta_{x_2}}{\epsilon_2} A_3^2 \times \left[C_2^2\right] = \frac{\beta_{x_3}}{\epsilon_3} A_3^3 \sin\left(\beta_{y_1}\left[d-c\right]\right) \tag{2.113}$$

$$\frac{\beta_{x_2}}{\epsilon_2} F_2 = \frac{\beta_{x_3}}{\epsilon_3} A_3^3 \sin\left(\beta_{y_3}\left[d-c\right]\right) \tag{2.114}$$

To continue applying the tangential field boundary conditions the H-field z-components must first be found as can be seen in (2.115).

$$\begin{aligned} H_z^1 &= -\frac{\beta_{y_1}\beta_z}{\omega\mu_1\epsilon_1} A_3^1 \cos\left(\beta_{x_1} x\right)\cos\left(\beta_{y_1} y\right) e^{-j\beta_z z} \\ H_z^2 &= -\frac{\beta_{y_2}\beta_z}{\omega\mu_2\epsilon_2} A_3^2 \cos\left(\beta_{x_2} x\right)\left[C_2^2 \sin\left(\beta_{y_2}\left[c-y\right]\right) - D_2^2 \cos\left(\beta_{y_2}\left[c-y\right]\right)\right] e^{-j\beta_z z} \\ H_z^3 &= \frac{\beta_{y_3}\beta_z}{\omega\mu_3\epsilon_3} A_3^3 \cos\left(\beta_{x_3} x\right)\cos\left(\beta_{y_3}\left[d-y\right]\right) e^{-j\beta_z z} \end{aligned} \tag{2.115}$$

Then, (2.97) can be applied resulting in (2.116) and further simplified with the redefined coefficients in (2.117).

$$\frac{\beta_{y_1}}{\mu_1\epsilon_1} A_3^1 \cos\left(\beta_{y_1} b\right) = \frac{\beta_{y_2}}{\mu_2\epsilon_2} A_3^2 \left[C_2^2 \sin\left(\beta_{y_2}\left[c-b\right]\right) - D_2^2 \cos\left(\beta_{y_2}\left[c-b\right]\right)\right] \tag{2.116}$$

$$\frac{\beta_{y_1}}{\mu_1\epsilon_1} A_3^1 \cos\left(\beta_{y_1} b\right) = \frac{\beta_{y_2}}{\mu_2\epsilon_2}\left[F_2 \sin\left(\beta_{y_2}\left[c-b\right]\right) - G_2 \cos\left(\beta_{y_2}\left[c-b\right]\right)\right] \tag{2.117}$$

Lastly, (2.98) can be applied resulting in (2.118) and simplified with the redefined constants as (2.119).

$$\frac{\beta_{y_2}}{\mu_2\epsilon_2} A_3^2 \left[-D_2^2\right] = \frac{\beta_{y_3}}{\mu_3\epsilon_3} A_3^3 \cos\left(\beta_{y_3}\left[d-c\right]\right) \tag{2.118}$$

$$-\frac{\beta_{y_2}}{\mu_2\epsilon_2}G_2 = \frac{\beta_{y_3}}{\mu_3\epsilon_3}A_3^3\cos\left(\beta_{y_3}\left[d-c\right]\right) \tag{2.119}$$

### 2.6.5 Solve for characteristic equation

Now a system of four equations with four unknowns has been established and system can be solved for the characteristic equation. It is additionally known that $\beta_{x_1} = \beta_{x_2} = \beta_{x_3}$, so the system of equations can be written as in (2.120).

$$\begin{aligned}
\frac{1}{\epsilon_1}A_3^1\sin\left(\beta_{y_1}b\right) &= \frac{1}{\epsilon_2}\left[F_2\cos\left(\beta_{y_2}\left[c-b\right]\right) + G_2\sin\left(\beta_{y_2}\left[c-b\right]\right)\right]\\
\frac{1}{\epsilon_2}F_2 &= \frac{1}{\epsilon_3}A_3^3\sin\left(\beta_{y_3}\left[d-c\right]\right)\\
\frac{\beta_{y_1}}{\mu_1\epsilon_1}A_3^1\cos\left(\beta_{y_1}b\right) &= \frac{\beta_{y_2}}{\mu_2\epsilon_2}\left[F_2\sin\left(\beta_{y_2}\left[c-b\right]\right) - G_2\cos\left(\beta_{y_2}\left[c-b\right]\right)\right]\\
-\frac{\beta_{y_2}}{\mu_2\epsilon_2}G_2 &= \frac{\beta_{y_3}}{\mu_3\epsilon_3}A_3^3\cos\left(\beta_{y_3}\left[d-c\right]\right)
\end{aligned} \tag{2.120}$$

This system of equations can be seen in matrix form where $A_3^1 = A$, $F_2 = B$, $G_2 = C$, and $A_3^3 = D$ in (2.121) (which has been presented in a landscape view to fully fit in a page).

$$\begin{bmatrix} \frac{1}{\epsilon_1}\sin\left(\beta_{y_1} b\right) & -\frac{1}{\epsilon_2}\cos\left(\beta_{y_2}\left[c-b\right]\right) & -\frac{1}{\epsilon_2}\sin\left(\beta_{y_2}\left[c-b\right]\right) & 0 \\ \frac{\beta_{y_1}}{\mu_1\epsilon_1}\cos\left(\beta_{y_1} b\right) & -\frac{\beta_{y_2}}{\mu_2\epsilon_2}\sin\left(\beta_{y_2}\left[c-b\right]\right) & \frac{\beta_{y_2}}{\mu_2\epsilon_2}\cos\left(\beta_{y_2}\left[c-b\right]\right) & 0 \\ 0 & 0 & -\frac{\beta_{y_2}}{\mu_2\epsilon_2} & -\frac{\beta_{y_3}}{\mu_3\epsilon_3}\cos\left(\beta_{y_3}\left[d-c\right]\right) \\ 0 & \frac{1}{\epsilon_2} & 0 & -\frac{1}{\epsilon_3}\sin\left(\beta_{y_3}\left[d-c\right]\right) \end{bmatrix} \begin{bmatrix} A \\ B \\ C \\ D \end{bmatrix} = 0 \qquad (2.121)$$

To solve for the determinant, which results in the characteristic equation, the determinant of a $4 \times 4$ matrix will be broken up into 4 $3 \times 3$ matrices and those further into 6 $2 \times 2$ matrices as shown in (2.122).

$$\begin{aligned}
\left|\begin{bmatrix} a & b & c & 0 \\ e & f & g & 0 \\ 0 & 0 & k & l \\ 0 & n & 0 & p \end{bmatrix}\right| &= 0 \\
a\left|\begin{bmatrix} f & g & 0 \\ 0 & k & l \\ n & 0 & p \end{bmatrix}\right| - b\left|\begin{bmatrix} e & g & 0 \\ 0 & k & l \\ 0 & 0 & p \end{bmatrix}\right| + c\left|\begin{bmatrix} e & f & 0 \\ 0 & 0 & l \\ 0 & n & p \end{bmatrix}\right| &= 0 \\
a\left(f\left|\begin{bmatrix} k & l \\ 0 & p \end{bmatrix}\right| - g\left|\begin{bmatrix} 0 & l \\ n & p \end{bmatrix}\right|\right) - b\left(e\left|\begin{bmatrix} k & l \\ 0 & p \end{bmatrix}\right| - g\left|\begin{bmatrix} 0 & l \\ 0 & p \end{bmatrix}\right|\right) + \ldots & \\
c\left(e\left|\begin{bmatrix} 0 & l \\ n & p \end{bmatrix}\right| - f\left|\begin{bmatrix} 0 & l \\ 0 & p \end{bmatrix}\right|\right) &= 0 \\
a\left[f\left(kp\right) + g\left(ln\right)\right] - b\left[e\left(kp\right)\right] - c\left[e\left(ln\right)\right] &= 0 \\
a\left[f\left(kp\right) + g\left(ln\right)\right] &= e\left[b\left(kp\right) - c\left(ln\right)\right]
\end{aligned} \tag{2.122}$$

Plugging values into (2.122) for the left hand side of the equation results in (2.123) and simplifying results further in (2.124).

$$\begin{aligned}
&\frac{1}{\epsilon_1}\sin\left(\beta_{y_1} b\right)\Bigg[-\frac{\beta_{y_2}}{\mu_2\epsilon_2}\sin\left(\beta_{y_2}\left[c-b\right]\right)\left(-\frac{\beta_{y_2}}{\mu_2\epsilon_2}\cdot -\frac{1}{\epsilon_3}\sin\left(\beta_{y_3}\left[d-c\right]\right)\right) + \ldots \\
&\qquad \frac{\beta_{y_2}}{\mu_2\epsilon_2}\cos\left(\beta_{y_2}\left[c-b\right]\right)\left(\frac{1}{\epsilon_2}\cdot -\frac{\beta_{y_3}}{\mu_3\epsilon_3}\cos\left(\beta_{y_3}\left[d-c\right]\right)\right)\Bigg]
\end{aligned} \tag{2.123}$$

$$\begin{aligned}
&\frac{\beta_{y_2}}{\epsilon_1\epsilon_2^2\epsilon_3\mu_2}\sin\left(\beta_{y_1} b\right)\Bigg[-\frac{\beta_{y_2}}{\mu_2}\sin\left(\beta_{y_2}\left[c-b\right]\right)\sin\left(\beta_{y_3}\left[d-c\right]\right) - \ldots \\
&\qquad \frac{\beta_{y_3}}{\mu_3}\cos\left(\beta_{y_2}\left[c-b\right]\right)\cos\left(\beta_{y_3}\left[d-c\right]\right)\Bigg]
\end{aligned} \tag{2.124}$$

Plugging values into (2.122) for the right hand side of the equation results in (2.125) and simplifying results further in (2.126).

$$\begin{aligned}\frac{\beta_{y_1}}{\mu_1\epsilon_1}\cos\left(\beta_{y_1}b\right)\Bigg[&-\frac{\beta_{y_2}}{\mu_2\epsilon_2}\left(-\frac{1}{\epsilon_2}\cos\left(\beta_{y_2}[c-b]\right)\right)\left(-\frac{1}{\epsilon_3}\sin\left(\beta_{y_3}[d-c]\right)\right)+\dots\\ &\frac{1}{\epsilon_2}\left(\frac{1}{\epsilon_2}\sin\left(\beta_{y_2}[c-b]\right)\right)\left(-\frac{\beta_{y_3}}{\mu_3\epsilon_3}\cos\left(\beta_{y_3}[d-c]\right)\right)\Bigg]\end{aligned} \tag{2.125}$$

$$\begin{aligned}\frac{\beta_{y_1}}{\mu_1\epsilon_1\epsilon_2^2\epsilon_3}\cos\left(\beta_{y_1}b\right)\Bigg[&-\frac{\beta_{y_2}}{\mu_2}\cos\left(\beta_{y_2}[c-b]\right)\sin\left(\beta_{y_3}[d-c]\right)+\dots\\ &\frac{\beta_{y_3}}{\mu_3}\sin\left(\beta_{y_2}[c-b]\right)\cos\left(\beta_{y_3}[d-c]\right)\Bigg]\end{aligned} \tag{2.126}$$

Setting the two sides equal to each other results in (2.127).

$$\begin{aligned}-\frac{\mu_1\beta_{y_2}\sin\left(\beta_{y_1}b\right)}{\mu_2\beta_{y_1}\cos\left(\beta_{y_1}b\right)}&=\dots\\ \frac{\left[-\frac{\beta_{y_2}}{\mu_2}\cos\left(\beta_{y_2}[c-b]\right)\sin\left(\beta_{y_3}[d-c]\right)+\frac{\beta_{y_3}}{\mu_3}\sin\left(\beta_{y_2}[c-b]\right)\cos\left(\beta_{y_3}[d-c]\right)\right]}{\left[\frac{\beta_{y_2}}{\mu_2}\sin\left(\beta_{y_2}[c-b]\right)\sin\left(\beta_{y_3}[d-c]\right)+\frac{\beta_{y_3}}{\mu_3}\cos\left(\beta_{y_2}[c-b]\right)\cos\left(\beta_{y_3}[d-c]\right)\right]}&\end{aligned} \tag{2.127}$$

(2.127) can be simplified, and for this specific scenario $\mu_1 = \mu_2 = \mu_3 = \mu_o$, into (2.128).

$$\begin{aligned}-\frac{\beta_{y_2}}{\beta_{y_1}}\tan\left(\beta_{y_1}b\right)&=\dots\\ \frac{\left[\beta_{y_3}\sin\left(\beta_{y_2}[c-b]\right)\cos\left(\beta_{y_3}[d-c]\right)-\beta_{y_2}\cos\left(\beta_{y_2}[c-b]\right)\sin\left(\beta_{y_3}[d-c]\right)\right]}{\left[\beta_{y_3}\cos\left(\beta_{y_2}[c-b]\right)\cos\left(\beta_{y_3}[d-c]\right)+\beta_{y_2}\sin\left(\beta_{y_2}[c-b]\right)\sin\left(\beta_{y_3}[d-c]\right)\right]}&\end{aligned} \tag{2.128}$$

where:

$$\begin{aligned}
\beta_{y_1} &= \sqrt{\beta_1^2 - \left(\frac{m\pi}{a}\right)^2 - \beta_z^2} \\
\beta_{y_2} &= \sqrt{\beta_2^2 - \left(\frac{m\pi}{a}\right)^2 - \beta_z^2} \\
\beta_{y_3} &= \sqrt{\beta_3^2 - \left(\frac{m\pi}{a}\right)^2 - \beta_z^2} \\
\beta_1 &= \omega^2 \mu_1 \epsilon_1 \\
\beta_2 &= \omega^2 \mu_2 \epsilon_2 \\
\beta_3 &= \omega^2 \mu_3 \epsilon_3
\end{aligned} \tag{2.129}$$

As a sanity check for (2.128), if $\epsilon_1 = \epsilon_2 = \epsilon_3$ and $b = c = d$ then $\beta_1 = \beta_2 = \beta_3$ and would allow (2.128) to simplify to $\tan\left(\beta_y d\right) = 0$ which would lead to $beta_y = \frac{n\pi}{d}$ which is as would be expected from common electromagnetic textbooks.

### 2.6.6 Numerically validate FEM results

The theoretical work can thus be used to validate the results seen using FEM software HFSS in order to be able to trust the results obtained and used from HFSS for the bulk of the work in this thesis. Using a homemade Python code which utilizes a Newton's Method solver to find roots for the characteristic equations solved for by hand the propagation phase and attenuation can be compared to HFSS results for the fundamental mode. As seen in Figure 2.15 the left side of the figure compares propagation phase results and the right hand side compares attenuation constants where the top row are results found numerically using the Python code and the bottom row are results from HFSS. Subset into the plots are the rectangular guide cross-sections that are used in the models and equations to realize the results, so, although these are not a direct one-to-one comparison we can see that (1) the results agree well and (2) the approximation made in finding the theoretical characteristic equation where the middle dielectric layer was extended to the sidewalls for the guide of rectangular cross-section was reasonable. The annotations in red point out equivalent points on the comparible plots in Figure 2.15. These results allow us to have confidence in HFSS results moving forward. The Python code used for these plots can be seen in Appendix A

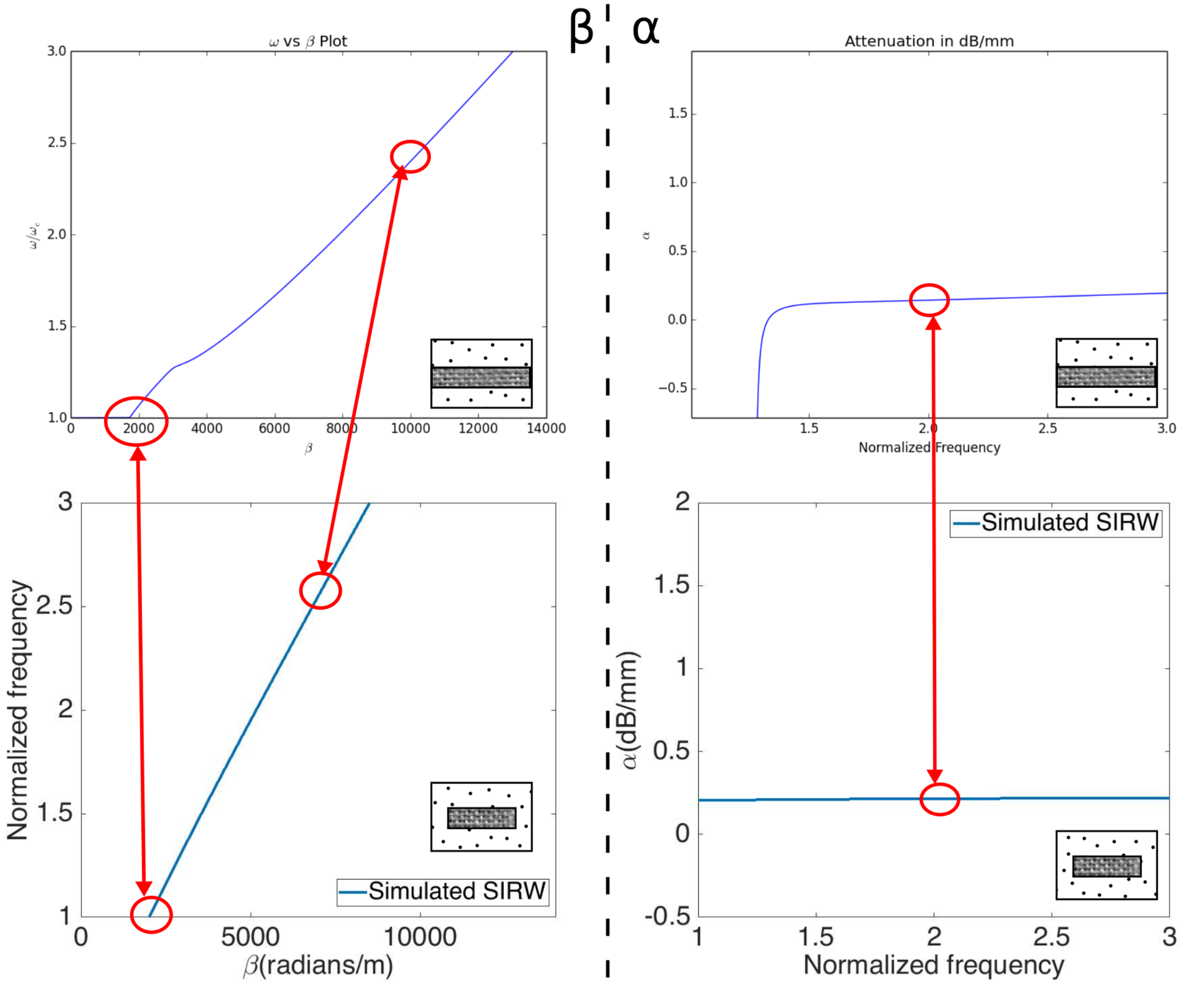

Figure 2.15: Plots from.

### 2.6.7 Additional considerations: cut-off frequency, impedance, and power carried

Additional analytical expressions are found for the guide of rectangular cross-section as this geometry is more likely to be of interest for use given that its planar profile could be substrate integration compatible.

The cut off frequency can also be estimated by knowing that it will exist somewhere between that of an empty metallic guide (upper bound) and that of one completely filled with the highest dielectric constant material used (lower bound) for the same cross-section area. The cut off frequency for a rectangular waveguide can be found from (2.130).

$$f_{c_{mn}} = \frac{1}{2\pi\sqrt{\mu\epsilon}}\sqrt{\left(\frac{m\pi}{a}\right)^2 + \left(\frac{n\pi}{b}\right)^2} \tag{2.130}$$

An expression for the total power carried by the guide and the guides impedance can also be found. In order to find these, the electric field component in the x-direction and the magnetic field component in the y-direction will be required using the formulas in (2.99). Each dielectric region will have its own field component where the superscripts indicate the dielectric region.

$$\begin{aligned} E_x^1 = \frac{\beta_z}{\epsilon_1 j}\left[C_1^1\cos\left(\beta_{x_1}x\right) + D_1^1\sin\left(\beta_{x_1}x\right)\right]\times\dots \\ \left[C_2^1\cos\left(\beta_{y_1}y\right) + D_2^1\sin\left(\beta_{y_1}y\right)\right]A_3^1 e^{-j\beta_z z} \end{aligned} \tag{2.131}$$

$$\begin{aligned} E_x^2 = \frac{\beta_z}{\epsilon_2 j}\left[C_1^2\cos\left(\beta_{x_2}x\right) + D_1^2\sin\left(\beta_{x_2}x\right)\right]\times\dots \\ \left[C_2^2\cos\left(\beta_{y_2}\left[c-y\right]\right) + D_2^2\sin\left(\beta_{y_2}\left[c-y\right]\right)\right]A_3^2 e^{-j\beta_z z} \end{aligned} \tag{2.132}$$

$$\begin{aligned} E_x^3 = \frac{\beta_z}{\epsilon_3 j}\left[C_1^3\cos\left(\beta_{x_3}x\right) + D_1^3\sin\left(\beta_{x_3}x\right)\right]\times\dots \\ \left[C_2^3\cos\left(\beta_{y_3}\left[d-y\right]\right) + D_2^3\sin\left(\beta_{y_3}\left[d-y\right]\right)\right]A_3^3 e^{-j\beta_z z} \end{aligned} \tag{2.133}$$

$$\begin{aligned} H_y^1 = \frac{1}{j\omega\mu_1\epsilon_1}\left(\beta_z^2 + \left(\frac{m\pi}{a}\right)^2\right)\left[C_1^1\cos\left(\beta_{x_1}x\right) + D_1^1\sin\left(\beta_{x_1}x\right)\right]\times\dots \\ \left[C_2^1\cos\left(\beta_{y_1}y\right) + D_2^1\sin\left(\beta_{y_1}y\right)\right]A_3^1 e^{-j\beta_z z} \end{aligned} \tag{2.134}$$

$$\begin{aligned} H_y^2 = \frac{1}{j\omega\mu_2\epsilon_2}\left(\beta_z^2 + \left(\frac{m\pi}{a}\right)^2\right)\left[C_1^2\cos\left(\beta_{x_2}x\right) + D_1^2\sin\left(\beta_{x_2}x\right)\right]\times\dots \\ \left[C_2^2\cos\left(\beta_{y_2}\left[c-y\right]\right) + D_2^2\sin\left(\beta_{y_2}\left[c-y\right]\right)\right]A_3^2 e^{-j\beta_z z} \end{aligned} \tag{2.135}$$

$$\begin{aligned} H_y^3 = \frac{1}{j\omega\mu_3\epsilon_3}\left(\beta_z^2 + \left(\frac{m\pi}{a}\right)^2\right)\left[C_1^3\cos\left(\beta_{x_3}x\right) + D_1^3\sin\left(\beta_{x_3}x\right)\right]\times\dots \\ \left[C_2^3\cos\left(\beta_{y_3}\left[d-y\right]\right) + D_2^3\sin\left(\beta_{y_3}\left[d-y\right]\right)\right]A_3^3 e^{-j\beta_z z} \end{aligned} \tag{2.136}$$

The wave impedance can be found by applying (2.137).

$$Z = \frac{E_x}{H_y} \tag{2.137}$$

Solving for an expression for impedance for the first dielectric region yields (2.138).

$$Z_1 = \frac{\omega \mu_1 \beta_z}{\left(\beta_z^2 + \left(\frac{m\pi}{a}\right)^2\right)} \tag{2.138}$$

Similar expressions can be found for the other two regions.

$$Z_2 = \frac{\omega \mu_2 \beta_z}{\left(\beta_z^2 + \left(\frac{m\pi}{a}\right)^2\right)} \tag{2.139}$$

$$Z_3 = \frac{\omega \mu_3 \beta_z}{\left(\beta_z^2 + \left(\frac{m\pi}{a}\right)^2\right)} \tag{2.140}$$

The total power carried by the guide will be the sum of the power carried in each of the three dielectric regions whose contributions will be calculated separately for clarity. The generalized expression for power carried can be seen in (2.141), and with some specifics in (2.142), but the specifics of the integrand must be found.

$$P = \frac{1}{2} Re \left( \oint_S \hat{n} \cdot \left[ \vec{E} \times \vec{H}^* \right] dxdy \right) \tag{2.141}$$

$$P = \frac{1}{2} Re \left( \int_0^a \int_0^d \hat{z} \cdot \left[ \vec{E} \times \vec{H}^* \right] dydx \right) \tag{2.142}$$

The integrand is expanded in (2.143) which reduced to (2.144).

$$\hat{z} \cdot [\vec{E} \times \vec{H}^*] = \hat{z} \cdot \left[ E_x H_y^* \hat{z} - E_x H_z^* \hat{y} - E_y H_x^* \hat{z} + E_y H_z^* \hat{x} + E_z H_x^* \hat{y} - E_z H_y^* \hat{x} \right] \tag{2.143}$$

$$\hat{z} \cdot [\vec{E} \times \vec{H}^*] = E_x H_y^* - E_y H_x^* \tag{2.144}$$

$E_y = 0$ by definition leaving (2.145).

$$P = \frac{1}{2} Re \left( \int_0^a \int_0^d E_x H_y^* dydx \right) \tag{2.145}$$

Solving for the power carried in region 1 the previously solved for field components can be substituted into (2.145) where the integrand for region 1 will be (2.146).

$$\begin{aligned} E_{x_1}H_{y_1}^* = \frac{\beta_z}{\omega\mu_1\epsilon_1^2}\left(A_3^1 e^{-j\beta_z z}\right)^2\left(\beta_z^2+\left(\frac{m\pi}{a}\right)^2\right)\left[C_1^1\cos(\beta_{x_1}x)+D_1^1\sin(\beta_{x_1}x)\right]^2\times\ldots \\ \left[C_2^1\cos(\beta_{y_1}y)+D_2^1\sin(\beta_{y_1}y)\right]^2 \end{aligned} \tag{2.146}$$

Additionally from applying the independent boundary conditions earlier it is known that $D_1^1 = D_1^2 = D_1^3 = 0$, $C_2^1 = 0$, and that $C_2^3 = 0$, also, all the unknown constants will be combined into one constant out front which correlates to the field amplitude. This allows the integrand to be simplified so that the power in region 1 can be found by (2.147).

$$\begin{aligned} P_1 = \frac{\beta_z}{2\omega\mu_1\epsilon_1^2}\left(A_{mn}^1 e^{-j\beta_z z}\right)^2\left(\beta_z^2+\left(\frac{m\pi}{a}\right)^2\right)\times\ldots \\ Re\left(\int_0^a\left[\cos(\beta_{x_1}x)\right]^2 dx\int_0^d\left[\sin(\beta_{y_1}y)\right]^2 dy\right) \end{aligned} \tag{2.147}$$

The integrals in (2.147) can easily be performed given the integration rules in (2.148) and (2.149).

$$\int \sin(a*x)^2 dx = \frac{x}{2}-\frac{\sin(2ax)}{4a} \tag{2.148}$$

$$\int \cos(a*x)^2 dx = \frac{2ax+\sin(2ax)}{4a} \tag{2.149}$$

the expression for power carried in region 1 can be found in (2.150) where $A_{mn}^1 = A_3^1\times C_1^1\times D_2^1$.

$$P_1 = Re\left(\frac{\beta_z}{2\omega\mu_1\epsilon_1^2}\left(A_{mn}^1 e^{-j\beta_z z}\right)^2\left(\beta_z^2+\left(\frac{m\pi}{a}\right)^2\right)\left[\frac{d}{2}-\frac{\sin(2\beta_{y_1}d)}{4\beta_{y_1}}\right]\left[\frac{2a\beta_{x_1}+\sin(2a\beta_{x_1})}{4\beta_{x_1}}\right]\right) \tag{2.150}$$

Next the expression for region 3 will be shown as it is very similar to region 1:

$$\begin{aligned} E_{x_3}H^*_{y_3} &= \frac{\beta_z}{\omega\mu_3\epsilon_3^2}\left(A_3^3 e^{-j\beta_z z}\right)^2\left(\beta_z^2+\left(\frac{m\pi}{a}\right)^2\right)\times\dots \\ &\left[C_1^3\cos(\beta_{x_3}x)+D_1^3\sin(\beta_{x_3}x)\right]^2\left[C_2^3\cos(\beta_{y_3}[d-y])+D_2^3\sin(\beta_{y_3}[d-y])\right]^2 \end{aligned} \tag{2.151}$$

$$\begin{aligned} P_3 &= \frac{\beta_z}{2\omega\mu_3\epsilon_3^2}\left(A_{mn}^3 e^{-j\beta_z z}\right)^2\left(\beta_z^2+\left(\frac{m\pi}{a}\right)^2\right)\times\dots \\ &Re\left(\int_0^a\left[\cos(\beta_{x_3}x)\right]^2dx\int_0^d\left[\sin(\beta_{y_3}[d-y])\right]^2dy\right) \end{aligned} \tag{2.152}$$

Using the same integral rules as in region 1:

$$\begin{aligned} P_3 = Re\Bigg(&\frac{\beta_z}{2\omega\mu_3\epsilon_3^2}\left(A_{mn}^3 e^{-j\beta_z z}\right)^2\left(\beta_z^2+\left(\frac{m\pi}{a}\right)^2\right)\times\dots \\ &\left[\frac{2\beta_{x_3}a+\sin(2\beta_{x_3}a)}{4\beta_{x_3}}\right]\left[-\frac{\sin(2d\beta_{y_3})-2d\beta_{y_3}}{4\beta_{y_3}}\right]\Bigg) \end{aligned} \tag{2.153}$$

where $A_{mn}^3 = A_3^3\times C_1^3\times D_2^3$.

Lastly the expression for region 2:

$$\begin{aligned} E_{x_2}H^*_{y_2} &= \frac{\beta_z}{\omega\mu_2\epsilon_2^2}\left(A_3^2 e^{-j\beta_z z}\right)^2\left(\beta_z^2+\left(\frac{m\pi}{a}\right)^2\right)\times\dots \\ &\left[C_1^2\cos(\beta_{x_2}x)+D_1^2\sin(\beta_{x_2}x)\right]^2\left[C_2^2\cos(\beta_{y_2}[c-y])+D_2^2\sin(\beta_{y_2}[c-y])\right]^2 \end{aligned} \tag{2.154}$$

Here we know $D_1^2 = 0$ but the boundary conditions do not remove the need for the $C_2^2$ constant:

$$\begin{aligned} P_2 = Re\Bigg(&\frac{\beta_z}{2\omega\mu_2\epsilon_2^2}\left(A_{mn}^2 e^{-j\beta_z z}\right)^2\left(\beta_z^2+\left(\frac{m\pi}{a}\right)^2\right)\int_0^a\left[\cos(\beta_{x_2}x)\right]^2dx\times\dots \\ &\int_0^d\left[C_2^2\cos(\beta_{y_2}[c-y])+D_2^2\sin(\beta_{y_2}[c-y])\right]^2dy\Bigg) \end{aligned} \tag{2.155}$$

Using the integration property from the prior two regions:

$$\begin{aligned} P_2 = Re\Bigg(&\frac{\beta_z}{2\omega\mu_2\epsilon_2^2}\left(A_{mn}^2 e^{-j\beta_z z}\right)^2\left(\beta_z^2+\left(\frac{m\pi}{a}\right)^2\right)\left[\frac{2\beta_{x_2}a+\sin(2a\beta_{x_2})}{4\beta_{x_2}}\right]\times\dots \\ &\int_0^d\left[C_2^2\cos(\beta_{y_2}[c-y])+D_2^2\sin(\beta_{y_2}[c-y])\right]^2dy\Bigg) \end{aligned} \tag{2.156}$$

For the integral with respect to $y$ we will expand the squared expression in order to break up the integral into three parts where:

$$P_2 = Re\left(K(P_2^1 + P_2^2 + P_2^3)\right) \tag{2.157}$$

$$K = \frac{\beta_z}{2\omega\mu_2\epsilon_2^2}\left(A_{mn}^2 e^{-j\beta_z z}\right)^2\left(\beta_z^2 + \left(\frac{m\pi}{a}\right)^2\right)\left[\frac{2\beta_{x_2}a + \sin(2a\beta_{x_2})}{4\beta_{x_2}}\right] \tag{2.158}$$

$$P_2^1 = (C_2^2)^2\int_0^d\left[\cos(\beta_{y_2}[c-y])\right]^2 dy = (C_2^2)^2\frac{-\sin(2\beta_{y_2}[c-d]) + \sin(2c\beta_{y_2}) + 2d\beta_{y_2}}{4\beta_{y_2}} \tag{2.159}$$

$$P_2^2 = C_2^2 D_2^2\int_0^d \cos(\beta_{y_2}[c-y])\sin(\beta_{y_2}[c-y])dy = C_2^2 D_2^2\frac{\cos(2\beta_{y_2}[c-d]) - \cos(2c\beta_{y_2})}{4\beta_{y_2}} \tag{2.160}$$

$$P_2^3 = (D_2^2)^2\int_0^d\left[\sin(\beta_{y_2}[c-y])\right]^2 dy = (D_2^2)^2\frac{\sin(2\beta_{y_2}[c-d]) - \sin(2c\beta_{y_2}) + 2d\beta_{y_2}}{4\beta_{y_2}} \tag{2.161}$$

The total power carried is:

$$P_{total} = P_1 + P_2 + P_3 \tag{2.162}$$

## 2.7 Numerical results for discussion on modes

### 2.7.1 Modes in the proposed guide of rectangular cross-section

The characteristic equations and other expressions found in Section 2.5 and 2.6 could be implemented in MATLAB or Python codes to extract information on the propagating modes that could be supported by the proposed waveguides. Some exploration of this topic will be carried out using finite element method solver ANSYS HFSS®. To get specific mode information such as whether the modes are TE, TM, or some hybrid as well as their specific indices does require some prior knowledge of what to expect from the user if specific integration lines are to be defined within the model. Here, when defining modal excitation waveports in the ANSYS model, the user can select whether to keep additional modes with no specific mode defined. In theory HFSS could be run to include an infinite number of modes but here the search is limited to the first 10 in order to explain the trend in behavior.

Given the simulations included here the aim is to: (1) explain the observed behavior with the waveguide whose dimensions match that which was fabricated and measured as well as (2) show that with more ideal dimensions a waveguide with could operate at a single mode for a wide bandwidth. To support this effort four models were simulated, at 100 GHz, the guide of rectangular cross-section as it was fabricated and the guide with the core layer removed were solved. Additionally a model of a ribbon waveguide with better proportioned core and cladding layers (following dimensions as in [85] with a core thickness of 100 µm and cladding thickness of 250 µm) as well as the same guide with a metalized layer as is proposed in this work were solved. In Figure 2.16 illustrations of the four models are shown and below them their first 10 modes as visualized on the waveports of the simulated structures. It is clear that the the modes excited in the guide are affected by the core layer as well as by the metalized walls but do not strictly follow what would be expected from a homogenous filled guide or a traditional dielectric ribbon. As expected, the fundamental mode is the same as that of a ribbon waveguide and, in simulation, this fundamental mode was the only mode which showed power being transmitted.

Although not addressed in this work, depending on how the proposed waveguide is fed or excited only the the fundamental mode could be excited. However, for implementations which include bends it is possible to couple into or excite other higher order modes when the signal passes through. Ideally, the guide could be designed so at a large bandwidth of frequencies there is only one mode which could be supported. Figure 2.17 shows the simulated real parts of the propagation constant for the first 10 modes in the guide of rectangular cross-section with dimensions as was fabricated versus one with the dimensions of a traditional ribbon waveguide (a core thickness of

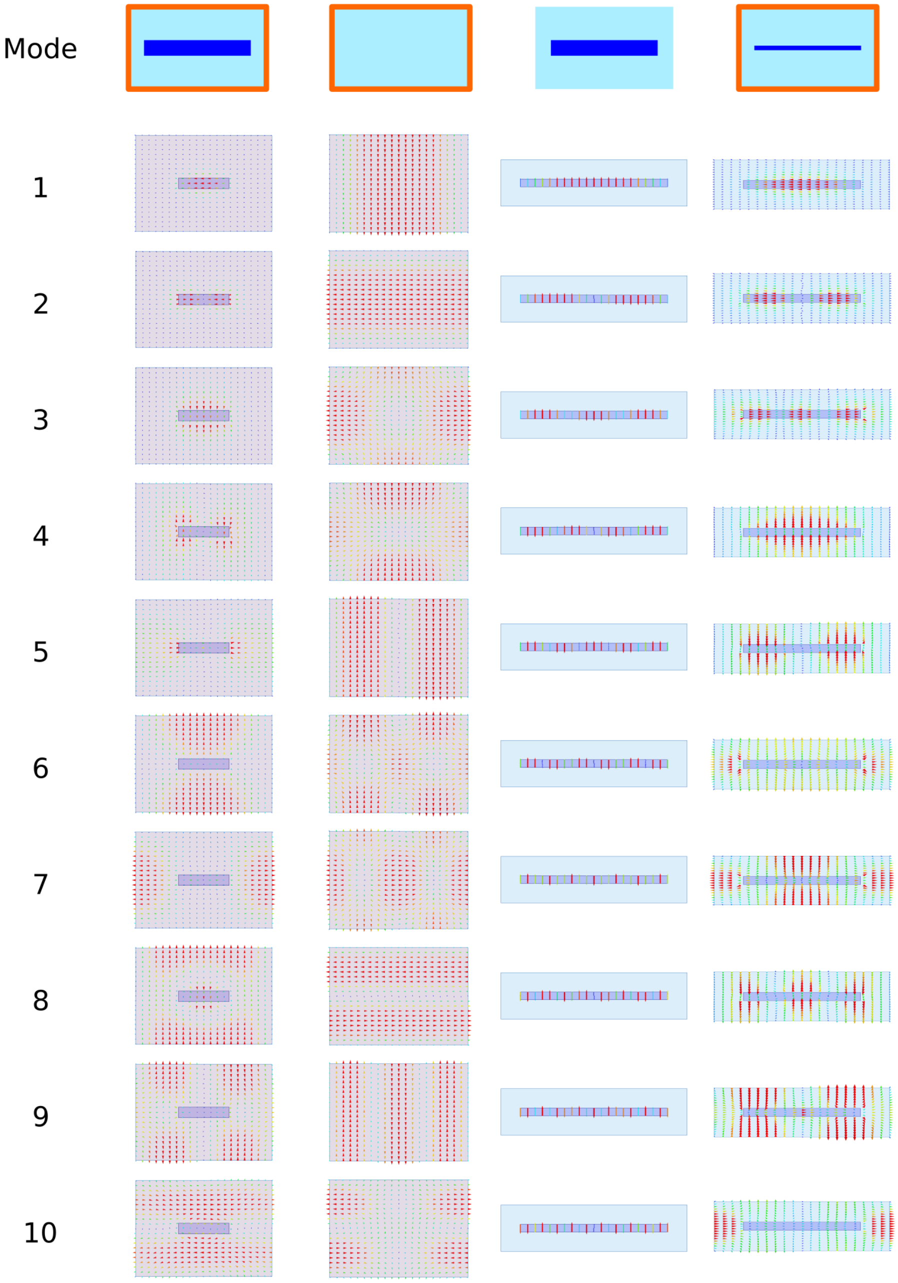

Figure 2.16: FEM results when including the first 10 modes for the guide of rectangular cross-section as fabricated, the guide dimensions as fabricated without the core layer, a ribbon waveguide, and a ribbon waveguide metalized as proposed.

100 µm and cladding thickness of 250 µm). By adjusting the dimensions the cut off frequency is obviously raised as would be expected by the smaller cross-section but the bandwidth available

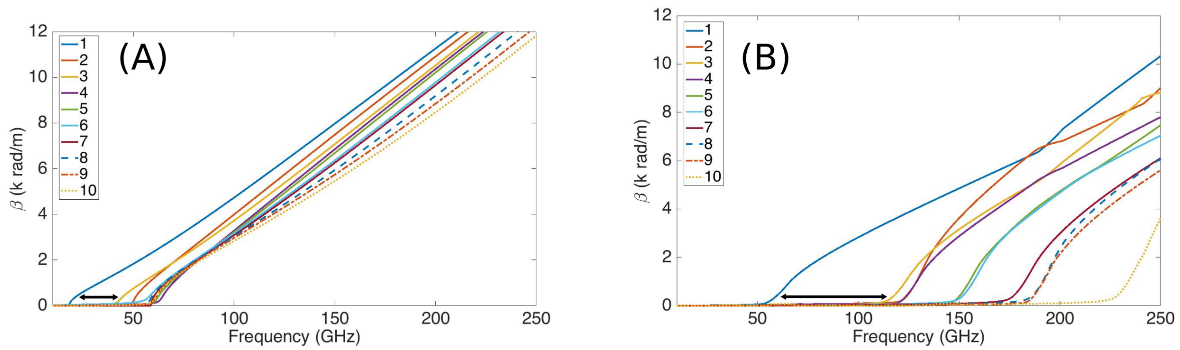

Figure 2.17: FEM results for the real part of the propagation constant ($\beta$) for (A) the guide of rectangular cross-section as was fabricated and (B) with dimensions of a traditional ribbon waveguide.

until the next mode would be excited is significantly larger. By optimizing the core and cladding dimensions or ratios greater control could be exerted over when higher order modes become present.

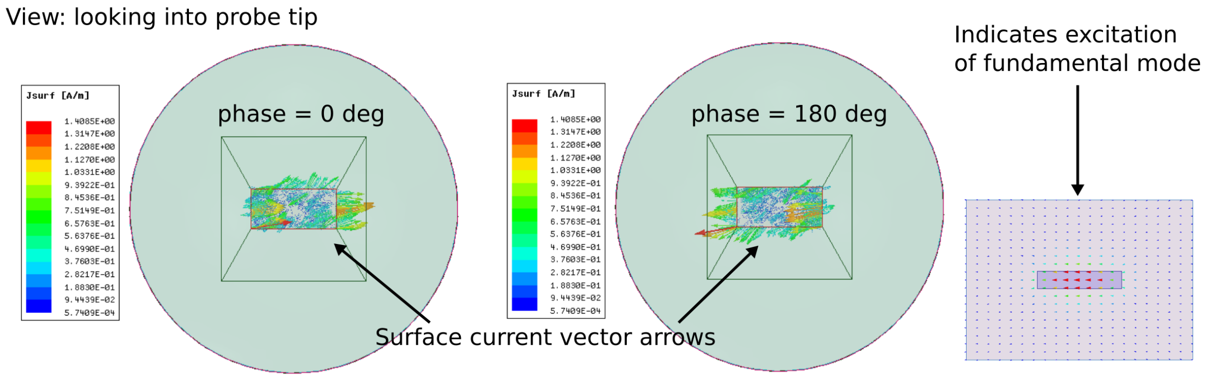

Figure 2.18: FEM results for the probes used to measure the guides of rectangular cross-section when solved at 100 GHz. The surface currents were plotted on the probe tip face and can be compared to the fundamental mode of the guide.

### 2.7.2 Modes in the measurement probes of rectangular cross-section

Given that the guides as fabricated can support higher order modes to better understand what is being measured in Section 2.2.2 the probes used for measurement of the rectangular cross-section were simulated at 100 GHz. As shown in Figure 2.18 the vector surface currents were plotted on a sheet at the probe tip face and they oscillated along the tips widest dimension (left to right, and right to left) as indicated by the two images capturing the currents 180 degrees out of phase. The probe tip dimensions directly match with the rectangular cross-section guides face. The mode seen in simulation this behavior best matches is the fundamental mode, as shown in the lower right of Figure 2.18. However, it could also have excited higher order modes seen in simulation such as mode 7 or 10 (and possibly others not included). However, the higher order modes which match the excited currents reaching the waveguide are, in simulation, primarily supported by interaction with the metal sidewalls which, in reality, would die out quickly given the conductor losses incurred at the frequencies at which the waveguides were being measured. Thus, it is likely the signal measured for the fabricated devices can be attributed to the fundamental mode.

## 2.8 Conclusion

A new waveguide design is demonstrated that is compatible with wafer, or substrate, level integration, and provides low dispersion and loss. Although 3D printing is used to realize the proposed waveguide, it is not used for the high dielectric constant material. As discussed in [86], although 3D printing methodologies do not yet yield RF devices that exceed, or in some cases meet, the performance of more traditional methods, one of the main limiting factors is the materials available for use for the existing additive manufacturing technologies. As works such as [69] push towards commercially available high dielectric materials, and given that some high end 3D printers can already print conductive layers, this structure would be able to be fully 3D printed once low-loss high dielectric printable materials are commercially available. 3D printing is compatible with wafer or substrate level integration which is its key advantage as a fabrication process for dielectric, especially multi-dielectric, based waveguides for future high speed needs.

Frequency domain measurements were carried out over a frequency range of 100 to 500 GHz. Simulation results also show good electric field confinement through bends and the possibilities of further reducing propagation loss through gradient dielectric substrates as advances in additive manufacturing continue. Results could be further improved by using a dielectric cladding material with a lower dielectric loss. The VeroWhitePlus® used here has a loss tangent of 0.04, but if a different fabrication technique was invoked such as injection molding a lower loss material such as low or high density polyethylene (HDPE) which has a similar dielectric constant but substantially lower loss tangent could be used. The difference in the propagation phase and loss constants for the proposed structures when using lower loss materials can be seen from the simulation results for the structures when VeroWhitePlus® is used, and when the Rogers material is used in the section investigating gradient dielectrics. The behavior seen in simulation and measurement results match to what is expected from the theoretical discussion of dielectric loaded waveguides and show that these waveguides can be used for high speed, low dispersion 100 Gb/s interconnects for the next generation of digital systems. As mentioned earlier, typical losses for a traditional 50 Ω microstrip are 0.2 dB/mm at 10 GHz where here, a simulated propagation loss of approximately 0.2 dB/mm was found for both cross-sections and measured around 0.15 and 0.05 for the rectangular and circular cross-sections respectively across the 100-500 GHz range investigated making this proposed waveguiding structure competitive for use in high-speed circuits and systems. Although we do note to the reader that these values serve to show that the guide is low loss but should not be taken as an absolute given the uncertainty in the THz measurement system used to obtain them. Overall, the measurements do show good agreement with what is expected from simulation.

# CHAPTER 3

# FABRICATION

## 3.1 Overview

In this chapter, the fabrication process used for making the substrate integrated ribbon waveguides (SIRW) in this thesis will be outlined. This will also include some additional detail on the type of 3D printing technology that was overwhelmingly used in this work. However, much of the work that led to the fabrication process used was part of a greater exploration of using low-cost, additive manufacturing fabrication techniques to realize RF and millimeter wave circuits. This work is also briefly discussed here and includes the application of a Nicholson-Ross-Weir (NRW) routine to perform material characterization of 3D printed plastics, additively manufacturing substrates with an air-core substrate to reduce the loss incurred due to the lossy materials used for 3D plastic printing, and using 3D printing to make injection molds for manufacturing THz passive components. Overall the work presented on fabrication methods here offers low-cost, low-complexity fabrication techniques to create RF and millimeter wave components.

## 3.2 Fundamentals of stereolithography

Stereolithography (SLA) is one of the many different technologies used for commercial 3D printers. This process prints a model layer by layer by invoking a photopolymerization process whereby the application of light, typically ultra-violet (UV) light, is used to cause chains of molecules to link together to form polymers. These polymers then form the desired 3D printed structure as the build material is applied and selectively cured in a layer by layer process.

The specific 3D printer used throughout this work is an Objet Connex350 3D printer from Stratasys Ltd. as can be seen in Figure 3.1 (A). Additionally, an illustration from [2] can be seen in Figure 3.1 (B) where the Objet print head can be filled with multiple different materials and support material to create any given final prototype. This printer has a build volume of 350×350×200 mm

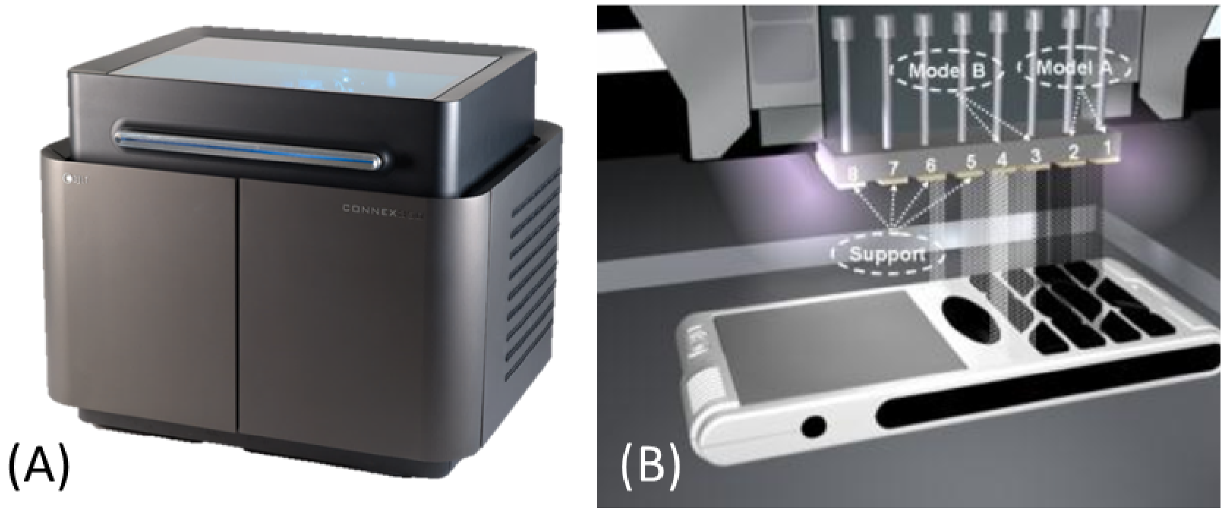

Figure 3.1: The printer used in this work, the (A) Objet Connex350 and (B) an illustration of how the printer prints from [2].

and on its high quality printing mode can print at its finest resolution 16 µm thick layers (thereby building a part at 12 mm per hour). The Objet Connex can print 600×600 dpi in the X and Y-axis with thin walls down to 0.6 mm.

Although one of the main selling points of this product line of 3D printers is its ability to be loaded with and print multiple materials within a single print run, this feature is not used in this work. The various materials available for this printer vary greatly in many physical or mechanical properties (after undergoing the photopolymerization process of course) but they are not so different in their electrical properties. As will be investigated in Section 3.4 most of the materials available here have very similar dielectric properties and so the Stratasys product VeroWhitePlus® was used as the predominant build material for this work as it was found among those available to have the lowest dielectric loss.

Stereolithographic additive manufacturing techniques as described here and used in this work also provide a solution to integrate components at the wafer or substrate level. Substrate and wafer level design relies on the passive and active structures to be planar in form. The integration of non-planar structures such as traditional rectangular metal waveguides would require planar to non-planar transitions or complex mounting structures. There types of solutions often require high

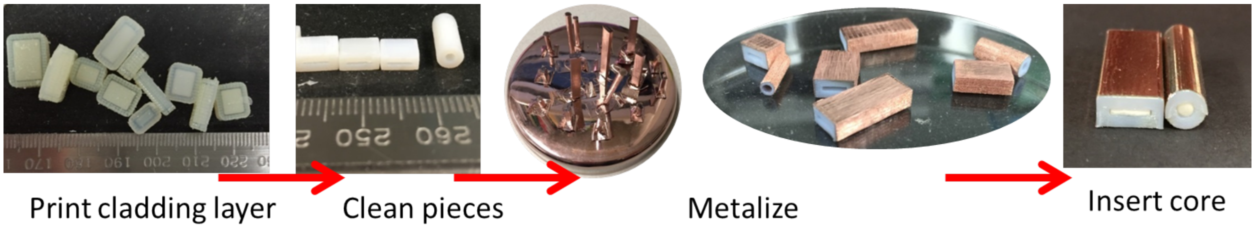

Figure 3.2: Visualization of the general fabrication process for the waveguiding structures made in this work.

precision tuning or adjustment which makes them ill suited for mass production. When employing 3D printing, the proposed waveguiding structure could be printed directly onto a wafer or substrate or, in the case of a substrate, the entire substrate could be printed entirely using 3D printed plastics as in [87] which would allow seamless integration.

## 3.3 Substrate integrated ribbon waveguide fabrication process

### 3.3.1 Process used for the work in this thesis

The general process used to fabricate the proposed waveguiding structures' prototypes is shown in Figure 3.2. Although other methods have been well demonstrated in the literature for fabricating ribbon waveguides part of the work in this thesis is exploring the utilization of additive manufacturing to create low-cost, high frequency circuits. Therefore, an additive manufacturing approach will be used here. The dielectric materials available to 3D print are limited, as will be further discussed in Section 3.4, and typically have dielectric constants around 2 - 3. Therefore, here they are used as the cladding material only and the core material will be commercially available alumina rods that are hand cut to length.

In order to fabricate the device prototypes, the cladding dimensions were first exported from ANSYS HFSS® and printed on a professional grade, commercially available 3D printer using the photo-polymer resin VeroWhitePlus®. A Stratasys Objet Connex350 printer was used which prints using a material jetting (polyjet) process where the build material is added layer by layer in a liquid form and then selectively cured with UV light as discussed in Section 3.2. The build material,

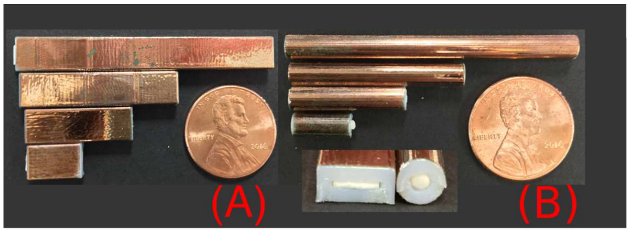

Figure 3.3: Fabricated devices as compared to a penny: finished (A) rectangular waveguides and (B) cylindrical waveguides of length (bottom to top) 10, 20, 30, and 50 mm where the inset shows their cross-sections.

VeroWhitePlus®, is a rigid opaque mainly comprised of poly(isobornyl acrylate) and poly(methyl methacrylate) with a low dielectric constant ($\epsilon_r$ = 2.8) and relatively low loss (tan$\delta$ = 0.04) at lower terahertz frequencies. The material properties used here for VeroWhitePlus®, for the THz range, were reported in [88] which also agrees with characterization work done at lower frequencies in [89] which is discussed in greater detail in Section 3.4. The printer used has the capability to print layers as fine as 16 µm, and has a 600 dpi resolution in the XY plane with up to 200 µm accuracy for a full model size thus making the overall feature size achievable fine enough to be a good tool for manufacturing parts intended for use with THz frequency geometries.

After the cladding parts were printed, they were coated with a layer of titanium (Ti, 250 nm), followed by a layer of copper (Cu, 1 µm), using a Denton Vacuum Desktop Pro sputtering system. The Ti layer is used to promote adhesion between the copper and dielectric substrate. The alumina cores were machined to size by hand using a Dremel rotary tool and then inserted into the cladding to complete the waveguides. Finished products can be seen in Figure 3.3. Some air gap is visible at the ends of the waveguides due to the reduction in the ends geometry to smooth the area that had been cut to length, however, through the length of the waveguide the fit between the core and cladding is snug with minimal air gap.

### 3.3.2 Proposed methods for future

In the future, there are other steps in fabrication that could be taken to significantly improve the device performance. First, the most obvious option, is having access to better materials. One way to do this would be to eschew additive manufacturing entirely and use more traditional methods to first make a ribbon waveguide and then simply metalize it after wards. Another way would be to make use of the not commercially available work to 3D print tailored dielectric constant materials [69] so that the core and cladding are using lower loss dielectrics *and* both layers are 3D printed so as to eliminate any issues with air gaps or imperfect boundaries between the two layers. Additionally, a low-loss material could have been used as cladding while minimizing any discontinuity between the two dielectric layers by using an injection molding process to apply the cladding layer around the core.

It is also now possible, since undertaking the work reported in this thesis, to purchase and use as support material, for an SLA printer as was used in this work, that can be dissolved in an acetone solution. This would have improved the cleaning of the 3D printed parts and therefore reduced any losses due to support material still being present, even if in small amounts, inside the waveguides and would have allowed a cleaner plastic on the outside to aid in the metallization step.

## 3.4 Material characterization

### 3.4.1 Background

Given the recent interest in using AM for RF circuits, there is a need to characterize the constitutive parameters of common materials used in commercially available 3D printers. Although preliminary work has been done in this area [90], one of the most popular materials being used that has not been characterized is Stratasys photo-polymer resin VeroWhitePlus®, a rigid opaque mainly comprised of poly(isobornyl acrylate) and poly(methyl methacrylate). Some prior work has evaluated the materials dielectric constant and loss tangent from 0.1 to 0.8 THz [88] using the method outlined in [30]. It was found that the dielectric constant was between 2.73 - 2.81 and the loss tangent between 0.012 - 0.05 from 0.1 to 0.8 THz respectively. These results do not necessarily apply to lower frequencies, making it necessary to characterize this polymer at a lower frequency range for ongoing projects related to 3D printing at lower frequencies. More importantly, the facilities available for this work in this thesis do not have the capabilities to replicate the methods used in

[88, 30] thus requiring an alternative method be used to evaluate the materials available for use in this work.

### 3.4.2 Methods

Here, the well known transmission/reflection method as proposed by Nicholson-Ross-Weir (NRW) [91, 92] is used to solve for the complex permittivity. Additionally, since it is known that VeroWhitePlus® is a passive material, or purely dielectric, the permeability of the material has a value of 1. Since this permeability value can be assumed, the permittivity can also be extracted by only using a transmission measurement. By using the same system of equations in NRW to solve for a theoretical transmission coefficient, which is only dependent on permittivity, and comparing it to the measured transmission coefficient, the permittivity can be solved for iteratively using a root solver [93]. Both NRW and the iterative epsilon extraction (IEE) method were used to find the permittivity in this work and an explanation of their algorithms can be found in Appendix C as well as the implementation of them in MATLAB code in Appendix D and E respectively.

A reference material, Teflon, is measured along with different VeroWhitePlus® samples in the S-Band (2 - 4 GHz). All samples of VeroWhitePlus® were printed on the same Object Connex350 printer. A sample of VeroWhitePlus® printed in early September of 2016 (VWP Old), a sample printed in late February 2017 (VWP New), a sample printed and then cured for an additional 10 minutes in a UV oven (VWP Cure), and a sample printed and then given a warm bath in copper sulphate for 15 minutes directly before measuring (VWP Wet) were all measured and the data processed using both methods.

Samples were measured in an S-Band waveguide from Maury Microwave using an Agilent Technologies ENA Series Network Analyzer E5071C. The system was calibrated using a manufacturer provided STL kit and details of calibration and measurement procedures can be found in Appendix B. Each sample was printed slightly larger than the sample holder cross section and then sanded down to size so that it fit as tightly as possible in the guide. Samples were measured seven times and for each measurement the sample was removed and reinserted into the guide. Results were analyzed using MATLAB and are the average of the seven measurements. Results showing the real part of the complex permittivity and the loss tangent using the NRW method and the real part of the dielectric constant using the iterative epsilon extraction solver can be seen in Table 3.1.

### 3.4.3 Results of VeroWhitePlus dielectric properties

The material properties of Teflon are well-known, having a dielectric constant of 2.1 and loss tangent of around 0.0005. Although NRW is reliable for finding the dielectric constant, one of the shortcomings of NRW is that it is unreliable for yielding loss information when a material is low loss [93, 94]. A low loss dielectric is typically defined as one whose loss tangent is below 0.01, although some people report loss tangents as high as 0.03 as low loss [90]. As can be seen in the results presented here, the loss information for Teflon, a very low loss material, is clearly inaccurate. Given this knowledge and the discrepancy of the results seen for VeroWhitePlus®, one can conjecture that VeroWhitePlus® is also low loss enough to not be characterized reliably using this measurement technique. To get a true value for its loss tangent, a different material characterization method such as using a resonant cavity would have to be used. However, results for the loss tangent found using the NRW method were still included given how well they agree with other published results [95].

In investigating the dielectric constant of VeroWhitePlus® (VWP), it can be seen that the value is relatively stable at about 2.8 - 2.9 for either method of processing the data and for all the tested samples. Since electronics and RF circuits is not the target market for 3D printer material manufacturers there was a question over how consistent the dielectric constant would be between batches of the material. The VWP Old and New samples were printed six months apart and from different batches of the material. Given that there was not a significant difference between the dielectric constant of the two batches it can give confidence that this property of the material could be consistent.

In processing RF circuits using VeroWhitePlus® material, often metallization is accomplished via an electroplating process. During this process, the VeroWhitePlus® substrate is submerged in

|  |  | 2.8 GHz |  | 3.2 GHz |  | 3.6 GHz |  |
|---|---|---|---|---|---|---|---|
|  |  | NRW | IEE | NRW | IEE | NRW | IEE |
| Teflon | $\epsilon_r$ | 2.01 | 2.23 | 2.03 | 2.15 | 2.07 | 2.1 |
|  | $\tan\delta$ | 0.03 | - | 0.04 | - | 0.04 | - |
| VWP Old | $\epsilon_r$ | 2.85 | 2.95 | 2.91 | 2.85 | 2.99 | 2.81 |
|  | $\tan\delta$ | 0.02 | - | 0.03 | - | 0.05 | - |
| VWP New | $\epsilon_r$ | 2.85 | 2.94 | 2.89 | 2.83 | 2.95 | 2.79 |
|  | $\tan\delta$ | 0.02 | - | 0.04 | - | 0.06 | - |
| VWP Cure | $\epsilon_r$ | 2.86 | 2.95 | 2.90 | 2.84 | 2.97 | 2.81 |
|  | $\tan\delta$ | 0.02 | - | 0.04 | - | 0.06 | - |
| VWP Wet | $\epsilon_r$ | 2.83 | 2.79 | 2.92 | 2.79 | 2.96 | 2.79 |
|  | $\tan\delta$ | 0.02 | - | 0.01 | - | 0.05 | - |

Table 3.1: Material characterization results for various VeroWhitePlus® samples.

a warm bath in copper sulphate which could possibly contaminate the substrate. Measurements of VWP Wet, after air dry, show that this processing does not greatly affect the material properties. Additionally, samples were weighted and all four VeroWhitePlus® samples were found to be the same weight, 52.1 g, at the time of measurement, which indicates that there was a negligible, if any, amount of moisture trapped in the VeroWhitePlus® from this processing.

Lastly, there is a possibility in the 3D printing process that the sample may not be fully cured during print which could affect the material properties. By giving a sample additional cure time it can be seen whether VeroWhitePlus® samples are fully cured at the end of their manufacturing. Our results show that this is the case. Overall, the results show that when using VeroWhitePlus® as a substrate for RF circuits the material maintains its dielectric properties, throughout potential processing, to have a dielectric constant of near 2.8. Additionally, VeroWhitePlus® is low enough loss a different characterization method should be utilized to get the most accurate reading of its loss tangent although the values reported in [88] and [95] agree with what was found here.

### 3.4.4 Results of anisotropy for VeroWhitePlus

Due to the nature of the 3D printing process used in this work, where a model is printed layer by layer, the question could easily be raised to whether the dielectrics printed can be considered

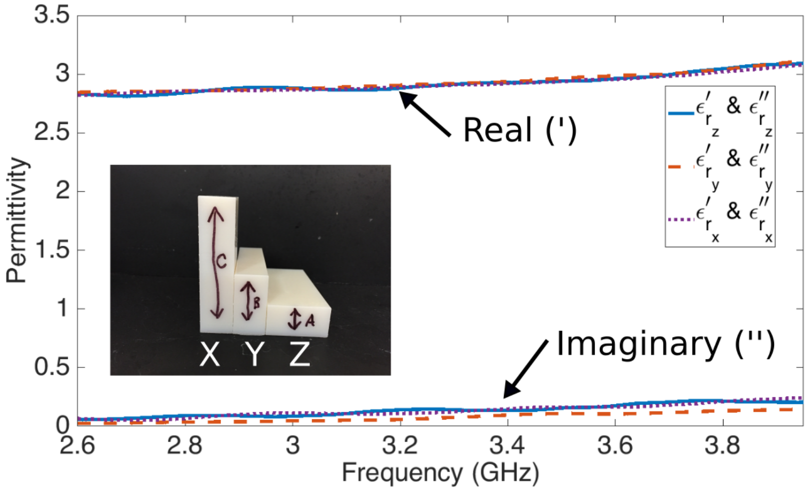

Figure 3.4: Measured complex permittivity of VeroWhitePlus® printed in different orientations, the inset is a photograph of the three measured samples with their printing orientations marked on the sides.

isotropic or anisotropic. Here, the term isotropic means that the material can be considered uniform in all orientations, specifically within the domain of electromagnetics that means a permittivity and permeability which are uniform in all directions (for example: free space). The implication being, that if 3D printed materials are characterized as in Section 3.4 are are not isotropic (ergo are anisotropic), then their results would only be relevant with respect to the orientation they were printed in.

To investigate whether this was the case with the printer and material used in this work three blocks of VeroWhitePlus® were printed along their X, Y, and Z orientations. These can be seen in the inset of Figure 3.4 where A = Z direction, B = Y direction, and C = X direction, as annotated, which can be imagined when visualizing how the blocks are inserted into the waveguide using the diagram in Figure C.1. Here, we are also defining the cross section of the waveguide used for measurements to be X on the width and Y on the height.

Figure 3.4 shows that the different printing orientations resulted in nearly identical results for the complex permittivity values. As an example, at 2.6 GHz the specific values of $\epsilon_{xx}$ = 2.82 + 0.07i, $\epsilon_{yy}$ = 2.84 +0.02i, and $\epsilon_{zz}$ = 2.83 + 0.06i which are indistinguishable from each other. It is possible that a more precise measurement technique could better distinguish between the orientations but given the methods used here it is likely that the 3D printed plastics printed using the printer in this work are isotropic. This means that despite the orientation samples are printed we can have confidence that their dielectric properties will be unchanged.

### 3.4.5 Results of other dielectric properties

Using the same methods as in Section 3.4.2 other 3D printed plastics that are available through the 3D printing resouces here at Michigan State were characterized. This work was performed to investigated whether there existed a better choice than VeroWhitePlus® to use for designs fabricated in this work. Overall, as can be seen in Table 3.2, the dielectric constant found is very similar to that of VeroWhitePlus® but many of the other choices have worse dielectric loss properties thereby leaving VeroWhitePlus® as the preferred choice.

The other materials investigated were acrylonitrile butadiene styrene (ABS) and Tango Black which can be printed using the Objet Connex350 printer, the "Resin Clear" available for printing with the Formlabs Form2 printer which, like VeroWhitePlus®, was also tested provided some additional curing time, and lastly polylactic acid (PLA) which can be printed on a Makerbot printer. The clear resin from the FormLabs printer is very comparable to VeroWhitePlus® but was not as easy to submit print jobs to and clean the parts afterwards. Additionally, although in Table 3.2 the Tango Black material appears to have a lower loss, this material is very flexibly, somewhat like the rubber on tires, and this result is likely inaccurate, but even if accurate, it would have not made a suitable choice for the applications used in this work due to its non-rigid nature.

## 3.5 Overview of additive manufacturing fabrication techniques

Here, a brief, general overview will be provided of the work done tangential to this thesis in the area of low-cost fabrication techniques using additive manufacturing. This work was informative in fabricating the prototype guides for this thesis but, more importantly, was used for other passive devices utilized in this work. Namely, the dielectric probes used to measure the waveguides, as well

| | | 2.8 GHz | | 3.2 GHz | | 3.6 GHz | |
|---|---|---|---|---|---|---|---|
| | | NRW | IEE | NRW | IEE | NRW | IEE |
| ABS | $\epsilon_r$ | 2.75 | 2.48 | 2.08 | 2.82 | 1.81 | 2.16 |
| | $\tan\delta$ | 0.28 | - | 0.27 | - | 0.25 | - |
| FormLabs Resin | $\epsilon_r$ | 2.85 | 2.93 | 2.89 | 2.82 | 2.96 | 2.80 |
| | $\tan\delta$ | 0.02 | - | 0.03 | - | 0.04 | - |
| FormLabs Resin Cured | $\epsilon_r$ | 2.85 | 2.96 | 2.88 | 2.85 | 2.95 | 2.82 |
| | $\tan\delta$ | 0.02 | - | 0.03 | - | 0.05 | - |
| PLA | $\epsilon_r$ | 2.71 | 2.13 | 1.96 | 2.02 | 1.90 | 1.93 |
| | $\tan\delta$ | 0.22 | - | 0.27 | - | 0.23 | - |
| Tango Black | $\epsilon_r$ | 2.96 | 3.09 | 2.96 | 3.02 | 2.97 | 3.03 |
| | $\tan\delta$ | 0.02 | - | 0.02 | - | 0.01 | - |

Table 3.2: Material characterization results for various 3D printed plastic samples.

as the lens used as a reference for the antenna, were made using methods explored in [66]. Looking to the future, many of the contributions made in the tangential work to this thesis will likely help shape the viability of 3D printings application to electronics. Given that it is suggested within this work that additive manufacturing techniques are the most promising path forward to realizing such designs in practice, the contributions made in advancing this area in general still hold a relevant place in this work.

### 3.5.1 Key contributions in the area of additive manufacturing techniques for RF and millimeter wave components

The key contributions offered in from work performed tangentially to the direct work in this thesis in the area of low-cost fabrication methods applied to RF and and millimeter wave circuits are namely:

1. 3D printing air-core substrates to tailor dielectric constant and loss for RF circuits [87],
2. first demonstration of a 3D printed cavity resonator with tunable resonant frequency [87],
3. applying 3D printing to injection molding [66],
4. and the first demonstration of 3D printed metal patterning on curved surfaces [96].

Some further depth will be given to the injection molding work in [66] so as to provide background on how the other passive devices utilized in this work were fabricated.

### 3.5.2 Millimeter wave and THz device fabrication background

Research in the terahertz (THz) spectral region (0.1 - 10 THz) has greatly expanded, especially in the development of THz systems. THz radiation holds significant potential in wide ranging applications such as medical imaging, spectroscopy, sensing, non-destructive evaluation, and communications [97, 8]. As the application of terahertz technology grows in use, there is a need to produce passive components that have low loss characteristics and are low cost. Many THz components are needed such as lenses for imaging and spectroscopy, microfluidic channels for drug discovery, and probes for on-wafer probing and sub-wavelength imaging.

The question of how to best manufacture THz passive components has been of interest [98, 99]. The tolerances of conventional machining techniques based on milling, cutting, and drilling are limited by the minimum size of the machining tool which are often too large for the geometries THz components demand. Fabrication techniques used for VLSI circuits and micro-electronics such as photo-lithography generally do not allow 3D structures with sizes as large as would be needed for these components either.

Significant work has been done to explore silicon based micro-machining of passive terahertz devices. Using localized pins and holes a snap together silicon rectangular waveguide has been introduced [100], as well as an air filled rectangular waveguide without additional assembly [101]. Other silicon waveguides have been fabricated using a variety of surface orientations, etching recipes, and geometries for use with millimeter and submillimeter wave frequencies [102, 103, 104].

However, larger passive devices such as lenses and probes cannot feasibly be fabricated using these techniques. Currently these, and other components, are fabricated through machining of dielectric blocks [105]. This approach is labor intensive, expensive, and limited in the types of structures that can be fabricated. Additionally, only a limited number of materials are available that can readily be machined. Even for smaller passive devices such as rectangular or cylindrical waveguides, the micromachining processes proposed with silicon are costly, complicated, and time consuming.

Hot embossing [106] and plastic injection micromolding [60, 107] for higher frequency components have been explored. Although these processes make manufacturing easy, able to produce on a large scale, and with good reproducibility, they are still relatively costly techniques as they rely on the use of machined metal molds which are expensive to make. Thus, there is a need for an alternative manufacturing approach that overcomes the limitations of cost and material availability while maintaining the ease of manufacturing, good reproducibility, and ability to produce on a large scale for THz passive components.

3D printing can be employed in the fabrication of THz dielectric components [108, 109]. However, the number of materials available for the design of THz components using 3D printing is limited. On the other hand, 3D printing overcomes the challenge faced in the machining of these components. To overcome the challenge of materials availability and cost, here it is proposed to use 3D printed templates in the fabrication of these components with a simple injection molding process. By using 3D printed templates, components can be rapidly prototyped with many dielectric materials that have low loss dielectric characteristics in the THz spectral region. As investigated in [30], many thermoplastics which would be compatible with an injection molding processing such as polypropylene, poly(norbornene) (commercially known as Zeonor), and high density polyethylene (HDPE) have low loss in the THz region. Furthermore, molding can be carried out at the wafer level to achieve large area processing and maintain the other benefits demonstrated with hot embossing and plastic injection micromolding.

### 3.5.3 Probe and lens design

Here, the design, fabrication, and measurement of a probe and lens from [66] are shown as well as details of template and mold fabrication. Models were made using ANSYS HFSS®. In Figure 3.5 diagrams of the components are shown and in Table 3.5.3 their dimensions are proved.

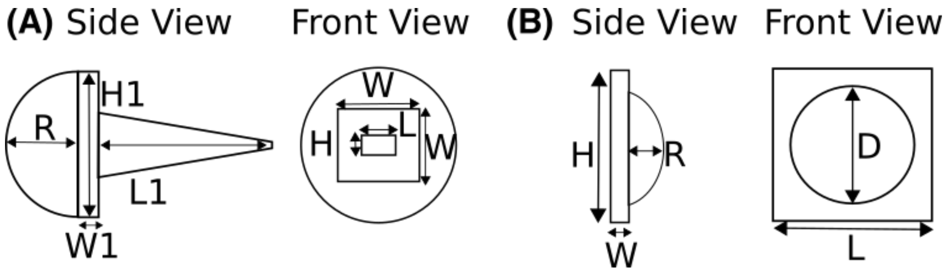

Figure 3.5: Diagrams of the devices to be molded including (A) a square tipped probe and (B) a lens.

| (A) Probe | | (B) Lens | |
|---|---|---|---|
| R | 13 mm | H | 41 mm |
| W1 | 3.5 mm | W | 3.5 mm |
| H1 | 26 mm | R | 6.5 mm |
| L1 | 30 mm | D | 33 mm |
| W | 13 mm | L | 41 mm |
| H | 0.4 mm, 3 mm | | |
| L | 2 mm, 6.5 mm | | |

Table 3.3: Summary of device dimensions.

### 3.5.4 Mold design and fabrication

The molds are designed in ANSYS HFSS® by taking the design for the desired component and "subtracting" it from a dielectric block. The block is then split into two pieces with corresponding pins and holes for the joining and alignment of the two sides after printing. Each mold has an input location for the nozzle of the injection molding machine and an output hole for air or extra material to escape as the cavity is being filled. An image of one of the fabricated molds can be seen in Figure 3.6 (B) and (C). Molds for components that required more material, such as the probe or lens, additionally had holes through them for mounting screws, as can be seen in Figure 3.6. This ensures that the mold halves are held together through the duration of the cooling period and not possibly pushed open by any excess material.

The obvious issue with using a 3D printed mold as opposed to a machined metal mold is the material differences. Metals, such as aluminum, have a high thermal conductivity and are able to quickly draw heat away from the injection chamber while maintaining their integrity. Dielectric

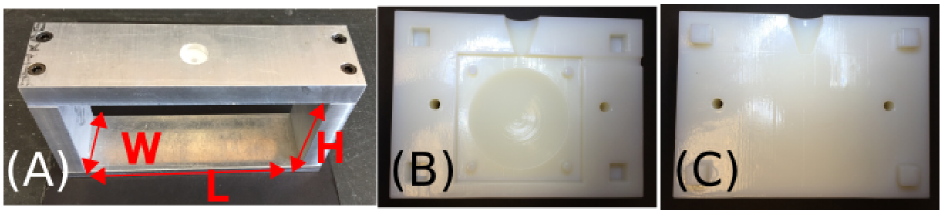

Figure 3.6: Fabricated (A) aluminum holding frame for molds and (B) an example mold device side and (C) back side.

materials, such as those used in commercially available 3D printers, are insulators and thus have a relatively low thermal conductivity. This not only means the newly formed component in the injection chamber will take a longer time to cool, but that the heat, unable to dissipate quickly, could compromise the mold integrity by melting, warping, or otherwise deforming the intended shape.

In order to alleviate this possibility in the process, an aluminum frame was designed and fabricated, as can be seen in Figure 3.6 (A), to hold the 3D printed molds. This frame not only acts as a heat sink but also provides greater structural integrity. The injection nozzle of the molding machine is a very localized source of high heat and is pushed into the mold using compressed air. This frame allows the hot nozzle to rest on top of the mold for the duration of the injection without causing the mold any stress due to heat or pressure from the nozzle. The cavity of the aluminum frame is large enough to accommodate all the molds used for this work. The dimensions marked in Figure 3.6 (A) are all on the inside of the frame, with a length (L) of 80 mm, width (W) of 38 mm, and a height (H) of 58 mm. The white spot on the top of the frame has a diameter of 11 mm, with the inner hole having a diameter of 3.6 mm, and is the injection site for the molding machine. The white material is teflon, which is used so that material passing through the frame does not cool down too quickly. The superior thermal conductivity of the aluminum can affect the ability to completely fill the mold cavity for larger components if it cools too quickly.

Both VeroWhitePlus®, and polylactic acid (PLA) materials were considered for use in printing the molds. PLA was found to be less tolerant of the high heat in the molding process than the VeroWhitePlus®, thus VeroWhitePlus® was used.

### 3.5.5 Injection molding process, measurements, and results

The mold geometries were exported and printed on a commercial Objet Connex350 Multi Material 3D printing system using VeroWhitePlus®. The mold is then placed in the aluminum frame, and into the injection molding machine from Adler Machine Tech Corp. LDPE or HDPE pellets are melted in the machines heated chamber at around $390 - 420^o\ F$ and injected into the mold. After cooling for five to ten minutes inside the mold the component is removed and ready to use. The surface of the molds are smooth enough, due to the fine printing resolution of the Connex printer, that there is no issue with the injected material adhering to the surface upon release.

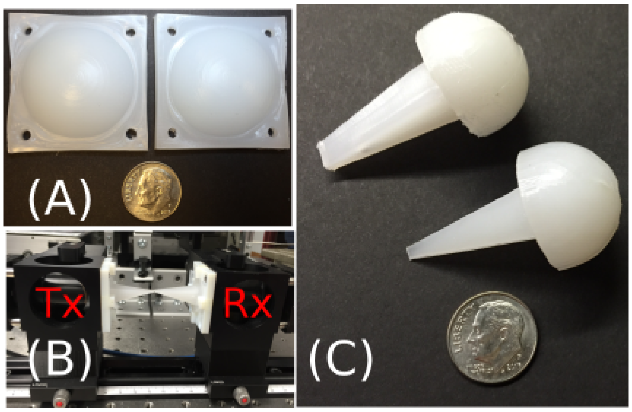

Figure 3.7: Fabricated units as compared to a standard dime (diameter of 17.91 mm): (A) set of lenses, (B) square tipped probes in place to be measured, and (C) square tipped probes.

The resulting components from the proposed injection molding process can be seen in Figure 3.7 (A) and (C), overall, the variation in component dimensions was minimal and on the order of the resolution of the printer which would be expected. The fabricated components were measured and evaluated using an Emcore frequency domain terahertz system. In Figure 3.7 (B) the measurement setup is shown for all probes measured, which yields information about the maximum amount of power that can be transferred tip to tip.

The results of these measurements can be seen in Figure 3.8. The two different sets of fabricated probes, with a thin and thick rectangular tip, where compared to probes fabricated by hand machining HDPE and ones 3D printed using VeroWhitePlus® material which has a dielectric

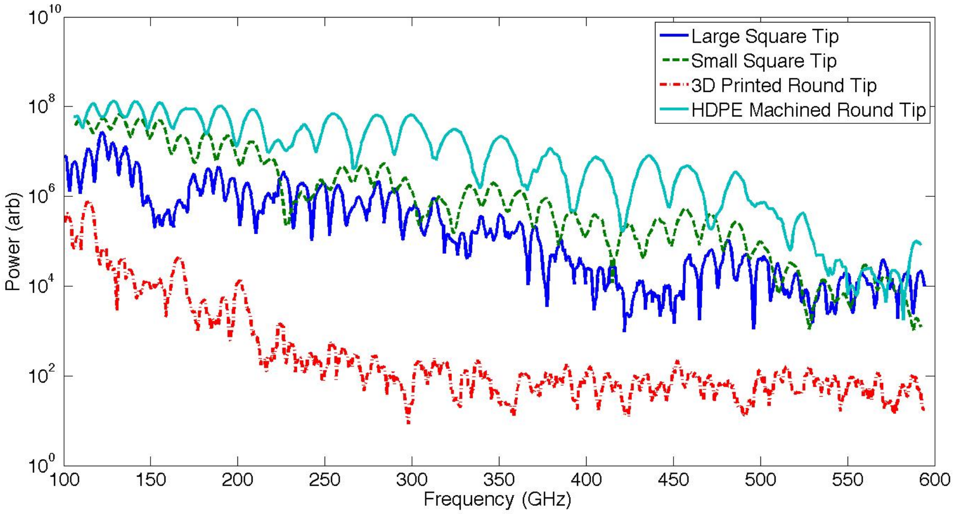

Figure 3.8: Measured results for different probes.

constant of 2.8 and a loss tangent of 0.04 [108]. The probes fabricated here were made using LDPE. The fabricated probes had comparable performance to the HDPE probes, especially at higher frequencies. The additional loss between the square and round tipped geometries is mostly due to polarization losses. The Emcore system uses a circularly polarized wave which can be much more easily coupled into the round probes than into the square ones. The 3D printed probe, although having the same advantage of the HDPE one as far as polarization, performed appreciably worse than the molded probes due to the loss tangent of the material being an order of magnitude greater than either the HDPE or the LDPE. These results show that the ease of 3D printing could be better suited to the manufacturing process of larger components than to the direct fabricated of them.

The lenses were measured by mounting them on the transmitter and receiver heads of the THz system and using the Dwell setting instead of a frequency scan. The Dwell setting continuously transmits a single frequency so the signal strength can be monitored. The maximum signal strength was seen when the two lens were about 635 mm apart making their estimated focal length about 317 mm. A slit was used to measure the beam width of the lenses. The slit was placed at the focal distance of the lenses and slowly opened until no further signal strength was gained. Using this method the diameter of the beam width was found to be 6.32 mm.

## 3.6 Conclusion

Notable contributions have been made in the work performed in tangent to this thesis with regards to low-cost additive manufacturing techniques to realize RF and millimeter wave circuits and components. Overall this work allowed reasonable prototypes to the proposed waveguides to be realized using additive manufacturing for part of the structure. However, in the future as 3D printing becomes a more mature technology for fabricating electronics, the proposed structures could not only be fully additively manufactured but created fully at much smaller scales to be directly printed on-board or on-wafer.

Additionally, a new process to fabricate THz components using 3D printed templates coupled with injection molding was introduced. This process allows for designs to be rapidly prototyped, have good reproducibility, and allow a variety of low loss dielectric materials to be available for THz components. This process is especially useful for having flexibility in the manufacturing of larger passive components like lenses and probes.

# CHAPTER 4

# CIRCUITS

## 4.1 Overview

Here, the general waveguide design as introduced in Section 2.2 will be extended to other circuit designs. First a power splitter (or power combiner) is designed, simulated, fabricated using 3D printing, and measured. Then, three different approaches are taken to design filters which could be integrated into the base waveguide designs when being used in a larger system to be more compact. A band-stop filter is shown using a photonic-crystal inspired design, then, another band-stop filter is shown by designing an open circuited stub mimicking transmission line circuit design principles, lastly, a stepped impedance filter is used to show a band-pass filter. The filters are shown purely through simulation as their dimensions are too fine to be realized using the fabrication techniques employed in this work. Finally, an antenna based on dielectric rod antennas, or a wire-less interconnect, is presented as well as a measurement and calibration technique to suite the measurement needs.

## 4.2 Power splitter/combiner

Using the proposed waveguiding geometry other basic transmission line circuits can be designed and fabricated. As an example, a power splitter/combiner is designed, fabricated, and measured. The design is made and simulated in HFSS®. The model itself is electrically large, with a size approximately $21 \times 21$ mm and simulated at 100 GHz. The model, simulation results, fabricated prototype, and measured results can be seen in Figure 4.1. In Figure 4.1 (A) the "Ideal" traces are from a model which exactly mimics the proposed waveguide in having an alumina core which perfectly meets a VeroWhitePlus® cladding, enclosed in a thin (1 μm) copper outside layer. The S-parameters have a reflection coefficient below -20 dB and transmission coefficients slightly above -10 dB. The slightly above -10 dB value is as expected given that, from previous simulations,

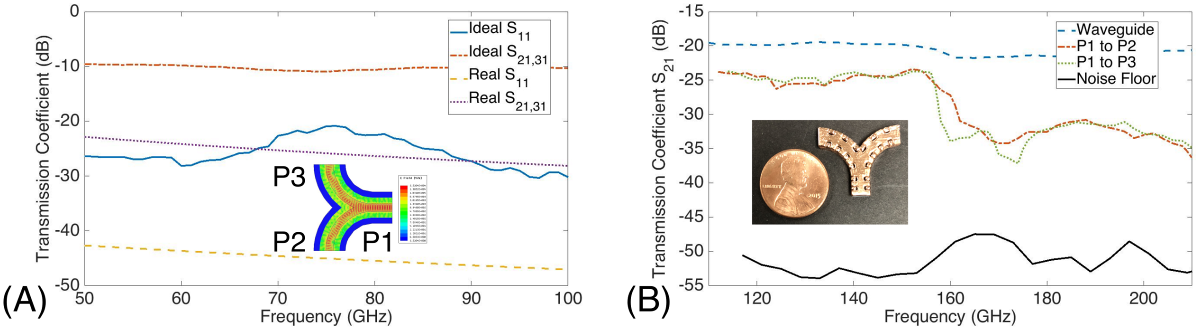

Figure 4.1: Power splitter (A) simulated S-parameters with an inset of the simulation model with the electric field plotted and (B) measured transmission coefficient with an inset of the fabricated device.

the waveguide of rectangular cross section had around 1-1.5 dB of loss per 3 mm if one side of the splitters channel is about 20 mm of distance traveled that would add up to about -10 dB. Although the frequency range of simulation and measurement results in Figure 4.1 are different due to computational cost of the simulation model, the results still confirm that the design works and allows comparison with the measured around the 100 GHz frequency range.

A power splitter/combiner presents more fabrication challenges than the initial prototypes of the waveguides because it involves curves. Before, the alumina core was inserted after 3D printing of the cladding but here, the core cannot be simply pushed into the cladding. For this design, the waveguide was printed in two pieces, a bottom with sidewalls and a top, and the two pieces were patterned to have a semi-dovetail junction to fit together. The pieces were printed so the junction was slightly snug so no epoxies were needed to keep the two pieces joined together. A laser cut piece of Roger's Board with a dielectric constant of 10 was used as the core to mimic alumina although overall much more loss will be expected. After sandwiching the Roger's Board core into the two cladding halves the structure was metallized using the same sputtering procedure as in Section 3.3.

The final fabricated device is shown in the inset of Figure 4.1 (B) which shows the measured results using the same equipment and general setup as in Section 2.2.2. An additional straight waveguide was fabricated alongside with the power splitter/combiner using the Roger's board core and printed in two pieces and is about the same length, to act as a suitable comparison. As can be seen in the measured results, each side of the power splitter measured about the same which is somewhat less than half the total transmission seen from the comparison waveguide. Overall the power levels are much less in these devices due to the much more lossy Roger's board used as the core, where most of the power is confined. For context, an HFSS® simulation was done of the device as it was fabricated, with the Roger's core, the cladding in two pieces, and some imperfections at the joints of the two pieces but leaving some air in between. The results of this simulation can be seen in Figure 4.1 (A) labeled as "Real" which, although obviously show a great decrease in performance, do match the measured results of what was fabricated. Another effect seen in the measurements due to the use of Roger's board as the core is the reduction in the transmission coefficient near 150 to 160 GHz. This same effect was seen in [30] when characterizing the same material, RO3010 being the Roger's board with a dielectric constant of 10. This effect is due to scattering from the particle sizes of the ceramic used in the board.

## 4.3 Filters

A filter is a two-port circuit which is designed in such a way to impose selectivity on the frequencies which pass between its ports. Most commonly, filters are designed to achieve frequency responses that result in low-pass, high-pass, band-pass, or band-stop characteristics. Filters can be implemented with hardware or digitally, can be passive or active, but, here the goal is to integrate a filter into the proposed waveguiding design. Such a filter would be passive, and therefore require no additional circuitry or power to function. It would also simplify larger integrated system designs by allowing filtering steps to be directly integrated into the interconnects between other subsystems.

Here three possible integrated filter designs are shown, two in simulation and one which is taken through the fabrication stage, to demonstrate the feasibility of integrating filters into the waveguide design.

### 4.3.1 Photonic crystal inspired filter

A photonic crystal (PC) is a structure that is periodic on a nanoscale (optical regime) whose periodicity affects the motion of photons. Early work from the 19th century in the field of physics showed that multi-layer dielectric stacks with periodicity results in a photonic band-gap in the dimension of that periodicity thus providing a filtering effect. Similarly as with optics, electromagnetic waves can be affected using the same principle. As can be seen in Figure 4.2, if an electromagnetic wave impinges upon a stacked dielectric structure with periodicity in that dimension then a band-stop filtering effect will be observed around the wavelength corresponding with the thickness of the dielectric layers which should be a half wavelength at the target frequency of rejection [110]. Prior work has shown that using the stacked dielectric approach to creating a PC-inspired filter can work in the THz range, even using fairly lossy materials in the case of directly 3D printing the dielectric layers [111, 66]. PC-inspired filter structures have been explored in the THz range for microfluidic detecting as well by allowing the small liquid sampled to introduced as a “defect” into the PC structure [112].

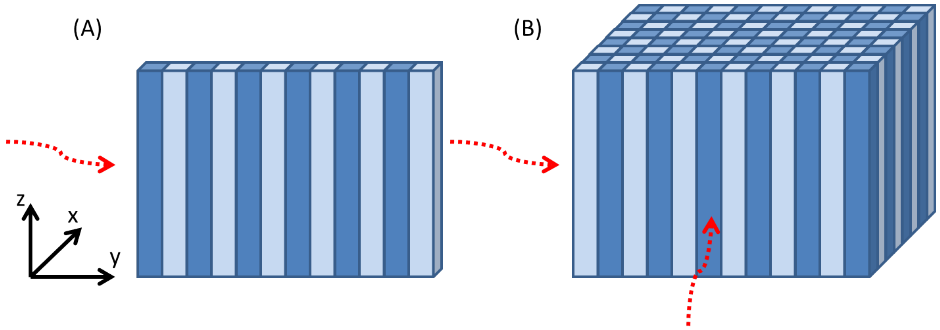

Figure 4.2: An illustration of how an electromagnetic wave interacts with a PC-like structure.

This approach could be used to integrate a band-stop filter into the proposed waveguiding structure as can be seen in Figure 4.3. Here, a thin silicon strip was used as the core material in simulation which has a dielectric constant of 11.9 and a loss tangent of 0.004. The strips dimensions itself were a height of 140 µm and a width of 2 mm. As previously explored in Section 2.3, by making the core sufficiently thin with respect to a wavelength then the electric field is primarily confined to the core-cladding boundary. Thus, by creating dielectric layers of air and the material VeroWhitePlus® along the length of the silicon core the traveling wave will experience the PC-like effect creating a band-stop region. To further show that this effect is not just from the layered dielectrics but a direct results of the layered dielectrics in conjunction with the guiding of the wave on the core a simulation was also run where the silicon core had been removed and air was left in its place.

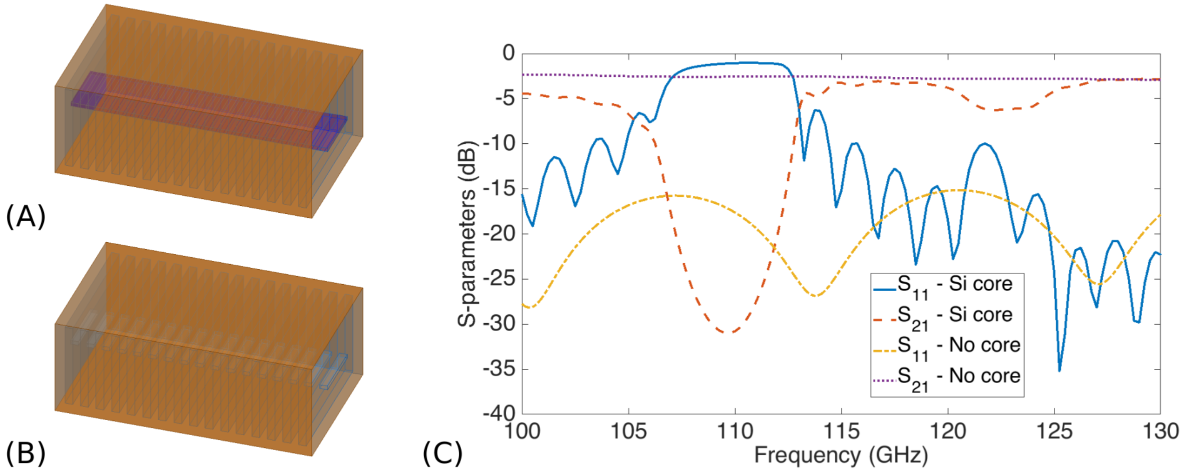

Figure 4.3: The (A) PC-like filter, (B) the simulated structure without the guiding core and (C) the simulated S-parameter results.

The simulation results in Figure 4.3 show a clear band-stop region with a center frequency around 110 GHz and a bandwidth of 10 GHz. Importantly, the results where the silicon core was excluded do not show any filtering effect thus proving the necessity of the guiding core strip to make this passive filter integration realizable.

### 4.3.2 Open circuited stub filter

A well known, simple filtering structure that can be easily integrated with a transmission line is a stub filer. The stub can either be short circuited or open circuited which result in a band-pass or band-stop filter respectively. The filter will have a center frequency that corresponds to the stub length where the stub length ($L_s$) is $\lambda_g/4$ and the center frequency ($f_c$) is $c/\lambda_g$ where $c$ is the speed of light in a vacuum and $\lambda_g$ is the wavelength of the center frequency as found when accounting for the material of the medium of propagation, typically not free-space. A traditional microstrip based transmission line open circuited stub filter is shown in Figure 4.4 (A) for reference.

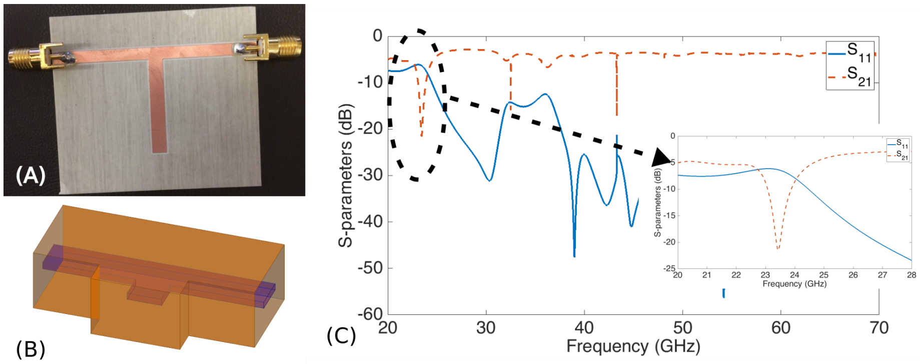

Figure 4.4: An (A) example of a microstrip based stub filter as compared to the (B) waveguide based stub filter and its (C) simulated S-parameter results with an inset showing a closer view of the filtering region.

Figure 4.4 also shows the simulated model of a SIRW open circuited stub filter where the core-cladding are extended into a stub for a fourth of the guided wavelength. Here, alumina is used in the core and VeroWhitePlus® as the cladding material. The stub length is 1.5 mm which, in the guided medium where the effective real part of the dielectric constant is 5 at 30 GHz, according to the simulation findings would lead one to predict a filtering effect at 22.36 GHz using the formula in Equation 4.1. In Figure 4.4 (C) the band-stop frequency is centered at 23.44 GHz which agrees well with the expected value.

$$f_r = \frac{c}{\sqrt{\epsilon_{eff}} \times L \times 4} \tag{4.1}$$

Although these findings are fairly low in frequency for this work they support an important property of the proposed waveguides in their ability to service a wide bandwidth. This filter design shows that these waveguides can be used for circuits at the lower end of their frequency range. In some of the designs presented earlier cut off frequencies of around 20 to 30 GHz were shown but here the cladding layer dimension was expanded to lower the cut off frequency.

### 4.3.3 Stepped impedance band-pass filter

A more nuanced approach to designing filters which is based off of microstrip circuit design as opposed to optical circuit designs is to vary the effective impedance of the guide the signal is traveling through. At low frequencies when lumped elements such as capacitors and inductors can be used filters can readily be realized by combining the two elements in such a way that only certain frequencies can pass through a network. Lumped elements behavior can be replicated at higher frequencies by using distributed elements, such as microstrip open-circuited or short-circuited stubs [113].

Impedances within a waveguide can be affected by changing the waveguide cross-section, whether in dimension, or by changing the medium filling the guides cross-sectional area. To apply the idea of varying guide impedance to the proposed waveguiding structures in this work the medium will not be changed in the cross-section, although, if 3D printing gradient dielectrics were possible as discussed in Section 2.2.1 this would be an interesting application, but the cross-sectional area of the cladding layer will instead be changed thereby changing the boundary imposed by the metalized outer layer.

Following design procedures as laid out in [113], the length of the waveguide sections is kept at $\lambda_g/4$ where $\lambda_g$ is the wavelength of the target operating frequency in the guided medium. Using tables from [113] different stepped filters can be designed. As a demonstration here an N = 6 and N = 5 filter were implemented using the ratios from [113] but are included in Table 4.3.3. For the designs presented here, a thin cladding layer of 200μm was used and considered as the normalized base impedance of “1”. The rest of the cladding layer sections were shrunk or expanded by the $\mathrm{g_n}$ factor.

The cladding layer of 200μm was originally selected with fabrication needs in mind to realize the designs with that thickness being the thinnest that could be 3D printed and survive the copper sputtering process. A thinner layer was found to work better through simulation but would not have been realizable.

The simulated models can be seen in Figure 4.5 along with the attempted process for fabrication.

| N = 0 - 6 | $g_n$ | N = 0 - 5 | $g_n$ |
|---|---|---|---|
| 0 | = 1.000 | 0 | = 1.000 |
| 1 | = 0.618 | 1 | = 0.7654 |
| 2 | = 1.618 | 2 | = 1.8478 |
| 3 | = 2.000 | 3 | = 1.8478 |
| 4 | = 1.618 | 4 | = 0.7654 |
| 5 | = 0.618 | 5 | = 1.000 |
| 6 | = 1.000 | | |

Table 4.1: Summary of stepped impedance filter ratios.

Given the extremely small nature of the dimensions to accommodate THz frequencies directly printing the cladding layer and using the fabrication process outlined in Section 3.3 was not feasible. Therefore, the fabrication methodology proposed in [114] was attemped wherein designs negatives were printed and metalized to create an “air substrate”. For these designs it means the cladding layer is air and, in order to maximize the electric fields interaction with the changing metal cross-sections a thin silicon (Si) core of 140μm is used so the electric field is primarily confined to the core-cladding boundary as opposed to being almost entirely within the core as in the base waveguide design.

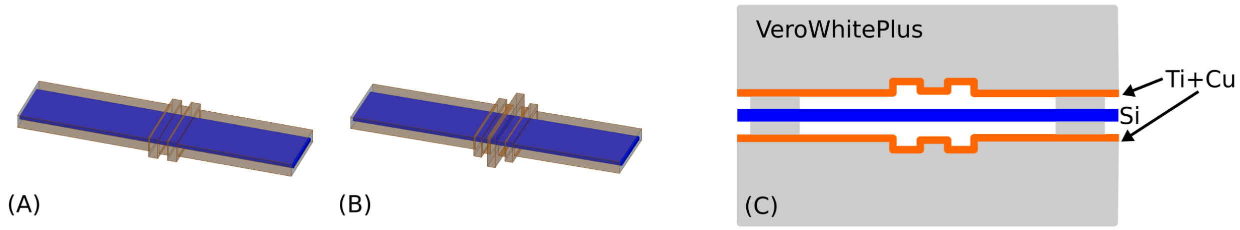

Figure 4.5: The simulated models for an (A) N = 5 and (B) N = 6 stepped impedance filter along with the (C) process with which fabricated was attempted.

The fabrication method shown in Figure 4.5 (C) shows that the waveguide filter was 3D printed in two halves which were metalized and subsequently pressed together with the Si core in place with small, unmetalized, 3D printed spacer pieces that ensure the core is centered in the middle channel. However, several attempts were made to fabricate these designs and it was found that 200μm was still too thin to be fabricated and thicker layers would have resulted in too poor of performance based on simulation results. Therefor, only simulation results are shown for the stepped impedance filter although, with improvements in 3D printing resolutions, such a filter could be realized. Figure 4.6 shows the simulated S-parameters of the filters where a band-pass region can be seen around 60 GHz as expected.

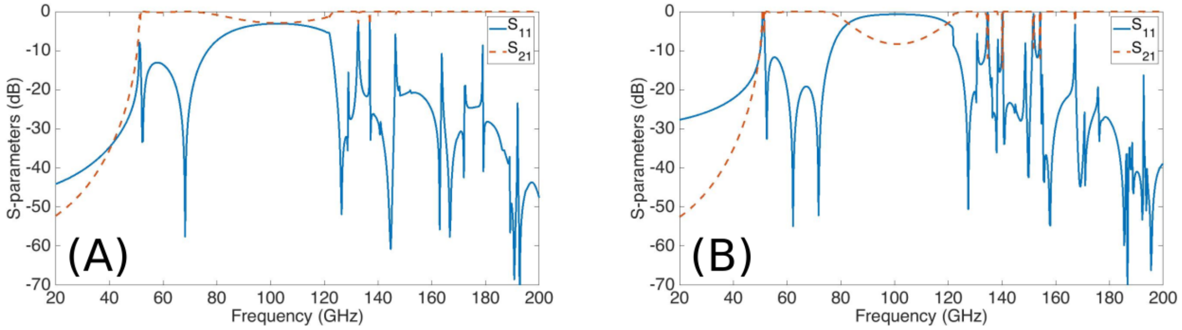

Figure 4.6: The simulated S-parameters for the stepped impedance filters where (A) is for N = 5 and (B) for N = 6.

In addition to improving the resolution of the filter, the core material would also need to be improved. The silicon core strips to be used in fabrication were first measured alone using the Emcore THz system and HDPE probes in an identical setup to the waveguides in Section 2.2.2. Two different high resistivity silicon wafers pre-cut into strips were available, a 25 mm long strip, 2 mm wide, with a 140µm thickness was measured from each wafer, denoted 1 and 2, while the lights in the laboratory were on and off. The lighting can create false results by encouraging electron-hole pairs.

As shown in Figure 4.7 one of the wafers, the second, was notably affected by the light in the room. However, regardless of the light, neither provided a consistent enough transmission for a filtering effect to be able to be seen.

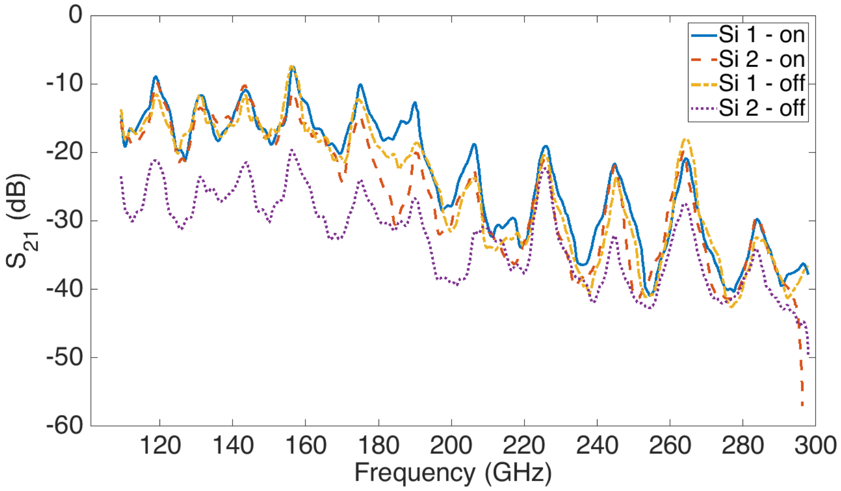

Figure 4.7: The measured transmission of 25 mm high resistivity silicon (Si) strips from two different wafers, denoted 1 and 2, with the lights in the measurement space left on or turned off.

## 4.4 Antenna

### 4.4.1 Dielectric rod antenna introduction and background

With the increase in use and demand for millimeter wave circuits and systems, in addition to a waveguide, one of the other most basic building blocks that is necessary is an antenna. Dielectric traveling wave antennas, typically seen in literature as dielectric rod antennas (DRA), have been investigated due to their small size, high gain, and wideband performance characteristics. Additionally, depending on the materials used, DRAs can be very low-loss. DRAs can be as simple as a rod, typically of circular or rectangular cross-section with dimensions related to the target operating frequency range, or include a cladding layer with various tapering steps to improve matching between the source/detector and/or free-space.

Many have proposed the use of DRAs as a means of wireless chip-to-chip communication as a possible alternative to wired interconnects in order to overcome the pressing need for wide bandwidth communications [115]. Substrate integrated circuits using dielectrics such as the proposed waveguide in this work and DRAs still allow easy integration into planar systems without suffering the conductor losses of microstrip based designs at millimeter frequencies. Some work has shown how substrate integrated waveguides (SIW) could transition into dielectric antennas [116] but the SIW that would lead to such an antenna would suffer those conductivity losses and limit its bandwidth. Dielectric resonator antennas, also commonly abbreviated as "DRA", have been proposed as another suitable high frequency, easily integrable alternative in work such as [117, 118, 119, 120]. Dielectric resonator antennas demonstrate good gain and are substrate compatible but do not offer the wide bandwidth that dielectric rod antennas can which will be important in meeting future bandwidth needs when addressing the specific problem of chip-to-chip communication.

Many excellent examples of DRAs [121, 122, 123] and DRA arrays [124, 125] can be found for operation in the millimeter wave band. In [126] a dual-polarized DRA is shown which shows double the wireless capacity of a conventional single polarized rod antenna operating at 75 GHz using the $E_x^{11}$ and $E_y^{11}$ modes. A wideband DRA is also shown in [127] for use between 75-325 GHz using high-resistivity gallium-arsenide (GaAs) as the core material. Here the antenna is shown to transition into a variety of metal rectangular waveguides well without the use of transitions (it is directly inserted into the guides). Although somewhat lower in frequency, [123] introduces a multilayer DRA which is created using fused deposition modeling of two thermoplastics and is demonstrated to operate between 30-40 GHz with a peak gain of 22 dBi. This work is particularly notable given that vast majority of the DRA literature uses either GaAs or Sapphire as the low-loss core material to achieve their antenna designs which are both expensive and have some fabrication limitations.

Moving into higher frequencies that enter the THz range, [128] used a genetic algorithm (GA) to optimize a rod shape which, coupled with a ring slot antenna as an excitation, could be applied to imaging applications. Although, notably, in this work the authors never provide their target frequency range or at what frequency their radiation patterns were acquired leaving doubt as to whether it was actually suitable for the THz range. A similar ring slot excitation is used for realizing a THz dielectric tapered rod antenna in [129] which presents theoretical and measured results at 600 GHz for use in an imaging system. A metal-dielectric antenna for terahertz near-field imaging was introduced in [130] where a slab of low-loss dielectric material was sharped into a pyramidal tip and subsequently partially metalized. This approach allowed the authors to improve upon work that used thin metal tips for submillimeter wavelength imaging but would not be applicable to a communications application.

As noted in [131, 132], specifically with regards to high-speed wireless communication applications, a dielectric rod waveguide combined with a metal waveguide is a promising candidate for solving this problem. The design proposed here is just that combination of a SIRW which can easily be adapted for the purposes of achieving a wireless link which is low-cost, easy to integrate, and, most importantly, provide a *wide bandwidth*.

### 4.4.2 Antenna design

Although DRAs have many benefits they can prove to be a challenge to feed [133]. Here, because of the nature of the measurement system used, more details on the measurement system itself can be found in Section 1.1.3, the DRA design is feed by a converging lens focusing the THz radiation into the DRA, specifically, coupling into the core layer. The coupling lens structure is designed the same as in Section 5.2.2.1 so that the core layer is directly in the path of the lens focal point.

The DRA itself is comprised of an alumina core layer and a high density polyethelene (HDPE) cladding with a thin layer of copper around as its outer most layer. The diameter $d$ of the antenna was approximated according to the design expression for circular dielectric rods which states that the ratio of $d$ to the free-space wavelength should be less than $0.626\sqrt{\epsilon_r}$ to guarantee the fundamental $\mathrm{HE}_{11}$ mode [134]. Since an alumina rod was used with a $d$ of 1.588 mm and dielectric constant ($\epsilon_r$) of 9.2 and the lowest operating frequency to be at least 100 GHz the ratio $d/\lambda_o$ is 0.53 which is less than $0.626\sqrt{\epsilon_r} = 1.89$.

In Figure 4.8 (A) on the right the actual “antenna” model to be fabricated is shown as opposed to how such an antenna would actually be implemented as shown on the left. In (B) the electric field along the tapered cone section is shown, and is consistent with expectations from Section 2.2.1.2 that at lower frequencies the field will interact more with the metal coating than at higher frequencies. Simulation results are shown in Figure 4.8 (C) and (D) and were performed on the model in (A)

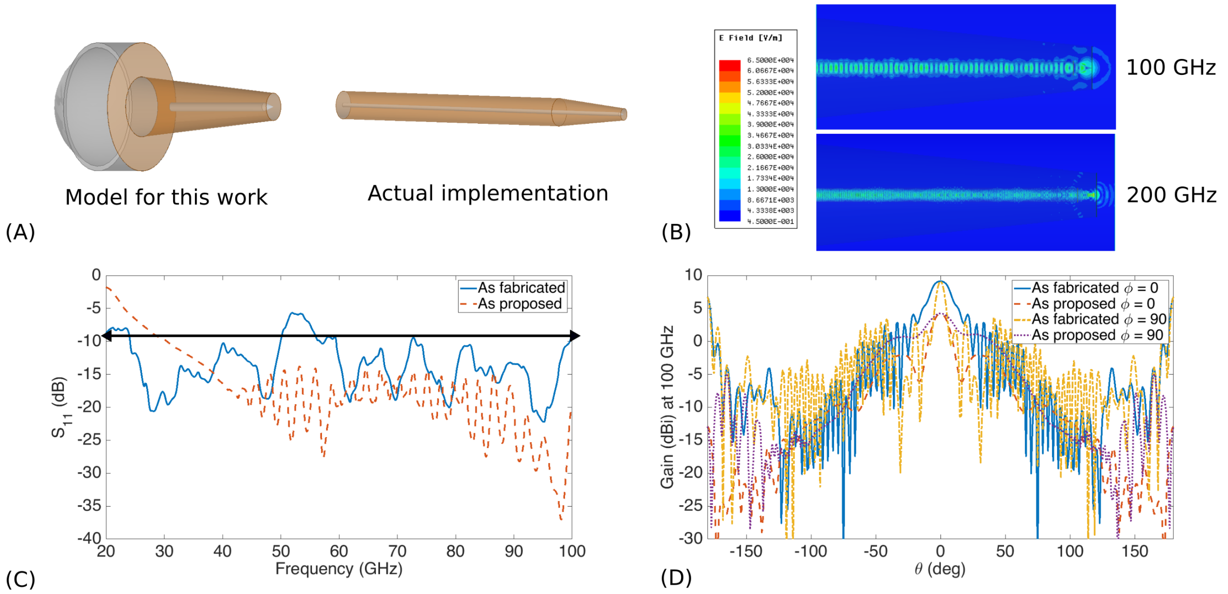

Figure 4.8: The antenna model simulated and fabricated for this work along with its actual envisioned implementation. Shown in (A) are the reflection coefficients simulated for both models and as well their (B) radiation patterns simulated at 100 GHz.

so as to allow direct comparison to the measurements of the fabricated prototype later as well as (B) to show what the "ideal" response would be. The reflection coefficient in (C) shows very wide bandwidth, having a response below -10 dB almost entirely from 20 to 100 GHz for the fabricated model and entirely for the proposed model. Due to the large electrical size of the model, simulations were limited to 100 GHz. As elsewhere in this work, simulations were carried out in ANSYS HFSS®. The two-dimensional radiation patterns are shown in (D) where the fabricated model shows markedly better directivity. In reality, a high directivity would be most desirably for use as a wireless interconnect and more work would be needed to improve this aspect of the real design.

### 4.4.3 Proposed antenna calibration and measurement

A proposed measurement setup and method using the Emcore Frequency Domain THz system is shown in Figure 4.9 where the transmitting (Tx) and receiving (Rx) heads are on rails which allows a two-dimensional radiation pattern to be found. A DUT can be mounted directly on the Tx head while an optical slit can be directly mounted on the Rx head which will dictate the aperture size of the measurement. Also shown in Figure 4.9 (A) - (D) are two antennas before their metallization. The fabricated prototypes were made by CNC for the low dielectric constant cladding (HDPE) and an alumina rod was shaped and inserted by hand. The top images show one which matches directly with the simulated model and the bottom images show one where the core layer protrudes from the cladding by a few millimeters which is more typical for DRAs.

The antenna measurement must be made relative to some isotropic radiator. Using this THz system, and at this frequency range, there is no recognized calibration standard, thus, a reasonable calibration choice must be made. In prior work [135], a small aperture has been chosen to calibrate the antenna realized as a 1.5 mm circular hole in a thick plate of copper (Cu) which was a similar diameter to the aperture used in the antenna under test (AUT). However, aperture antennas do not result in an isotropic radiation pattern as would be ideal for a calibration antenna. Additionally, for the specific measurement system used here, the quasi-optical nature also forces one to consider how well a solution such as an aperture antenna would be excited. Here, the use of a divergent lens is proposed and used as a calibration standard, as shown in Figure 4.10, where the previously discussed plano-convex lens from Section 3.5 is used when mounted in the opposite orientation to have a divergent rather than convergent effect on the collimated THz beam.

The lens to be used as the calibration "antenna" was modeled and simulated in ANSYS HFSS® to understand what to expect by treating it as an antenna. Although, as seen in Figure 4.11, a radiation pattern for the lens can readily be found in simulation more practical information can be found using the ANSYS HFSS built in Fields Calculator tool. Using this tool the power flow through an open (or closed) surface can be found by integrating the Poynting vector normal to that surface. In the lens model a cylinder of air extended away from the lens surface for many wavelengths of the solution frequency, 100 GHz, and circular surfaces were placed along three locations: (1) directly entering the lens, (2) directly exiting the lens, and (3) about 2.5 $\lambda$ (7.5 mm) away from the lens. Entering the lens is 100 % of the power, exiting is 90 %, and at a distance is 87 %. Later, if measured, these power percentage estimates can be useful, given that the THz

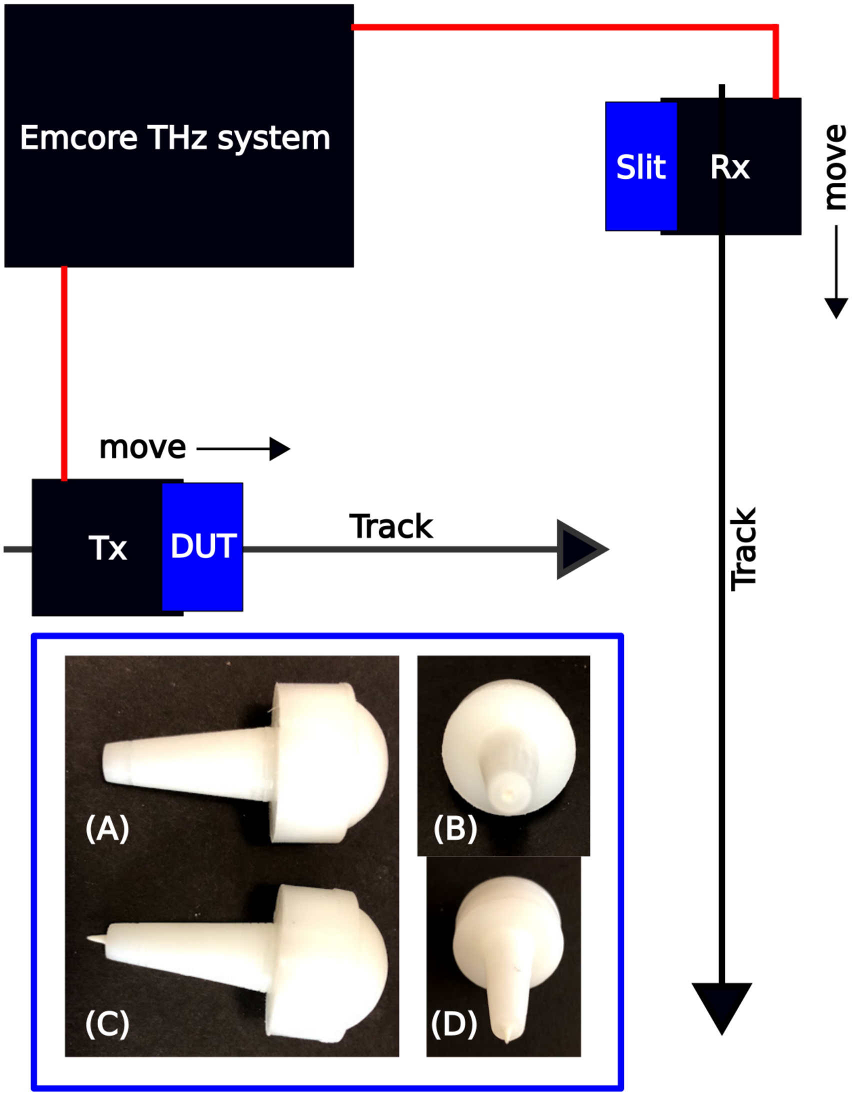

Figure 4.9: The measurement setup for the calibration reference and antenna. The inset shows the (A) side view and (B) head on view of an antenna matching simulation where the core is completely within the cladding and the (C) side view and (D) head on view of an antenna where the core protrudes beyond the cladding.

measurement system used works in units of power, to understand the results.

## 4.5 Conclusion

The proposed waveguiding design can be extended to realize other circuits including a power splitter, filters, and an antenna. By sharing a common design technique these circuits similarly can

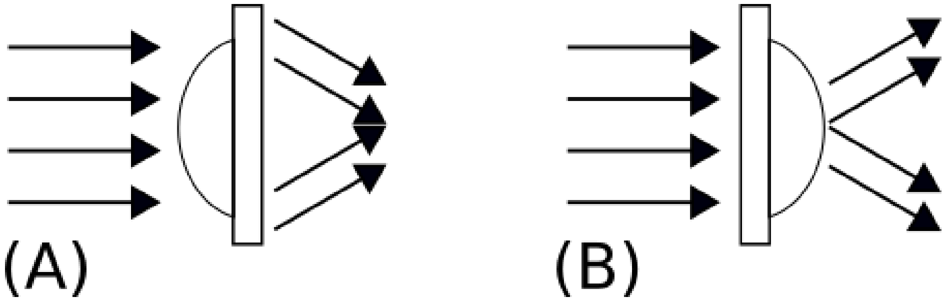

Figure 4.10: Illustration of using a plano-convex lens as a divergent lens to act as a calibration for the antenna.

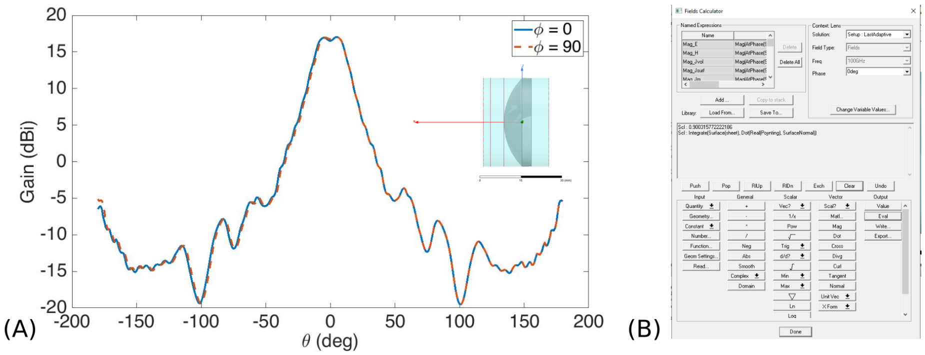

Context: Lens
Solution: Setup : LastAdaptive
Field Type: Fields
Freq 100GHz
Phase 0deg

Scl : 0.900315772222186
Scl : Integrate(Surface(sheet), Dot(Real(Poynting), SurfaceNormal))

Figure 4.11: (A) Radiation plot of a plano-convex lens with the model used inset as well as (B) a screen capture of the HFSS Fields Calculator tool used to get power estimates.

be realized for low-loss, wide-band, substrate integrated applications. Here, as expected, the power splitter showed in simulation and measurement an equal power division. Additionally, three filters were explored through simulation showing band-pass and band-stop characteristics and each using different design techniques to be realized. Lastly, the design was extended to realize a wire-less interconnect by transition to a dielectric rod antenna-like design.

# CHAPTER 5

# SENSORS

## 5.1 Overview

Applications related to sensing are presented in this Chapter. First, probe designs based on the proposed waveguiding structuring are presented as well as simulation and measurement results. The probes used in the measurement of the waveguiding structures are included and compared to the new designs including a probe with a metal coating applied and one with two-dielectrics. Of key interest are the probes susceptibility to coupling into each other while measuring a device (cross-talk) and their ability to couple power into devices under test. Lastly, a method for imaging with the probes and an Emcore THz frequency domain system is demonstrated to recover images of biological samples including a leaf and a sunflower seed.

## 5.2 Probes

Broad-band dielectric probes are introduced and demonstrated for on-wafer terahertz (THz) device characterization. Dielectrics that are low-loss in the THz region and selective metallization are used to realize the probe designs. The probes are measured and evaluated by themselves and are used to measure on-wafer THz devices. Simulations are done for the probes using ANSYS Electronics Desktop HFSS® and measurements are taken using an Emcore frequency domain THz measurement system. This work was published in [71].

### 5.2.1 Introduction

There is great interest in terahertz (THz) technology and research, especially, with a growing number of on-wafer devices moving towards operation in this frequency range. As device speeds continue to increase to meet burgeoning bandwidth needs, there is a need to easily measure and characterize these on-wafer circuits, systems, and sensors. Although low THz frequencies, around

100 GHz, can be reached using certain network analyzers with frequency multiplier attachments, typical commercially available THz systems that reach frequencies up to around 3 THz (frequency domain systems) or 10 THz (time domain systems) are quasi-optical and thus require probes to characterize on-wafer devices under test (DUTs) or interrogate samples at specific locations such as in imaging, spectroscopy, and sensing applications. Low-loss, wide band, high resolution, single and dual polarized probes are needed to apply these measurement systems to on-wafer or on-board circuit applications.

Various near-field THz probe designs have been proposed in the literature and typically fall within two categories: those that are made with low-loss dielectrics or those that are made with thin wires. An excellent comprehensive review of the THz probing area can be found in [136]. Some proposed designs do not fit into these categories, such as in [137] where probes were micromachined on-wafer from silicon and showed a mean insertion loss of 6.5 dB from 500 - 700 GHz, but probing solutions of this nature are not feasible to apply generally.

The use of thin metal wires is fairly common in the literature, but this approach has the main limitations of high loss and limited bandwidth. Due to the well known skin effect, which specifies that the depth of electric current density in a conductor is inversely proportional to the frequency, the resistive losses due to the conductive material are directly proportional to frequency. Additionally, typically only a limited bandwidth can be supported on a wire guide due to the mechanism of propagation where waves are typically traveling along the surface of the wire.

Wire based waveguides do have some advantages as demonstrated in [138], using a scattering tip operating at 2.64 THz the diffraction limit can be surpassed obtaining resolutions as high as $\lambda/3000$ for imaging applications. In [139], THz radiation is coupled to cylindrical wires where the radiation propagates along the surface of the wire. A scattering mechanism was used to couple into the wires where 0.4 % of the incident power was coupled, then, a radial antenna was used to couple into the wire which improved the coupling to around 56 %. However, in this work the wires were modeled as perfect electrical conductors (PEC) which is not a valid assumption to make given the frequency range. Similar wire based designs can be found in [140] where a variety of different thin metal wires (steel, aluminum, copper, zinc, and nichrome) were used to guide THz pulses as well as in [141, 142].

Although not trivial, it is very feasible to image beyond the diffraction limit when using optical based systems using techniques based on the principle that the distribution of light intensity immediately behind a small aperture is determined by the size of the aperture rather than diffraction or the wavelength of the radiation. This idea has been applied to THz systems in [143, 144, 145] for imaging applications using various types of apertures in metal. In [146] the same principle is used but with a tapered metal tube, the full taper angle being 33°, with a sub-wavelength exit to create a probe like structure, similar work was also done in [147]. However, these aperture based techniques cannot be used for locations of interest far, relatively speaking, away from the aperture as would be needed for on-wafer or on-board probing. Nearly all of literature in this area focuses on imaging, especially planar imaging, applications.

Some of the most practical work has been in using low loss dielectrics, such as Teflon and High Density Polyethylene (HDPE), to realize probe designs. Although, a great deal of the published dielectric probes have only been simulated and tested in the W-Band and have not been vetted for THz systems such as the work in [148, 149, 150, 151, 152]. Literature that has investigated dielectric probes at frequencies directly within the THz region can be seen in [105] where HDPE has been subtractively manufactured to realize a plan-convex lens conjoined with a tapered cone which are used for nondestructive evaluation applications in [30], and in [152] where Teflon probes with a tip diameter of 0.17 mm are demonstrated at 260 GHz to image various samples, such as a leaf and RFID card, with a 0.2 - 0.5 mm resolution.

In looking to move away from the many excellent examples of microfluidic and imaging applications and move towards on-wafer and on-board probing, there are additional parameters to consider such as efficient coupling, between the probe and the device, and limiting cross-talk between the transmitting and receiving probes and nearby devices which are not the DUT. A similar design as shown in [105] has been used in [70, 153] to apply towards a smaller frequency domain system for interrogating high speed waveguides. However, these type of effects such as device coupling and cross-talk were not evaluated thus leaving significant uncertainty in their measurements. As shown in [58], factors such as incoming wave polarization can greatly affect results for rectangular waveguides as were measured in [70].

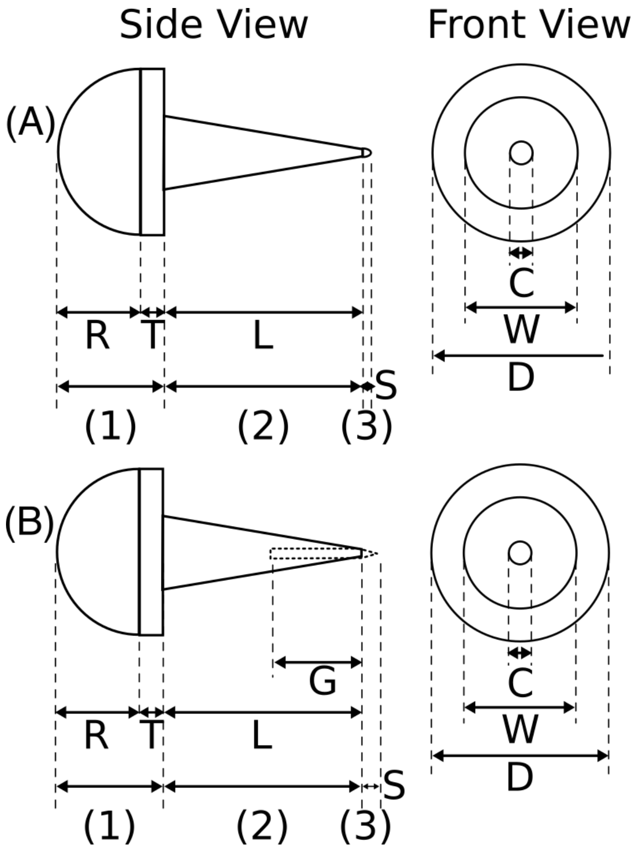

Figure 5.1: Diagrams for the basic probe geometries of a (A) round tip cross-section and (B) two dielectric probe cross-section. For each design, the probe is comprised of a (1) plano-convex lens, (2) tapered cone, and (3) tip.

Here, we investigate the design and fabrication of dielectric based probes for coupling THz waves from a quasi-optical setup into on-wafer probing applications. Simulations were carried out in ANSYS Electronics Desktop using HFSS®. Different designs are explored through simulations and are fabricated, and tested. Both single dielectric and multiple-dielectric based probes are investigated. The probes coupling effectiveness, bandwidth, resolution, and cross-talk susceptibility are evaluated. An Emcore PB7200 frequency domain terahertz (0.1 - 2 THz) system is used to characterize the probes. Details of design, fabrication and test setup are presented. On-wafer probing of example THz waveguiding components are shown.

### 5.2.2 Probe design and simulation

#### 5.2.2.1 Design

The fundamental design of the probes is based on the design principles of plano-convex lenses. The probe is comprised of three elements, a plano-convex lens, a tapered cone, and a tip as can be seen in Figure 5.1. Dimensions of the probes geometries represented in Figure 5.1 can be found in Table 5.2.2.1.

| (A) | Round tip | (B) | Two dielectric |
|---|---|---|---|
| R | 7.5 | R | 7.5 |
| T | 10 | T | 10 |
| L | 30 | L | 30 |
| C | 1 | C | 1.588 |
| W | 11 | W | 11 |
| D | 24.5 | D | 24.5 |
| S | 0.5 | S | 2 |
| | | G | 15 |

Table 5.1: Summary of probe dimensions, units in millimeter (mm).

For the sections of the probe, the tip was made to be as small as possible within fabrication tolerances. The amount of space available for a lens in the THz measurement systems transmitting and receiving heads is limited so a lens radius, $R$, of 7.5 mm was chosen. Using the len's maker's formula, simplified for a dielectric air boundary as seen in Equation (5.1) and using an $n$ of 1.54 for HDPE, a focal length of 14 mm can be approximated. Given that a tapered cone length longer than 14 mm is desired to increase to potential utility of the probe, the critical angle, $\theta_c$, between an air and HDPE boundary can then be found as $\theta_c = \arcsin\left(\frac{1}{1.54}\right)$ to be 40.5°. Then, the slope of the tapered cone can be made such that the electric field being sent through the probe can experience total internal reflection (TIR). The slope of the taper is around 45° which allows the electric field to hit the taper sides at an angle of approximately 80° from the axis normal to the interface which is greater than $\theta_c$ thus allowing TIR.

$$\frac{1}{f} = \frac{(n-1)}{R} \tag{5.1}$$

One other probe design not detailed in Figure 5.1 was used in this work, whose dimensions are the same as in Figure 5.1 (A), but with selective metallization. The selectively metallized design is metallized everywhere expect the tip and the lens. The two-dielectric design is based off the waveguides proposed in [70] to realize an improved tip design. The second dielectric, outlined with a dotted line in Figure 5.1 (B), is alumina with a dielectric constant on 9.2 and loss tangent ($\tan\delta$) of 0.003. In all the designs the main dielectric used is HDPE which has a dielectric constant of 2.38 and loss tangent of 0.002 at THz frequencies [30]. Both the metallized design as well as the two dielectric design are seeking the solve the problem of better field confinement to the probe geometries beyond what one dielectric alone can do. This idea will be further discussed in the simulation section.

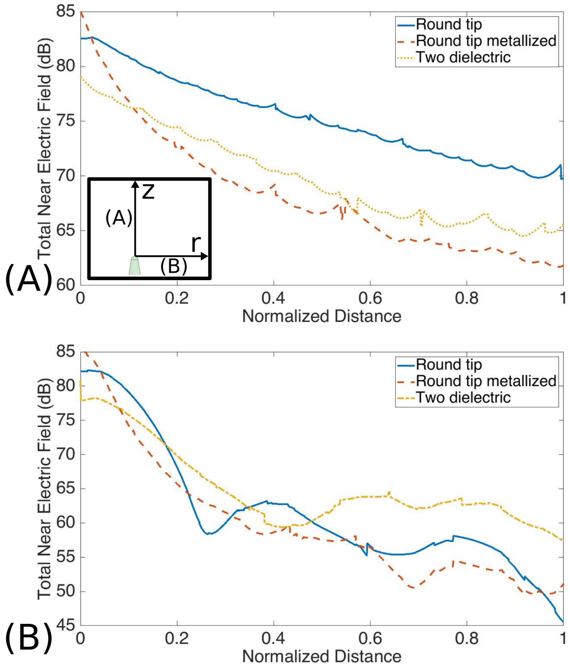

Figure 5.2: Simulation results for the total near electric field, in dB, along a line from the tip of the probe device to 10 mm away from the tip when moving in the (A) axial direction and (B) radial direction as indicted by the figure inset.

#### 5.2.2.2 Simulation

Geometries of the probes were made and simulated in ANSYS Electronics Desktop High Frequency Structure Simulator (HFSS$^{®}$) and simulations were solved on Michigan State University's High Performance Computing Center (HPCC) resource. Models were solved at 100 GHz and a near field radiation setup, of radius one half the total length of the probe being simulated, was used to investigate the total electric field 10 mm from the probe tip in the radial and axial direction (moving away from the tip) as well as the electric field confinement along the entire probe geometry. It is fairly common in the literature of this area to only investigate the tip of a probe in simulation, however, such results are fairly meaningless unless you can guarantee what the electric field will look like upon entering that section of the geometry.

In Figure 5.2 the potential benefits of a modified probe can be seen as it is most desirable in an idea probe to keep the electric field as confined to the probe tip as possible. In Figure 5.2 (A), the total electric field decreases with distance much faster with the modified probes than with the purely dielectric device. The modified probes electric field strength drops by an order of magnitude 4 mm away from the tip when it takes a full 10 mm for the purely dielectric probe. Additionally, in Figure 5.2 (B), which gives an idea about the beamwidth that can be expected from the fabricated devices, the beamwidth is much smaller for the modified probes. To find an estimate for the beamwidth from Figure 5.2 (B) the distance the electric field strength drops by 3 dB (half strength beamwidth) can be seen, which, for the rounded tip probe happens at 1 mm, for the metallized probe at 0.42 mm, and for the two-dielectric probe at 0.01 mm.

Figure 5.3 allows us to visualize similar information to Figure 5.2 but for the entire geometry as opposed to focusing on the tip. The 0° position is the center of the tip of the probe and shows an obvious maximum. The position of ± 180° is the center of the lens section of the probe where there is effectively no field strength (three orders of magnitude less). The beamwidth in degrees can be estimated by seeing where the electric field strength drops by 3 dB which for the rounded tip probe is about 4.5°, for the metallized probe 4°, and for the two-dielectric probe 3°.

Figure 5.4 shows the simulated electric field confinement through the three proposed probe

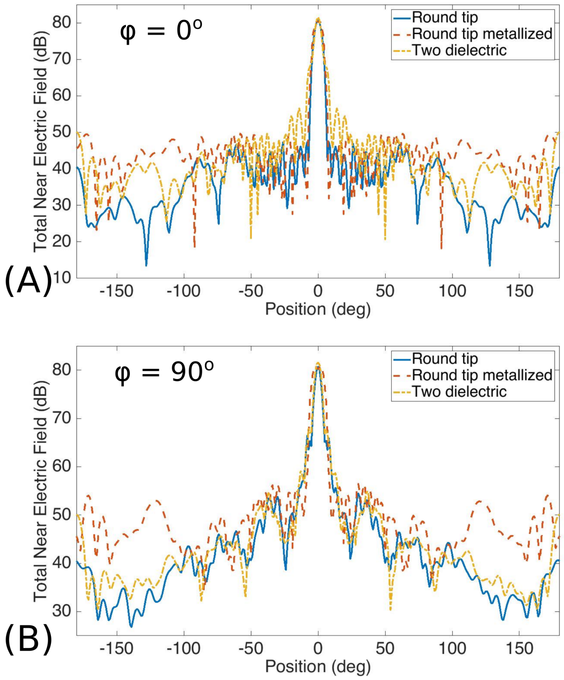

Figure 5.3: Simulation results for the total near electric field on a sphere along the (A) $\phi = 0°$ and (B) $\phi = 90°$ planes.

geometries. In simulation a symmetry boundary was used to cut the probe geometry in half to reduce computational cost and a waveport was used to excite the structure. By looking at the electric field confinement along the entire structure and not just at the tip more of the probes expected behavior can be confirmed. All three structures show the point of TIR about halfway in the tapered cone section of the probe as was discussed in the design section and expected. Additionally, all three structures show their greatest electric field concentration at their tip, as desired.

### 5.2.3 Fabrication methods

The dielectric body of the probes were machined by using a computer numerical control (CNC) tool to shape a block of HDPE into the desired probe geometry. The files used for the CNC were directly export as parasolid files from the HFSS® modeling software. After machining, a fine grade sandpaper was used to make the surfaces as smooth as possible.

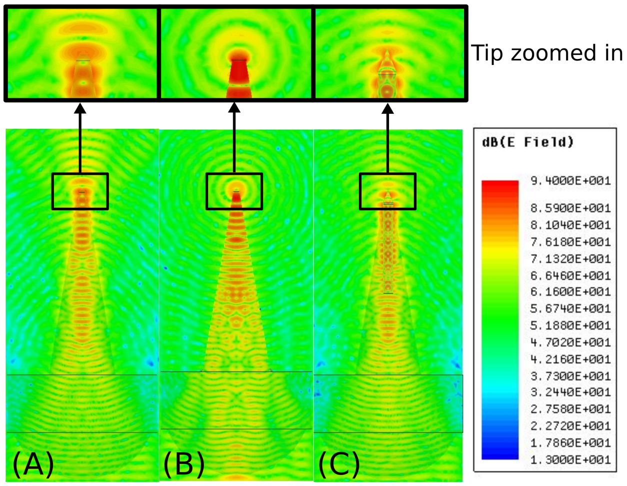

Figure 5.4: Simulated electric field confinement through the (A) rounded tip, (B) metallized rounded tip, and (C) two dielectric probe with insets of a close up on their tips.

Metallization was done using a sputtering deposition technique with copper using a Denton Desktop Pro sputtering system. The probe body where metal was not desired was covered using a polyimide tape. A thin, 60 nm, layer of titanium (Ti) followed by a 1 µm layer of copper (Cu) is deposited onto the exposed regions of the probe geometry to achieved the desired patterning. The alumina rod was shaped by hand using a dremel and inserted manually into the probe geometry. Final devices can be seen in Figure 5.5.

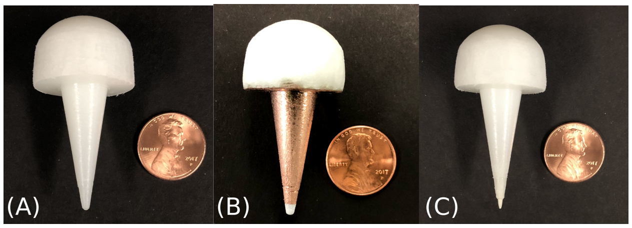

Figure 5.5: Fabricated probes including the (A) rounded tip, (B) metallized rounded tip, and (C) two dielectric probe.

The two dielectric probe proved the most challenging to realize well because although the geometry excluding the alumina rod could be directly tooled, the tooling is precise enough that when inserting the alumina piece there is nowhere for the air in the alumina rod shaped cavity to escape. A small air outlet hole was bored into the side of the tapered cone where the alumina rod cavity ends to alleviate this problem, but, there is still not a perfect seal between the rod and the HDPE here which affects performance later. In the future an injection molding like fabrication such as was used in [66] might be better suited for this style of design to eliminate this problem.

### 5.2.4 Measurements and results

Transmission measurements were taken using a quasi-optical THz measurement system, the commercially available Emcore frequency domain PB-7200. Measurement setup details are shown in Figure 5.6 where (A) and (B) show the two different transmission setups; (C) and (D) show two different probe positions for coupling into an on-wafer device.

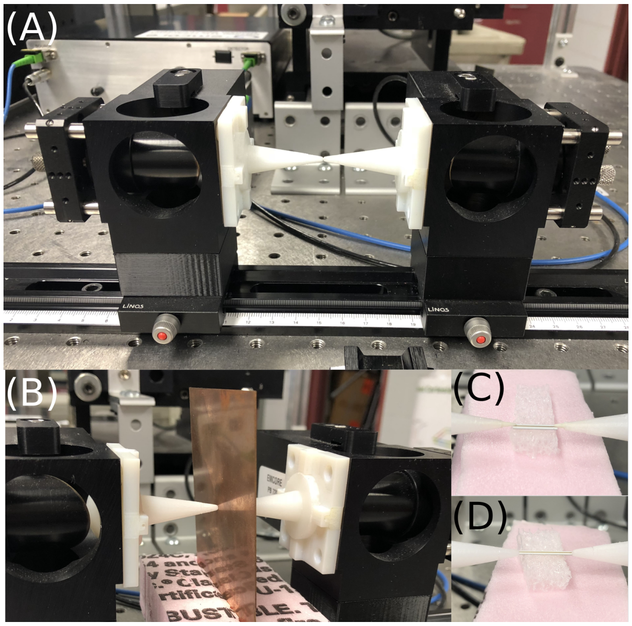

Figure 5.6: Details on measurement setups where (A) shows the setup for total tip to tip transmission, (B) for transmission through a restricted window (1 mm diameter), (C) probing a device by coupling onto the top, and (D) probing a device by edge coupling.

#### 5.2.4.1 Transmission

The THz system measures the total power, in arbitrary units, that is received at the receiver head from the transmitter head. This measurement includes any effects that could affect the total power between the two heads such as differences in the atmosphere (THz radiation is very sensitive to moisture), misalignment between the focusing mirrors, misalignment between the two probes, or interfering signals, in addition to any effects that could be due to the probe design and fabrication methods alone. Therefore, it is important to normalize measurements relative to a background in order to ignore other possible interference and attribute our results solely to the proposed designs and fabrication in this work.

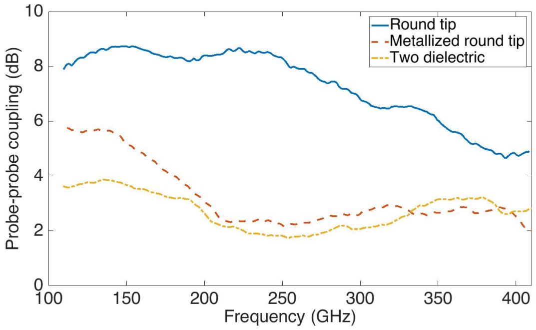

Figure 5.7: Probe to probe coupling results of the probe designs when measuring transmission tip to tip normalized to those measured with a restricted window (1 mm diameter).

Shown in Figure 5.7 are the probe to probe coupling results of the probe designs when measuring using the setup shown in Figure 5.6 (A) and (B), where they are positioned tip to tip in free space and when restricted to a window of 1 mm diameter (the size of the probe tips), respectively. The latter measurement allows us to isolate how much power is being directly transmitted through the probe tips to some DUT versus how much power transmission could be due to cross-talk between the probes. In comparing the probes transmission directly through their tips versus including mutual coupling, it is clear that the purely HDPE probe has the most mutual coupling. It is also interesting that the two-dielectric probe has comparable mutual coupling to the metallized probe which indicates that the the probe has good field confinement supported by the boundary between the two dielectrics.

#### 5.2.4.2 Coupling and on-wafer measurements

To determine the amount the coupling efficiency of the probes into a DUT two known devices, a 50 Ω microstrip on an alumina substrate, of substrate height 0.4 mm and length of 12 mm, and an alumina rod, of diameter 1.588 mm and length 18 mm, were used. Here, feature scaling was used, or data normalization, to restrict the range of the amount of power coupled into a DUT from 0 to 100 %. The formula used for this is provided in Equation (5.2) where $X$ is the measured power coupled through the DUT and $X'$ is the normalized power coupled through the DUT.

The power transmitted between the probe under test when measured tip to tip, as seen in Figure 5.6 (A), is used as the $X_{max}$ or relative 100 % and the power transmitted when the probes are the DUTs length away with air between them is used as the $X_{min}$ or relative 0 %. The resulting $X'$, or normalized power coupled through the DUT, is actually a reflection of two coupling events, from the transmitting probe to the DUT and from the DUT to the receiving probe. Therefore, assuming similar probe coupling efficiencies, the results in Table 5.2.4.2 were found for a single probe which would be the square root of $X'$.

$$X' = \frac{X - X_{min}}{X_{max} - X_{min}} \tag{5.2}$$

Coupling results can be found in Table 5.2.4.2 for select frequencies where the % of power coupled is per probe for an edge coupling setup, as seen in Figure 5.6 (D). Values of 0 or 100 % denoted with an asterisks indicates that the value obtained with the calculation processes detailed above was invalid but tended toward 0 or 100 % (invalid meaning a value outside the range of 0 to 100).

In Table 5.2.4.2 it is clear that overall the proposed probes significantly coupled power into the DUTS, that the coupling into the alumina rod was typically more efficient than for the microstrip, and that for all probe devices coupling decreased with frequency, which would be expected. These results are especially promising for the potential with the two-dielectric probe. Although its

|  | 150 GHz | 250 GHz | 350 GHz | 450 GHz |
|---|---|---|---|---|
| 50 Ω alumina microstrip |  |  |  |  |
| Round tip | 11.3 | 9.9 | 11.7 | 6.3 |
| Metallized round tip | 24.2 | 36.2 | 32.7 | 31.6 |
| Two dielectric | 2.9 | 14.1 | 10.8 | 8.8 |
| alumina rod |  |  |  |  |
| Round tip | 65.9 | 64.2 | 53.6 | 25.0 |
| Metallized round tip | 78.0 | 100* | 57.4 | 0* |
| Two dielectric | 0* | 22.7 | 14.6 | 7.9 |

Table 5.2: Summary of on-wafer coupling measurements, units in % power per probe for edge coupling.

coupling efficiencies were lower than the other designs, simulation and the other measurements indicated that it had better field and power confinement to its tip and, given its method of fabrication, could allow for more customized and replaceable tips.

### 5.2.5 Discussion

Although both edge and top coupling were investigated, only edge coupling is appropriate for this probe designs presented in this work. As Figure 5.8 illustrates, for a top coupling scenario the probe tips in this work do not make good contact with non-flexible DUTs as were measured in this work. In future work, tip shapes that are designed with top coupling in mind will be used to achieve better coupling in a top coupling configuration. Top coupling is preferable to edge coupling for on-wafer probing given that wafers, and boards, are rigid, two dimensional spaces to investigate.

Another interesting implication from this work to be further investigated in future work is "replaceable tips". With improvement in the two-dielectric probe fabrication to improve measurement results, namely to eliminate its air gap where the alumina meets the HDPE and to better shape the tip, a variety of customized, interchangeable tips could be used.

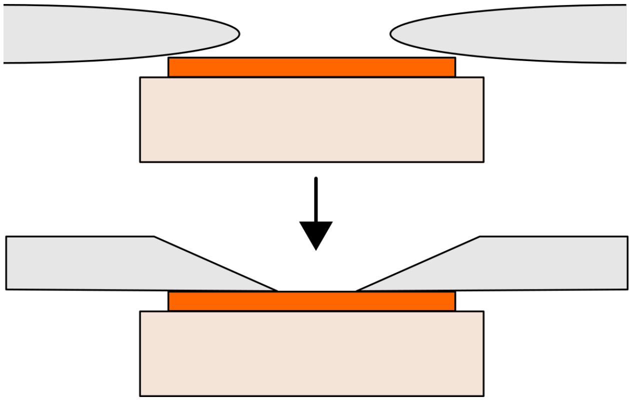

Figure 5.8: Illustration of future work to achieve good top coupling for on-wafer probing given the implications of this work.

## 5.3 Imaging

### 5.3.1 Background

Some background in the area of THz imaging was previously discussed in Section 1.1.2.2 and an overview of measurement systems given in Section 1.1.3 but medical imaging in general has been been discussed in a great detail. More generally in the area of THz imaging the key challenges are: (1) the acquisition time, (2) the spatial resolution and penetration depth, and (3) data visualization and interpretation.

Acquisition speed for imaging, when compared to established medical imaging systems, is very slow. Speeds range from a few thousand pixels per second to a few seconds per pixel and there is a trade off between acquisition speed, spectral resolution, and signal to noise ratio (SNR). By monitoring only peak height or position rather than the full THz waveform speed can be increased but at the cost of spectral resolution. In some cw systems the beam can be broadened to cover the entire sample and, with an array of detectors, image the sample all at once but at a great cost to the SNR. Since sources are costly and generally only one can be employed by a system, raster scanning, where the source will measure one pixel at a time, is most commonly used which gives a slow speed but high SNR. Minimizing the number of measurements needed to construct an image could greatly improve the imaging speed or by moving away from the current standard of raster scanning.

Developing methods utilizing arrays of detectors, compressed sensing techniques, sparse arrays or synthetic aperture imaging would greatly increase acquisition speeds by allowing systems to acquire more than one pixel at a time. In [154] and [155] compressed sensing techniques were demonstrated for increasing acquisition speed, instead of imaging an object directly it is imaged by piecing together the transmitted light through random screens. Using this method a single detector is still used so a high SNR can be maintained. When using the compressed sensing, an $N \times N$ pixel image can be resolved with less than $N^2$ measurements and does not require raster scanning. In [154] a $32 \times 32$ (in pixels) image is recognizable after 300 measurements which is 30% of the measurements that would have been needed if raster scanning was used and images taken in [155] showed similar results.

Using sparse arrays and imaging techniques from synthetic aperture arrays [156] and [157] are able to resolve images by measuring the reflected electric field off of samples and applying a time delay between receivers. In [157] video imaging was demonstrated with a rate of 62.5 frames/second by combining a synthetic aperture array with a cw source to achieve interferometric imaging. Another interesting approach to speed up acquisition time was demonstrated in [158] where an optical character recognition (OCR) algorithm was used to determine how well they could imaging a sample which had a string of four metal letters on it using different frequencies in the THz region. The images taken with the fastest speed, and therefor really compromised SNR, could still generally be picked up by the OCR correctly. If algorithms similar to those for OCR could be developed for other structures as well then the SNR trade-off for faster acquisition times can be somewhat side stepped.

As mentioned previously, another option could be to use an array of detectors that pick up on the reflected or transmitted field all at once. There are a number of drawbacks with this approach for *in vivo* imaging. Since the image would need to be taken in reflection mode the SNR would be very poor, but more importantly, in order to image the type of structures that would be in the skin level (where THz is mostly limited to) would require very good resolution. Currently THz detector arrays for imaging are very small and typically demonstrate their ability to image simple shapes that around on the order of centimeters in size. Although using a detector array would provide the greatest speed, the technology is not currently developed enough for use in biomedical imaging.

Spatial resolution is one of the most important parameters for THz imaging capabilities. In the far-field, it is controlled by the diffraction limited spot size at the focus of the THz radiation. Given the wavelengths in the THz region spatial resolution in the far-field it can at best be around 100 µm to 1 mm but can be improved by confining the detection scheme to the near-field. Therefor, by bringing the sample within the immediate vicinity of the detector, sample resolutions as good at around 25 µm can be achieved (which is $\lambda$/24 at 0.5 THz) [43]. According to [17] typical spatial resolution is 20 µm axially and 250 µm laterally. Penetration depth was discussed more in-depth in Section 1.1.2.2 where, overall in moist biological tissues THz radiation can realistically penetrate about 82 µm.

Resolutions at this magnitude are similar to other established medical imaging technologies, but for applications where the target to be imaged or interrogated is very small, significantly smaller than a wavelength, near-field imaging needs to be used. Near-field imaging is based on the principle that the distribution of radiation behind a small aperture is a function of the diameter of that aperture instead of being a function of wavelength. Since bringing a sample to be imaged within very close proximity of the source is not always ideal or feasible, other workarounds have been made. One of the more popular methods for achieving high resolution near-field imaging is using probes. When using probes, the resolution is determined by the spot diameter of the probe and not by the incident THz beam. Using a metal tipped probe, spot sizes as small as $\lambda/200$ have been achieved [159].

There are many ways to visualize data taken with pulsed and cw THz systems that yield different information to the viewer. As with any imaging technique the question of how to extract useful information from the raw data taken is paramount. In pulsed laser systems, as the pulse travels through the sample changes to the pulse such as attenuation, broadening and delay can be directly correlated to physical processes that occur in the sample such as absorption, optical thickness, reflection at the samples interfaces, scattering, and diffraction. In cw systems physical properties or processes that have frequency dependence can be clearly observed. Additionally, better SNR is yielded when using TD methods (in general), and schemes that look at a parameter relatively (with respect to a reference) not only provide better SNR but eliminate artifacts or effects from mechanisms not under observation.

A vary comprehensive overview of different visualization schemes is covered in [160], where an alcohol-dehydrated, formalin-fixed and paraffin mounted thin-cut canary's head is imaged. Using a pulsed system, raw data was taken for each pixel and then was manipulated mathematically in creating the resulting canary head images. The time dependent electric field was measured and the images were built using raster scanning. At each pixel a time scan of the transmitted THz pulse was taken and typically took about 17s per pixel to acquire. Overall the methods used were variations of looking at relative power loss, time delay and deflectance (dark field) due to the sample.

The resulting images of the canary head in [160] are very different and could potentially provide different information to the viewer. Looking at the relative power loss the viewer can gain insight about the loss due to absorption, reflection, scattering and diffraction, in the frequency domain analysis, knowledge about the frequency dependence of losses can be drawn as well. Time delay information can be related to the refractive index of the sample. Dark field imaging can provide image contrast improvements and potentially give information on spatial features beyond the resolution of bright field imaging. A previous publication from the same research group [161] first introduced dark field imaging for THz. In this publication they demonstrate the techniques promise for biomedical applications by imaging tumor boundaries since the largest medical distinction between benign and malignant tumors is based on differences in the boundary between tumor and healthy tissue. Since diffraction and scattering are greatly increased at boundaries dark field imaging could provide better detail than bright field imaging for such an application.

The main problem with the images in [160], is that although we can clearly see the effects of something like power loss, there is no good understanding of the mechanisms that cause that loss. Therefor, we cannot say how much of it is due to absorption or scattering, etc. In applications where imaging biological tissue is demonstrated, the loss is always attributed to absorption due to the tissues water content and no further thought is put to the matter. This kind of fundamental understanding is something greatly lacking in the study of THz imaging that will need to be addressed.

Another method of visualizing data is polarization based imaging. In [162] this method of visualization is explored in the THz region which holds the possibility of simultaneously measuring both transversal electric field components. Other visualization methods only capture one component of the electric field which makes a difference when interpreting data. For example, with only one field component a decrease in amplitude of the field is commonly attributed to absorption or scattering but it is possible to observe such a decrease due to the rotation of the electric field vector which could be induced from a sample by a variety of mechanisms (ex: birefringence, not-normal incidence of reflection, multiple scattering). The authors use a circularly polarized source to measure a polystyrene foam sample (which exhibits good birefringence) and image a coin. They are able to measure the different field components using a unique detection scheme with a $< 111 >$ oriented electro-optic crystal, a quarter wavelength plate and a Wollaston prism. A method for imaging, using polarization in THz, not explored in this paper nor elsewhere that I could find, would be to measure a sample with different polarizations of the source and piece the results together to create an image (polarimetric imaging). It is known that man made structures tend to favor different polarizations (such as linear polarizations) than natural structures. This could show possible medical application to detect skin level ailments (tumors, lesions, wounds) or foreign items (shrapnel, staples) that favor a different polarization than healthy skin.

### 5.3.2 Goal

As mentioned previously, THz imaging is non-ionizing and therefore not harmful to biological tissues but its susceptibility to absorption in water molecules is considered a great disadvantage to the use of THz radiation for biological imaging as biological samples typically have a high water content. It is generally thought that terahertz high absorption in water is due to waters librational mode and rate of diffusion falling within the terahertz range. Within a mass of water molecules each molecule will hydrogen-bond with, on average, 3 to 4 other water molecules at any given time. These hydrogen bonds are in a constant state of flux and will librate on a subpicosecond time scale. Diffusion of water molecules happens on a picosecond time scale. Between these two mechanisms fluctuations in the water network and therefor fluctuations of the water dipole moments lead to strong terahertz absorption since the time scale, sub-psec and psec, fall within the terahertz range (1 THz = $10^{12}$ Hz = 1 $psec^{-1}$). This is disadvantageous because this phenomena limits the penetration depth THz radiation could have in samples.

However, for thin biological samples, this would not be an issue. Additionally, this sensitivity to water is quite advantageous for applications that specifically seek to monitor, track, or discover the high or low moisture present in biological samples. Two such applications here are shown including the non-invasive imaging of a food product and investigating the moisture content of a leave in the process of changing its color.

A raster scanning method is used to perform the imaging and the measurement methodology is evaluated. Although a set of single dielectric polyethelyene probes are used for this work, it could easily be applied for use with a modified probe design as found in Section 5.2 in future work. The modified probes presented in Section 5.2 would allow a finer resolution and, in-conjunction with work shown in Section 4.3 would allow simple integration of filter in the system to remove noise from the measurements pre-processing.

### 5.3.3 Methods and measurement setup

The Emcore THz systems ability to perform imaging on biological samples was evaluated using a set of the HDPE probes for the THz system in conjunction with a Parker motorized XZ stage run by an automated program and a homemade Python code automating the THz system controls. The test setup can be seen in Figure 5.9 where the different elements to the setup have been annotated.

The sample to be imaged was fixed to the Parker motorized stage using general optical post assembly pieces and positioned between the two probes attached to the THz transmitting and receiving heads. The probe tips are as close to each other as possible while still allowing enough

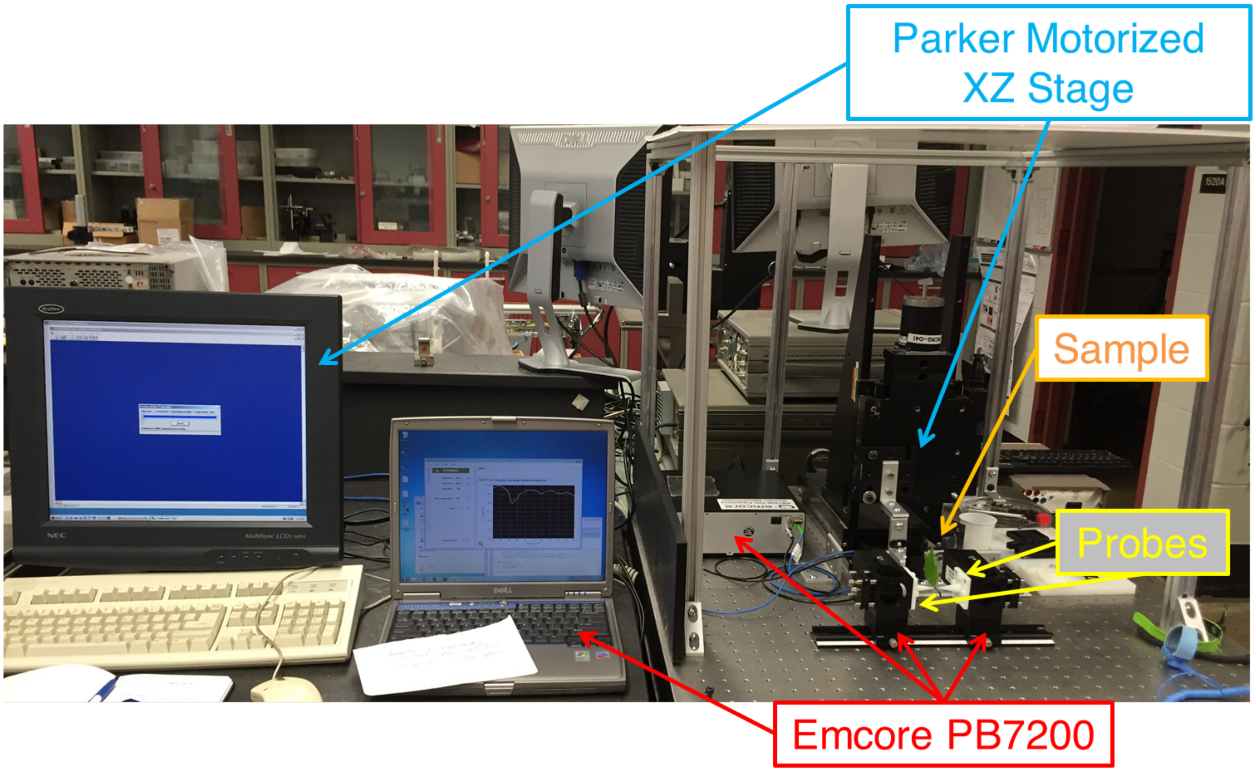

Figure 5.9: Equipment setup to take automatic transmission measurements through a sample with the Emcore THz system to later create an image.

room for freedom of movement of the sample, typically a few millimeters of space. The Parker motorized stage can be manually operated or used to run a predefined program, detailed instructions on using the Parker motorized XZ stage as well as sample code that was used to move the sample to recreate an image are included in Appendix H and I respectively. Initially, the stage was manually positioned so the probes were in position for the first desired measurement and then a program was run which performed a rasterized scan of the sample. The program controlling the stage was timed to be working in concert with the THz measurement system so the stage only moved after a frequency sweep of a point on the sample was complete. This timing was determined by trail and error performing small sample imaging tasks. On the computer controlling the THz measurement system a Python program was running, using the same time as the stage, to click the mouse on the "Start Scan" command for the machine.

### 5.3.4 Results and discussion

Two leafs (bio-samples), a sunflower seed, and a copper square on foam board were imaged for this work. The copper square acted as a test since the likeness of the constructed image is easy to visually check against the sample. It also has a clear theoretical answer; anywhere there is copper should have no transmission and anywhere there is foam should have some transmission. This test image matched its theoretical result fairly well, as can be seen in Figure 5.10, it is clear that there was some drift between where the program thought the interrogating probe was and where it actually was and that there were some effects around the edges of the copper square. Overall the image was 11 × 10 pixels where each pixel is roughly 1 $\text{mm}^2$, the image was taken around 300 GHz and it took a total time of 2 h, 8 min, and 10 s to acquire (roughly 70 sec/pixel). The pixel size corresponds to the physical dimension of the tip of the probes used which is around 1 mm in diameter. The program controlling the motorized stage to move the sample also loved in 1 mm sized steps to correspond to the spot size of the imaging probe tip.

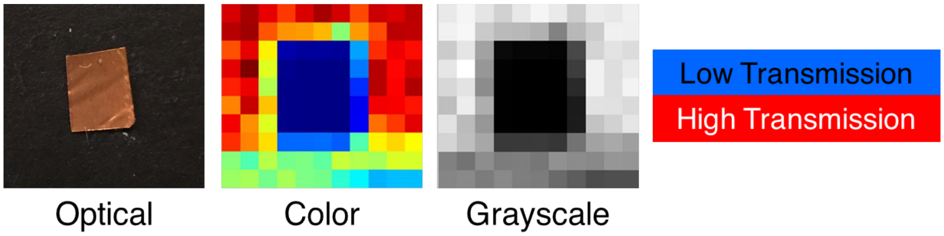

Figure 5.10: Sample image of a copper square on foam board where the copper should give no transmission and the foam board should allow the THz signal to pass.

The two most interesting leaf results are shown in Figure 5.11, where the top image shows an ivy leaf and the bottom image shows an ivy leaf with a blemish. The top leaf image is 31 × 29 pixels where each pixel is roughly 1 $\text{mm}^2$, the image was taken around 300 GHz and it took a total time of 18 h, 10 min, and 43 s to acquire (roughly 70 sec/pixel), the bottom leaf image is 20 × 17 pixels where each pixel is roughly 1 $\text{mm}^2$, the image was taken around 300 GHz and it took a total time of 5 h, 12 min, and 50 s to acquire (roughly 55 sec/pixel). The second leaf had a shorter average pixel time because I took my measurement for that one using a narrower frequency band around

300 GHz. Overall, in the leaf images the veins and boundary of the leaf are well defined. The leaf with the blemish, a notably “dryer” spot in the leaf where its color was starting to turn, had a much higher transmission which makes since as the blemish was caused by the leaf starting to lose moisture content. The blemishing area on the leaf is much more obvious in the image taken using THz radiation than what can be observed optically showing that using THz radiation for passive monitoring could reveal behavior in deciduous trees coloring turning well before they are visually appearant.

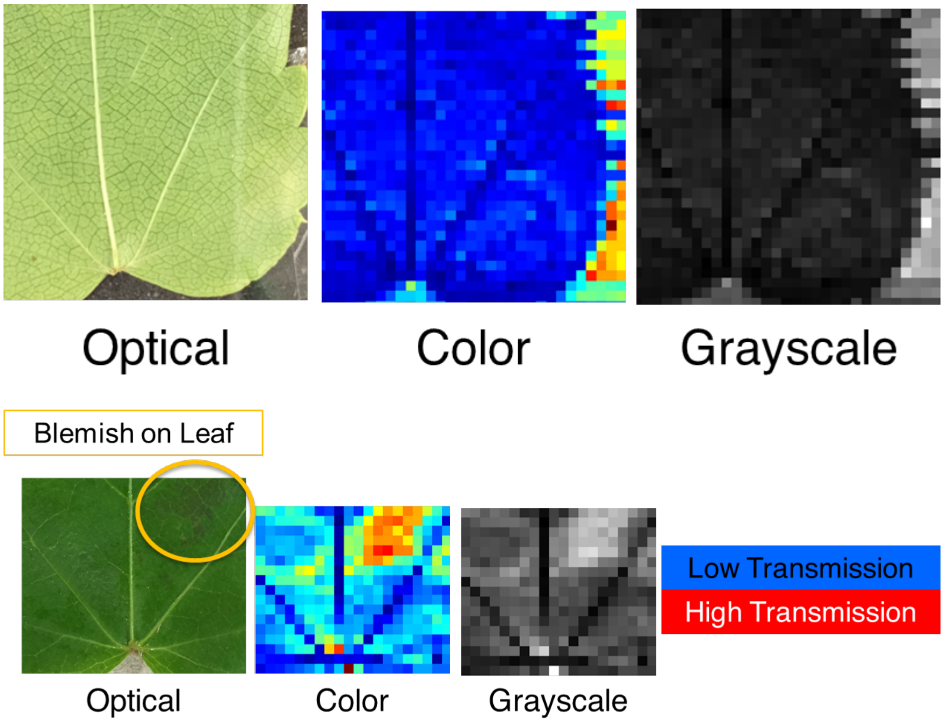

Figure 5.11: (Top) Fresh ivy leaf from the Engineering Courtyard and (bottom) a similar leaf which has a blemish.

Using THz imaging for a non-destructive evaluation application was done by imaging a shelled sunflower seed, as seen in Figure 5.12. The seed was imaged with its shell on, then, after taking the image, the shell was removed so that the actual inside of the seed could be directly compared with the image taken. The seed image is 46 × 20 pixels where each pixel is roughly 0.5 $\text{mm}^2$, the image was taken around 300 GHz and it took a total time of 14 h, 47 min, and 48 s to acquire (roughly

55 sec/pixel). Here, the motorized stage took smaller steps to achieve the smaller pixel size while using the same measuring probes. This would not be possible give the probe tip geometry if an imaging array were being used as there would have certainly been cross-talk between the array elements but since the imaging is done using a rasterized scanning technique the only concern is that the measuring might be affected by the field interacting with surrounding area in the sample. However, as can be seen in the image, the seed and shell boundaries remain clear. A finer step sized had been checked on a less complex sample to check if there was blurring or aliasing in the image prior to imaging the seed.

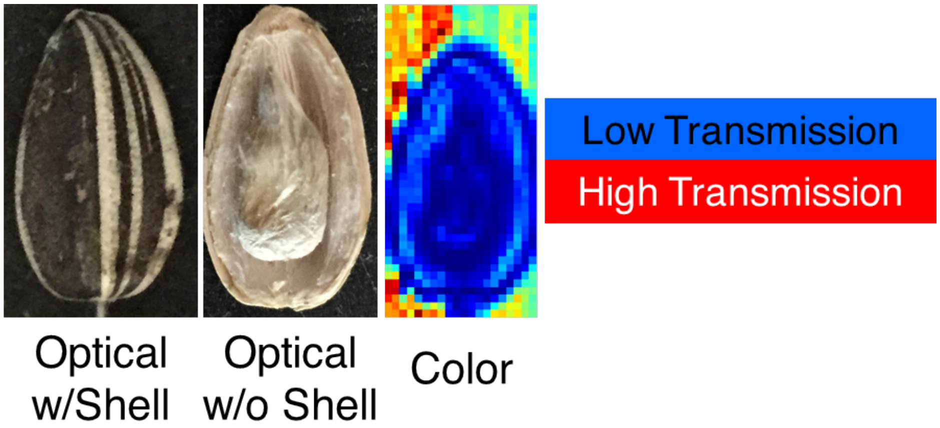

Optical w/Shell

Optical w/o Shell

Color

Figure 5.12: Sunflower seed imaged non-destructively, with its shell fully intact.

The THz image gave a very good representation of the seed. It could easily be seen that the seed what not physically damaged and, if a THz system with phase information were used, it could be possible to identify defects such as rot, mold, or insects as a means for food safety and quality control.

### 5.3.5 Future work

As presented here, the use of the cw THz system is too slow to apply the imaging technique to biological samples that require a limited time frame, for example, samples which require refrigeration. The resolution of the system is limited by the performance of the probes used could be improved by the use of some of the probe improvement proposed in Section 5.2. Data interpretation using this system is straight forward which is both an advantage and a disadvantage. Its simplicity allows data taken to be easily and quickly used to reconstruct an image of a sample and correlate high power values (in arbitrary units) to high transmission and therefore low moisture content, and contrarily low power values to correlate to low transmission and therefore low content of moisture or other THz absorbing materials. However, without phase information as well specific spectra or material properties cannot be extracted to provide more meaningful analysis of sample such as determining a root cause for a high or low reading (ex: moisture due to rot versus a mold).

The THz system used here does experience interference peaks when the received signal and the reference signal have a difference in path length which could be correlated with a phase shift in theory. Using the shifts in interference peaks in this system could allow a user to get both pieces of information to recovered material property data.

## 5.4 Conclusion

There is a need for inexpensive, low-loss, dielectric based probes for THz measurements which can obtain high resolution for sensing and imaging as well as having a high coupling efficiency and minimized cross-talk for on-wafer or on-board devices characterization. Here, some improvements have been made to meet these needs by introducing and evaluating designs to fit low-cost frequency domain THz system heads, to show the utility of customizing the tip shape, and showing how polarization can be maintained and cross talk minimized by applying a minimal amount of metalization. The imaging application demonstrates that the low-cost, relatively speaking, CW Emcore THz system could be used for getting amplitude based images at THz frequencies. The method demonstrated could be performed using the newer proposed probes as well and possibly get a finer resolution image.

# CHAPTER 6

# CONCLUSION

## 6.1 Conclusion and future work

### 6.1.1 Conclusion

Current trends in consumer and non-consumer electronics show a clear need for high-speed circuits, and, therefor, for circuits which are wideband. Despite the excellent work and results in addressing these needs in optical circuit design, there is still an incentive to reaching a solution which is entirely electric as far as reducing power consumption, board real-estate, design complexity, and increasing the ease of integration with pre-existing systems. Thus, the work presented here offers a feasible approach for wideband circuit design which makes use of millimeter wave through THz frequencies. The general composition of the proposed waveguiding design allows for the benefits of the well studied dielectric ribbon waveguide while offering a solution to its susceptibility to cross-talk which would allow this design to, with further optimization, be used in high density on integrated circuits. The possibilities with implementing the proposed guide offer a solution that presently is not completely satisfied by current traditional waveguiding structures such as microstrips, substrate integrated waveguides, or dielectric ribbon waveguides.

The prototypes in this work showed good agreement between theory, finite element modeling simulation, and measured results. The agreement being, that the proposed guides have low signal reflection, high transmission, and are wideband. Additionally, a number of other circuits and sensors designs which were based off of the design principles for the basic waveguides were also assessed. These additional applications demonstrated for the base waveguide design show how the design could be extended to create a suite of wideband circuits to address needs in future electronics systems.

### 6.1.2 Future work

Although promising, there are still many challenges left to address before the proposed design could be more rigorously vetted and possibly integrated into a larger system. Many of these challenges were discussed within this document near their most relevant topic but will be briefly summarized here. The future challenges primarily fall within two categories: (1) materials and manufacturing and (2) measurement and integration.

In order to simplify fabrication, additive manufacturing methods were employed in this work to realize the prototype guides. However, in order to reduce losses and shrink the guide geometries it would be more advantageous to use conventional materials such as, for the high dielectric constant core, using a high resistivity silicon, sapphire, or a low-loss ceramic composite and, for the cladding, low-loss material such as high or low density poly-ethylene or zeonor. However, the main advantage of employing the additive manufacturing techniques is their ability to be easily applied to substrate integration. More traditional materials would not allow easy integration, so in order to more forward with an additive manufacturing technique, the materials available for 3D printing would need to be improved. This would include lowering the loss of 3D printed plastics, making high dielectric materials commercially available, and improving the ability to print with conductive materials. If more variety in dielectric constants were available, then the proposed guides could be printed directly. Further, if the resolution of commercially available printers were improved then small dielectric based circuits such as those discussed through simulation in Section 4.3 could be readily realized.

The measurements performed in this work accomplish the main task of providing a proof of concept and allow comparison with simulation. However, a more reliable measurement system would greatly improve the confidence in the measurements as well as the quality of the results. For example, if a measurement system more similar to a vector network analyzer would have been able to be used, then reflection measurements could have been captured simultaneously with the transmission measurements to get a more full picture as to loss in the guides. In order to integrate a waveguiding design of this nature into larger systems, or possibly more advanced testing equipment, transitions would need to be designed and developed to allow the proposed waveguide to communicate with the already established conventional waveguiding designs, especially, microstrips. Similar to designing transitions between the proposed guide and conventional guides, significantly more work would need to be done on how to properly excite the proposed guide in order to assure specific behavior with regards to the modes present in the guide.

Additionally, there are even still further extensions of the proposed design that were not explored in this work which could be investigated in the future. This wouls include a detailed study of the optimal core and cladding ratio cross-section to achieve lower loss, larger bandwidth, while miniaturizing the design. This waveguide could be used to realize multi-level waveguides and to provide the co-integration of passives with actives. Lastly, a greater exploration of tailoring dielectric cross-sections for specific applications such as tailored cut off frequencies, targeting specific mode excitations, and transitioning to other devices (or free space).

# APPENDICES

# APPENDIX A

## PYTHON CODE FOR SOLVING CHARACTERISTIC EQUATION

```
#------------------------------------------
import numpy as np
import scipy.constants
from scipy import zeros
import matplotlib.pyplot as plt

#------------------------------------------
# Define Newton Method Solver
def newton(xstart,fn):
    x = xstart
    eps = 1e-8
    xold = x + 10*eps
    delta = 0.1
    maxloops = 50
    for loops in range(maxloops):
        fval = fn(x)
        dfdx = (fn(x + delta) - fn(x))/delta
        xold = x
        x = xold - fval/dfdx
        if (abs(x - xold)<eps) and (abs(fval)<eps):
            return x
        else:
            pass
            #print no solution :(
```

```

#---------------------------------------------
# Variables
a = 3.8e-3
b = 1.3e-3
c = 0.64e-3
d = b
er1 = 2.8
er2 = 9.2
er3 = er1
tand1 = 0.04
tand2 = 0.003
tand3 = tand1
e = scipy.constants.epsilon_0
u = scipy.constants.mu_0
c0 = scipy.constants.c
pi = scipy.pi
eps1 = e*er1*(1 - 1j*tand1)
eps2 = e*er2*(1 - 1j*tand2)
eps3 = e*er3*(1 - 1j*tand3)

n = 1 #mode number in height
m = 1 #mode number in width
fc = (1/(2*pi*np.sqrt(u*e)))*np.sqrt((m*pi/a)**2+(n*pi/b)**2)
fc_low = (1/(2*pi*np.sqrt(u*e*er1)))*np.sqrt((m*pi/a)**2+(n*pi/b)**2)
wc = 2*pi*fc_low
start_f = wc
```

```
stop_f = 3*wc
res = 0.5e9
numpnts = int(np.ceil((stop_f-start_f)/res))
omega = np.linspace(start_f,stop_f,numpnts)

#-----------------------------------------
# Solve for kz
kz = zeros(numpnts)+1j*zeros(numpnts)
flag = 1

for i in range(0, numpnts):
    if (omega[i] > wc):

        k0 = omega[i]/c0
        k1 = omega[i]*np.sqrt(u*eps1)
        k2 = omega[i]*np.sqrt(u*eps2)
        k3 = omega[i]*np.sqrt(u*eps3)

        #-----------------------------------------
        # Define Characteristic Equation
        def char_eq(kz_temp):

            beta_y1 = np.sqrt(k1**2 - kz_temp**2 - (m*pi/a)**2)
            beta_y2 = np.sqrt(k2**2 - kz_temp**2 - (m*pi/a)**2)
            beta_y3 = np.sqrt(k3**2 - kz_temp**2 - (m*pi/a)**2)

            term1 = beta_y3*np.sin(beta_y2*(c-b))*np.cos(beta_y3*(d-c))
```

```
            term2 = beta_y2*np.sin(beta_y3*(d-c))*np.cos(beta_y2*(c-b))
            term3 = beta_y3*np.cos(beta_y2*(c-b))*np.cos(beta_y3*(d-c))
            term4 = beta_y2*np.sin(beta_y3*(d-c))*np.sin(beta_y2*(c-b))
            term5 = -(beta_y2/beta_y1)*np.tan(beta_y1*b)
            val = ((term1 - term2)/(term3 + term4)) - term5
            print val
            return val

        if (flag == 1):
            flag = 2
            kz_guess = (omega[i]*np.sqrt(u*e))*(1-1j*0.001)
        elif(flag == 2):
            flag = 0
            kz_guess = kz[i-1]
        else:
            kz_guess = 2*kz[i-1]-kz[i-2]

        kz[i] = newton(kz_guess,char_eq)

#-----------------------------------------
# Solve for alpha/beta
beta = np.real(kz)
alpha = -1*np.imag(kz)

# Solve for Phase Velocity
vp = np.divide(omega,np.transpose(kz))
# Solve for Group Velocity
```

```
vg = np.divide(np.diff(omega),np.transpose(np.diff(np.real(kz),axis=0)))

#-----------------------------------------
normf = omega/wc
# Plot - omega vs beta plot
plt.figure()
plt.plot(beta, normf)
plt.xlabel(r'$\beta$')
plt.ylabel(r'$\omega/\omega_c$')
plt.title(r'$\omega$ vs $\beta$ Plot')
plt.show()

# Plot - phase and group velocity plot
plt.figure()
plt.plot(normf, np.transpose(np.real(vp)/c0), label = 'Phase Velocity')
plt.plot(normf[0:-1], np.transpose(vg/c0), label = 'Group Velocity')
plt.legend(loc='best')
plt.xlabel('Normalized Frequency')
plt.xlim([1,3])
plt.ylabel('Velocity (m/s)')
plt.title('Group and Phase Velocities Plot')
plt.show()

# Plot - attenuation in dB/mm plot
alpha_new = alpha*(8.685889638)/(1000) #Np/m -> dB/mm
plt.figure()
plt.plot(normf, alpha_new)
```

```
plt.xlabel('Normalized Frequency')
plt.xlim([1,3])
plt.ylabel(r'$\alpha$')
plt.title('Attenuation in dB/mm')
plt.show()
```

# APPENDIX B

# WAVEGUIDE MATERIAL MEASUREMENT PROCEDURE

## B.1 Introduction

This appendix details how to calibrate an Agilent Technologies E5071C ENA Series Network Analyzer and subsequently measure a material sample in a waveguide for the S- and X-Band frequency ranges. Additionally, details are provided on how to prepare a suitable material sample for material measurement and the following appendices provide code and the algorithm outline on how to process these measurements to extract material parameters using a Nicholson-Ross-Weir (NRW) algorithm.

## B.2 Material Samples

For the S-Band a material block must be $2.84 \times 1.34 \times 0.7$ inches (W×H×L). The W and H fill the sample holder cross-section and the L of 0.7 in is important for transforming the S-Parameter measurements into dielectric properties values ($\epsilon_r$ and $\tan\delta$) using the NRW algorithm.

For the X-Band a material block should be $0.9 \times 0.4 \times 0.27^*$ inches (W×H×L). Again, the W and H fill the sample holder cross-section, but, here the L is not as strict. The L should be less than 1/2 wavelength (in the material) thick in this frequency range. For my work, I am expecting the samples to have a dielectric constant around 2.5-3 which yields a thickness of roughly 0.27 in. If the sample is too thick it becomes difficult to get it out of the guide, too thin, and it becomes fragile and it doesn't get much phase change during the measurement. I found doing my measurements at 0.27 in was almost the exact total length of the X-Band sample holder so I do not recommend making samples any thicker than this unless they will be measured by inserting them into the waveguide itself. Note that if this procedures is used the de-embedding will be much different than what is used here.

It is highly advised to make your material block slightly larger that the sample holder cross-section dimensions and then sand it down to size right before measurements are to be taken. This ensures it fits the holder as perfectly as possible, with, ideally, no air gaps between the material and the holder walls. This gives the most accurate results. Additionally, you want to minimize, ideally have no, cracks, roughness, air pockets, chips, or any other defects in your material sample. Defects greatly reduce the accuracy of the results. If there are any noticeable defects the sample should not be used.

## B.3 Clean the Equipment

Before connecting any connectors, use a foam swab and isopropyl alcohol (IPA) to clean out the connectors. You can refer to guides provided by Agilent on connector cleaning but you should only dampen, not soak, the swab before gently moving it around the center conductor pin. You should also visually inspect that no foreign particles (foam, dust, etc.) are in the connector and that the center pin is not bent or damaged. Next, clean the surfaces of the waveguide that get bolted together so they can make good contact. Clean out the inside of the sample holder so no residue or particles left behind from a prior sample could interfere with your measurements. Finish cleaning any connectors or waveguide segments with compressed air to get any dust or fine particles out.

## B.4 Setup the System

To setup the system for measurements you will use the Agilent Technologies E5071C ENA Series Network Analyzer and the S- or X-Band waveguide in its holder. For reference, Figure B.1 shows the X-band waveguide in its holder, in front of the VNA ready to be connected. Note: the blue static wristband should always be worn when doing work direct with or near the VNA or VNA cables.

The cables from the VNA are 3.5 mm connectors (green in the labs color system) and do not connect directly to the waveguide. As can be seen in Figure B.2, an APC-7 mm connector must be used to adapt the VNA cables to the waveguide assembly. These connectors (APC-7 mm) are genderless, it just depends on how you adjust them. All that matters for mating them is a snug

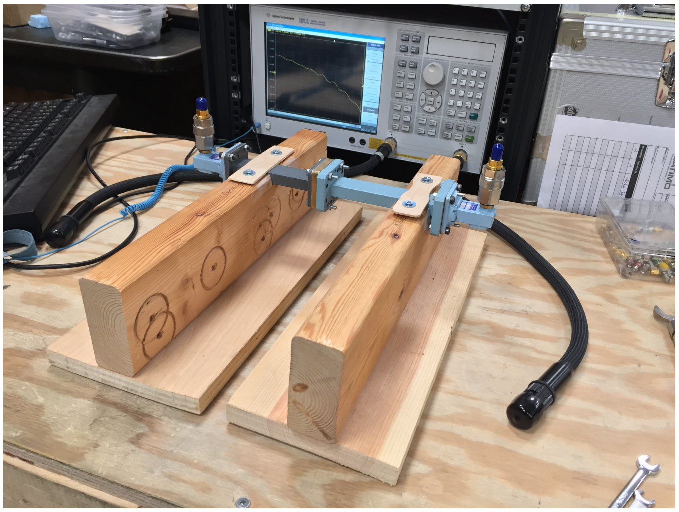

Figure B.1: X-Band waveguide in its holder placed in front of the VNA used for measurements.

connection (use torque wrench).

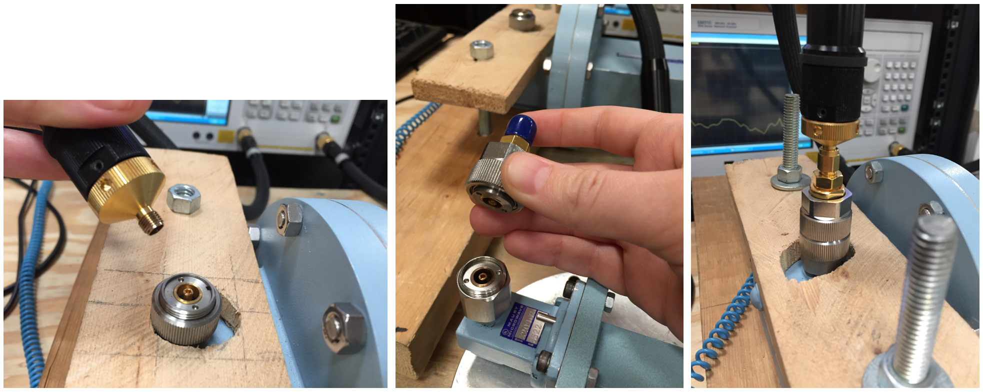

Figure B.2: Connector assembly to attach the waveguide to the VNA properly:(left) shows that the 3.5 mm VNA connection **does not** directly connect to the waveguide connector, (middle) shows the adapter, an APC-7 mm connector, to be connected to the waveguide first, and (right) shows the final connected VNA to the waveguide.

All connector matings should be properly torqued for the most accurate results. There **are** torque wrenches for the 2.4 mm/K/3.5 mm (8 in-lb), SMA (5 in-lb), and 7 mm/N (12 in-lb) connectors. Recall that in order to properly tighten a connection you should always be using **two** wrenches. One to apply torque, and the other the hold the other side (if not your torque is applied to the cable/other connectors in the system which lessens their lifetime (or damages them out right). Recall that if any adapters are needed the wrench size for the SMA/3.5 mm through is a 7/32 wrench and the SMA/3.5 mm is a 7/16 wrench (for holding). Additionally if adapters are needed and they are not clearly marked using the red/green system in the lab then the SMA and 3.5 mm male connector gauging kit should be used to determine if the adapter is suitable to be used. The kit can be seen in Figure B.3 where the center most item is the gauge. The item below it with the red cap is the calibration standard, where, when connected to the gauge, the gauge should read “0”, if not then adjust the gauge to read 0. When attaching an adapter or connector facing judgment it is ideal to be as close to the 0 mark as possible without going over. If the connector reads below 0 (in the “negative range”) it can be mated with 3.5 mm connectors (green), if it goes beyond 0 into the “positive” range it can only be used with SMA connectors (red). However if a connector reads too low, such as at or below -40 then it is unlikely to make a good connection to the 3.5 mm connector.

Figure B.3: SMA and 3.5 mm male connector gauging kit.

Also for any screw that requires torque where a specific torque wrench cannot be found here is an adjustable socket torque wrench in the lab, see Figure B.4. For example, the screws that hold the X-Band waveguide flanges together should be torqued but there is no specific wrench for them. They are 7 mm bolts with an 8.8 rating stamped on the head which means they can take a maximum torque of 2 in/lb (these values can be looked up on charts online). So the adjustable torque wrench can be used by using the 7 mm socket and adjusting the torque to 2 in/lb.

## B.5 S-Band Calibration

1. If you were not the last person to use, preset the system

Figure B.4: Adjustable socket torque wrench setup for use with the X-Band flange bolts with additional holding wrench and example bolt.

2. Scale → electrical delay → waveguide media → cut off 2.078 GHz
3. Averaging on, 64, average trigger on, IF BW 15 kHz
4. Stimulus → 2.6 - 3.95 GHz, center and span is automatic
5. Sweep setup → 801 points, stepped, else is default
6. Trigger → Single (as opposed to continuous)
7. Calibration → Cal kit S_TRL → port extension off → Zo = 1 Ω → Calibrate the 2 port TRL Cal
   - Thru: nothing in between the two sides, use all 4 alignments pins (1 on each side and top/bottom), use short screws
   - Short: polished plate, have polished side facing the port you are measuring, use medium screws
   - Line: the known line length piece, use medium screws
8. After calibration is complete hit done, then if you trigger and auto scale $S_{11}$ should be -80 to -100 dB

## B.6 X-Band Calibration

1. If you were not the last person to use, preset the system

2. Scale → electrical delay → waveguide media → cut off 6.557 GHz
3. Averaging on, 64, average trigger on, IF BW 15 kHz
4. Stimulus → 8.2 - 12.4 GHz, center and span is automatic
5. Sweep setup → 801 points, stepped, else is default
6. Calibration → Cal kit XBand-X7005M → port extension off → Zo = 1 Ω → Calibrate the 2 port cal by following the guided instructions on the screen (note that the "thru" is just the two halves connected together).
7. After calibration is complete hit done, then if you trigger and auto scale $S_{11}$ should be -80 to -100 dB
8. First measurement is the sample holder segment empty, use long screws (should be -30 to -40 dB)

## B.7 Measurements

1. Note: Once you have setup the system you want to move the VNA cables as little as possible, movements in the cables will effect your calibration and make your results less accurate
2. First measurement is the sample holder segment empty, use long screws
3. When taking material measurements you always want the material block flush with one side of the sample holder (as flat on the sample holder edge as possible) and then to take the measurement with that flat/flush side facing Port 1.
4. Take 10 measurements of each sample, the sample needs to be re-seated (taken out of the sample holder and put back in) every time for the measurement to be statistical significantly different.
5. After ≈2 hrs you will need to re-calibrate, but it is best if you re-calibrate between each sample.

## B.8 Information Processing

Use Nicholson-Ross-Weir (NRW) to extract the material samples constitutive parameters, in doing this you will need to de-embed your measurements. Further details on NRW can be found in Appendix C and MATLAB code in Appendix D.

# APPENDIX C

# NICHOLSON-ROSS-WEIR AND ITERATIVE EPSILON EXTRACTION ALGORITHMS

## C.1 Introduction

This document details the mathematical extraction process for obtaining the complex constitutive material parameters $\mu$ and $\epsilon$ from a reflection, $S_{11}$, and transmission, $S_{21}$, measurement taken using a vector network analyzer (VNA). For these measurements a material sample is placed into a waveguide of rectangular cross section as shown in Figure C.1. It is assumed that the material perfectly fills the cross-section and that the material sample has a thickness, $d$, that is less than half a wavelength of the longest wavelength within the frequency range of interest when the wave is traveling through the material (not the free space wavelength). Here, the well known Nicholson-Ross-Weir (NRW) algorithm is summarized and an implementation of NRW in MATLAB specifically as was used in the material characterization work from this thesis is provided in Appendix D.

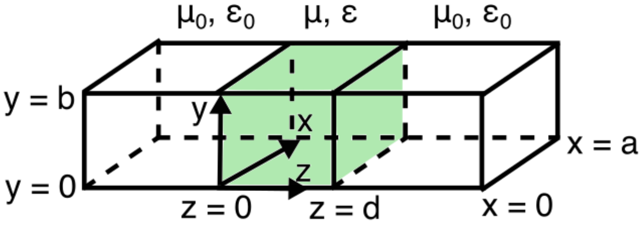

Figure C.1: Diagram of rectangular waveguide with a material sample placed in the green cross-sectional region and the attached waveguide extensions are the transparent boxes on each side.

A simplified version of NRW is also used where just a transmission measurement is needed to iteratively solve for $\epsilon$, thus called the iterative epsilon extraction (IEE) algorithm. The algorithm for IEE is provided here and the MATLAB implementation is in Appendix E.

## C.2 Nicholson-Ross-Weir (NRW) algorithm

Given the definitions:

$$V_1 = S_{21} + S_{11} \tag{C.1}$$

$$V_2 = S_{21} - S_{11} \tag{C.2}$$

where:

$$S_{11} = \frac{(1 - P^2)\Gamma}{1 - P^2\Gamma^2} \tag{C.3}$$

$$S_{21} = \frac{(1 - \Gamma^2)P}{1 - P^2\Gamma^2} \tag{C.4}$$

we can find expressions relating the measured S-parameters to the unknown constitutive parameters. Thus we have 4 knowns, from the 2 complex S-parameters in real and imaginary representation, and 4 unknowns, the 2 complex constitutive parameters $\epsilon$ and $\mu$. Continuing, I will follow the terminology from Nicholson (1970), where Equation C.3 and C.4 can be substituted into C.1 and C.2:

$$V_1 = \frac{P - \Gamma^2 P + \Gamma - P^2\Gamma}{1 - \Gamma^2 P^2} = \frac{(1 - \Gamma P)P + (1 - \Gamma P)\Gamma}{(1 + \Gamma P)(1 - \Gamma P)} = \frac{P - \Gamma}{1 + \Gamma P} \tag{C.5}$$

$$V_2 = \frac{(1 + \Gamma P)P - (1 + \Gamma P)\Gamma}{(1 + \Gamma P)(1 - \Gamma P)} = \frac{P - \Gamma}{1 - \Gamma P} \tag{C.6}$$

This allows us to solve for $P$ and then subsequently $\Gamma$ because we have simplified our system of equations into 2 equations and 2 unknowns (now $P$ and $\Gamma$). So $V_1 + V_1\Gamma P = P + \Gamma$ or $P(1 - \Gamma V_1) = V_1 - \Gamma$ leads to:

$$P = \frac{V_1 - \Gamma}{1 - \Gamma V_1} \tag{C.7}$$

Then substituting $V_2 - V_2\Gamma P = P - \Gamma$ into C.7 leads to:

$$V_2 - \Gamma\left(\frac{V_1 - \Gamma}{1 - \Gamma V_1}\right)V_2 = \frac{V_1 - \Gamma}{1 - \Gamma V_1} - \Gamma$$

$$V_2 - \Gamma V_2 V_1 - \Gamma V_1 V_2 + \Gamma^2 V_2 = V_1 - \Gamma - \Gamma + \Gamma^2 V_1$$

$$\Gamma^2(V_1 - V_2) - 2\Gamma(1 - V_1 V_2) + (V_1 - V_2) = 0$$

$$\Gamma^2 - 2X + 1 = 0$$

where:

$$X = \frac{1 - V_1 V_2}{V_1 - V_2} \tag{C.8}$$

This quadratic for $\Gamma$ has solutions:

$$\Gamma = X \pm \sqrt{X^2 - 1} \tag{C.9}$$

whose sign should be chosen based on $|\Gamma| \leq 1$.

Lastly, the expression for $\Gamma$ can be related to the constitutive parameters where:

$$\epsilon_r = \left[ \left( \frac{\beta_s}{\beta_o} \right)^2 + \left( \frac{\beta_s}{\beta_o} \right)^2 \right] \frac{\beta_e}{\beta_s} \frac{1 - \Gamma}{1 + \Gamma} \tag{C.10}$$

and

$$\mu_r = \frac{\beta_s}{\beta_e} \frac{1 + \Gamma}{1 - \Gamma} \tag{C.11}$$

where

$$\beta_e = \sqrt{\beta_o^2 - \left( \frac{\pi}{a} \right)^2} \tag{C.12}$$

$$\beta_s = \beta_o \sqrt{\epsilon_r \mu_r - \left( \frac{\pi / a}{\beta_o} \right)^2} = -\frac{\ln(P) \pm j2n\pi}{jd} \tag{C.13}$$

and $a$ is the width of the waveguide in meters, $d$ is the sample thickness in meters, and if a sample is “thin” (which is defined as being less than a half wavelength in thickness when traveling in the material) then $n = 0$. Other constants used above are defined below as:

$$\mu_o = 4\pi \times 10^{-7} \text{ H/m}$$

$$\epsilon_o = 8.85 \times 10^{-12} \text{ F/m}$$

$$\beta_o = \omega \sqrt{\mu_o \epsilon_o}$$

.

The last thing to consider in this process is that, for the calibration procedure used in Appendix B, the addition of the sample and its holder are beyond the plane of calibration. The system is calibrated at the plane $z = 0$ as shown in Figure C.1, so in order to accurately extract the constitutive parameters a small de-embedding step is needed. A thorough explanation and derivation for this can be found in [163] but if we consider $z = 0$ as our reference plane then the reflection measurement, $S_{11}$, is unchanged. The transmission measurement, however, will undergo a phase shift for the additional distance of air if the material sample does not perfectly fill the sample holder. Therefore, before using transmission measurements they should be multiplies by a factor of $e^{j\beta e(d-\delta)}$ where $\delta$ is the sample thickness and $d$ is the thickness of the sample holder. This step is also necessary for the algorithm in Section C.3.

## C.3 Iterative Epsilon Extraction (IEE) algorithm

Using just a transmission measurement $\epsilon_r$ can be solved for. Here, the superscript T denotes "theoretical" and M denotes "measured" and $\epsilon_r$ is being solved for but is initialized with a complex valued guess. The iterative process is initiated by plugging an initial guess into Equation C.14 and then using the MATLAB built in fsolve() function to minimize C.14.

$$S_{21}^{T}(\epsilon_r) - S_{21}^{M} = 0 \tag{C.14}$$

Equation C.14 calls Equations C.15 - C.18, all of which only depend on $\epsilon_r$.

$$S_{21}^{T}(\epsilon_r) = \frac{(1-\Gamma^2)P}{1-P^2\Gamma^2} = \frac{(1-\Gamma^2(\epsilon_2))P(\epsilon_r)}{1-P^2(\epsilon_r)\Gamma^2(\epsilon_r)} \tag{C.15}$$

$$\Gamma(\epsilon_r) = \frac{Z(\epsilon_r) - Z_o}{Z(\epsilon_r) + Z_o} \tag{C.16}$$

$$Z_o = \frac{\omega\mu_o}{\beta_o} \tag{C.17}$$

$$Z(\epsilon_r) = \frac{\omega\mu_o}{\beta_s} \tag{C.18}$$

Other constants not used in Section C.2 are defined below and it is assumed that the material under investigation is nonmagnetic:

$$P(\epsilon_r) = e^{-j\beta_s d}$$

$$\beta_s = \beta_o \sqrt{\epsilon_r \mu_r - \left(\frac{\pi/a}{\beta_o}\right)^2}$$

$$\mu_o = 1 + 0j = 1$$

.

# APPENDIX D

# NICHOLSON-ROSS-WEIR ALGORITHM MATLAB CODE

```
%% Needed Constants
c0 = 299792458;     % Speed of light in a vacuum (m/s)
u0 = pi*4e-7;       % Free space permeability (H/m)
e0 = 8.85e-12;      % Free space permittivity (F/m)
delta = 17.78e-3;       % S-Band sample thickness in meters
d = 29.61e-3;           % S-Band sample holder empty distance in meters
a = 72.136e-3;  % S-Band sample holder empty width in meters
%% Grab Data from S2P Files
% Syntax for SXPParse:
%[freq, data, freq_noise, data_noise, Zo] = SXPParse('filename.s2p');
% SXPParse is available on the MATLAB File Exchange as part of the
% S-Parameter toolbox here: https://tinyurl.com/kyffpul
[freq, data, ~, ~, ~] = SXPParse('file.s2p');
len = size(freq,2);
mydata = zeros(len,2);
mydata(:,1) = data(1,1,:);   % S11
mydata(:,2) = data(2,1,:);   % S21
%% Solve for beta, epsilon, mu, tand
epsilon = zeros(1,len);
mu = zeros(1,len);
tand = zeros(1,len);
ke_c = pi/a;
k0 = 2*pi*freq*sqrt(u0*e0);
lambda0 = c0./freq;
```

```
beta_e = sqrt(k0.^2 - ke_c^2);
% De-Embed S-Parameters
S11 = mydata(:,1);
S21 = mydata(:,2).*exp(1i*beta_e*(d-delta));
% Find V1 and V2
V1 = S21 + S11;
V2 = S21 - S11;
% Find Gamma: Reflection Coefficient
X = (1 - V1.*V2)./(V1-V2);
Gammap = X + sqrt(X.^2 - 1);
if abs(Gammap) <=1
    Gamma = Gammap;
else
    Gamma = X - sqrt(X.^2 - 1);
end
% Find P: Propagation Coefficient
P = (V1 - Gamma)./(1 - Gamma.*V1);
% Solve for beta_s and epsilon
n = 0;
beta_s = (log(P) + 1i*2*n*pi)./(-1i*delta);
mu(:) = ((1 + Gamma)./(1 - Gamma)).*(beta_s./beta_e);
epsilon(:) = (1./mu(:)).*((beta_s./k0).^2 + (ke_c./k0).^2);
% Sometimes might need sign change, just judge off results
tand_reg(:) = -imag(epsilon(:))./real(epsilon(:));
```

# APPENDIX E

# ITERATIVE EPSILON EXTRACTION MATLAB CODE

```
%% Needed Constants
c0 = 299792458;     % Speed of light in a vacuum (m/s)
u0 = pi*4e-7;       % Free space permeability (H/m)
e0 = 8.85e-12;      % Free space permittivity (F/m)
delta = 17.78e-3;       % S-Band sample thickness in meters
d = 29.61e-3;           % S-Band sample holder empty distance in meters
a = 72.136e-3;  % S-Band sample holder empty width in meters
%% Grab Data from S2P Files
% Syntax for SXPParse:
%[freq, data, freq_noise, data_noise, Zo] = SXPParse('filename.s2p');
% SXPParse is available on the MATLAB File Exchange as part of the
% S-Parameter toolbox here: https://tinyurl.com/kyffpul
[freq, data, ~, ~, ~] = SXPParse('file.s2p');
len = size(freq,2);
mydata = zeros(len,2);
mydata(:,1) = data(1,1,:);   % S11
mydata(:,2) = data(2,1,:);   % S21
%% Solve
epsilon = zeros(1,len);
tand = zeros(1,len);
ke_c = pi/a;
for j = 1:len
    k0 = 2*pi*freq(j)*sqrt(u0*e0);
    Z0 = (2*pi*freq(j)*u0)/k0;
```

```
    beta_e = sqrt(k0.^2 - ke_c^2);
    % Function Handles
    beta_s = @(er) sqrt(er*k0^2 - ke_c^2);
    P = @(er) exp(-1i*delta*beta_s(er));
    Z = @(er) (2*pi*freq(j)*u0)/beta_s(er);
    gamma = @(er) (Z(er) - Z0)/(Z(er) + Z0);
    S21_T = @(er) ((1-gamma(er)^2)*P(er))/(1-(P(er)^2*gamma(er)^2));
    % Solve for stuff
    er_guess = [1.8-0.0001*1i];
    S21_M = mydata(j,2).*exp(1i*beta_e*(d-delta));
    eqn = @(er) S21_T(er) - S21_M;
    S = fsolve(eqn,er_guess);
    epsilon(:) = S;
    tand(:) = -imag(S)./real(S);
end
```

# APPENDIX F

# COPPER SPUTTERING PROCEDURE

## F.1 Introduction

This Appendix details how to sputter copper on 3D plastic printed parts using a Denton Vacuum Desktop Pro Thin Film Deposition System. At the time of this writing the system can be used through Michigan State's ECE Shop. An annotated diagram of the system is shown in Figure F.1 and below detailed instructions are provided.

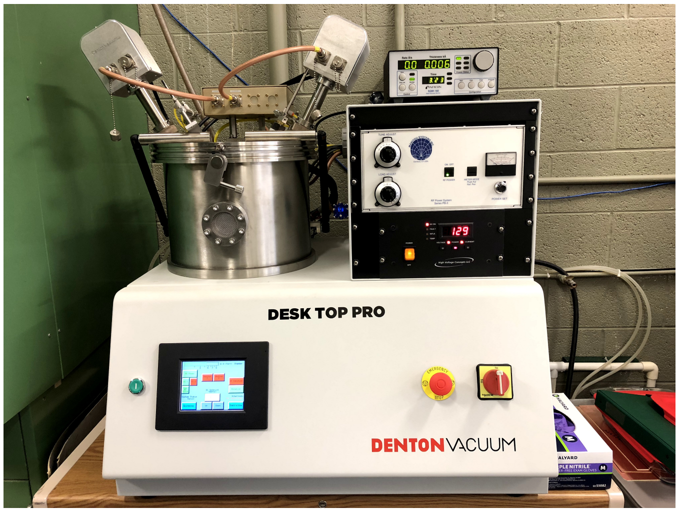

Figure F.1: Denton DesktopPro Sputtering system used for fabrication in this thesis.

## F.2 Preparation

1. Turn on the Nitrogen (open valve on Nitrogen tanks)
2. Turn on the chiller (hit enter button)
3. Turn on the Denton system (turn knob to on, push big green power button)
4. Turn power supply on (orange switch to power)
5. Press "Screens" on the Denton systems screen, then:

    a) DC Sputter Control
    b) Open Chamber
    c) Press shutter 1 and shutter 2 to check that the shutters are working the lid should be open that this time, and you should be able to see the shutter move to the aide to expose the heads that spray the vaporized metals. While the heads are exposed, you should also check that the materials loaded are the ones you want. You can tell this by color. The day we did this training, head 1 (left) was loaded with Ti (shiny gray) and head 2 (right) with Cu (shiny tan)

6. Place samples in chamber
7. Close lid, put latch on
8. On screen: auto pump vent → auto pump, wait for it to reach 5e-5 Torr. This will take 30 to 40 min, you can wait in the room while it does this (recommended) or leave and come back and check

## F.3 Sputter

1. Make an entry in the equipment log, note the pressure the chamber reaches (the one on the red screen not on the Denton Control screen)
2. Open both argon valves (silver and black)
3. Set the program: Program → Film 1 → next thru setup → program again. For more information on the programs set in the control box (blue, upper right on top of Denton System) there is a manual in the desk the Denton is sitting on.
4. On the Denton Screen: Screens → DC sputter control. Make sure the shutters on closed so we can burn off any gunk that's there from prior use.
5. Power to DC1
6. Zero on program box (controller) to time how long the run time is

7. DC ignition
8. Power on power system should agree with what's on the Denton screen. The power was 125 W during our training
9. Wait approximately 3 min to burn off any gunk on the shutters/heads. During this time you can look in the viewing window to visually inspect the color of the flame. It will be purple-ish while burning gunk, will be blue-ish white when clean. Note the time it took to burn off gunk in the log book.
10. Zero sensors, open shutter 1
11. The samples should be accumulating thickness, can see on the controller. There is something off for the Ti sensor so although we want 600 Å we'll stop it when the sensor reads 300 Å. Record in the log book how much you deposit, of what, how long it took, and the power it did it at. Depositing 600 Å of Ti should take around 6 min. You can flip through the log book and see what others did to find a reference/estimate for your work.
12. When the sensor reads 300 Å, close the shutter and hit the DC power button on the screen to turn it off.
13. Change the program to Film 2
14. Change power to DC2, make sure both shutters are closed, press zero on the controller and press DC ignition
15. It will take about 40 s to burn off the gunk copper
16. Zero the sensor again, open the shutter. This sensor is accurate so when the sensor reads 5,000 Å (what we want) it can be stopped. Note: Cu accumulates much faster than Ti.
17. We ended up opting for 10 kÅ of Cu which took 28 min, when doing this procedure with Chris Oakley, we sputtered 10 kÅ of Cu as well but did not do it all at once to get minimal warpage of our device. So we sputtered 5 kÅ, closed the shutter, turned off the power, waited

5 min, then hit DC Ignition, waited for the DC power to be green again, selected DC2 and opened shutter 2

18. Once 10 kÅ was reached, close shutter 2, turn off DC power

## F.4 Finish

1. Screens → auto pump vent → auto vent
2. When it's done venting the lid will pop off. You should then immediately turn off the argon (silver and black knobs)
3. Remove samples (wear gloves!)
4. Close the lid
5. Turn power supply off (orange switch to off)
6. Turn off the Denton system (turn large knob to off)
7. Turn off the chiller (hit power symbol button)
8. Turn off the Nitrogen (close valve on Nitrogen tank)

# APPENDIX G

# COPPER WET ETCHING PROCEDURE

## G.1 Introduction

Included here are the details on a deep copper wet etching process, developed within the Terahertz Systems Lab, as can be carried out in the Engineering Research Complex (ERC) cleanroom at Michigan State University. Using this procedure, microwave circuits can be fabricated on dielectric substrates, typically for this procedure Roger's Board was used with 17 µm thick copper.

## G.2 Pre-Cleanroom Tasks

1. Obtain a substrate. Free samples of Roger's board can be ordered from Roger's Corporation directly through their website via their "Samples in the University Program" if you use your Michigan State University email address and use your on-campus address for the shipping.
2. An additional note on selecting a substrate: Roger's boards come in a variety of dielectric constants, loss tangents, and thicknesses. But pay special attention to the thicknesses if you are planning to use the ERC cleanroom mask aligner to pattern the board as it has limitations on how thick a substrate it can accommodate. For the work published under the title "Frequency reconfigurable patch antenna array" in the journal Electronics Letters, a board thickness of 2.54 mm was used. Although it was successfully patterned it was absolutely too thick for this mask aligner and I would recommend always selecting a board thickness **thinner** than the 2.54 mm size.
3. Obtain a mask. Layouts for a design can be exported from ANSYS HFSS or Keysight's Advanced Design System (ADS) directly and be laid out in a variety of software products to be exported as a high resolution pdf. This pdf can then be printed professionally as a mask. Typically our masks have been printed by Infinity Graphics in Okemos, MI. Depending on

the type of photoresist you have available or plan to use your mask should be your design (positive photoresist) or the opposite/inverse (negative photoresist).

4. Cut your substrate into appropriately sized pieces. The mask aligner in the ERC can accommodate, at largest, a wafer size of 3 in (as in the space of a 3 in diameter circle) so the mask and board size used must be the same size or smaller than this. When unpacking the Roger's board DO NOT remove the plastic coating covering it. In the Engineering Machine Shop at Michigan State multiple bench shears are available to cleanly cut Roger's board into smaller pieces. It is possible to cut the board into smaller pieces using a paper trimmer, however, using a paper trimmer, the Roger's board is more likely to warp or deform or the cut will not be totally clean because, although the Roger's board is relatively thin and soft, a paper trimmer is not designed to cut cleanly through a material more substantial than heavy weight *paper*. One of the golden rules of proper tool safety and maintaining your equipment is to always use the right tool for the task at hand, therefore, I cannot recommend enough seeking out the shearing tools available in the Engineering Machine Shop.

## G.3 Cleanroom: prepare the substrate

1. Remove plastic coating on the Roger's board. Roger's board is shipped with a plastic coating covering it and it should not be removed until inside the cleanroom to keep the substrate as clean as possible as well as preventing any unnecessary contamination of the cleanroom itself.

2. If a ground plane is desired, completely cover one side of the board with packaging tape to protect it from the etchant.

3. Conduct the standard RCA cleaning procedure:

    a) Place sample in basket

    b) Spray and submerge the basket in a beaker with acetone for 20 s

   c) Spray and submerge the basket in a beaker with methanol for 20 s
   d) Spray and submerge the basket in a beaker with DI-water for 1 min
   e) Blow dry with $N_2$ gas
   f) Put the substrate in the oven (95 °C) for 5 min, or for 1 min at 105 °C on a hot plate, to dry off remaining moisture

## G.4 Procedure Steps

1. Spin coat samples with positive photoresist (PR), Shipley 1813 for 30 s at 4,000 rpm. This will result in a thickness of 1.2 µm of PR on the sample
2. Bake on the hot plate for 1 min (or 5 min in the oven)
3. Use the mask aligner to expose the PR, 275 W for 1.1 min
4. For standard operating procedures for the mask aligner, see the ECE Shop documentation provided here [Link]
5. Submerge in developer (MF-319) agitating continuously for 40 to 45 s
6. Spray with DI-water over a beaker for 1 min
7. Blow dry with $N_2$ gas
8. Check inside the cabinet under the wet bench across from the mask aligner for copper etchant already mixed. If there is some use it, if not make a new batch . . .
9. Mix the etchant: 700 mL of DI-water and 150 g of Sodium Persulfate ($Na_2\ O_8\ S_2$, MG Chemicals)
10. Etch:
    a) Heat up etchant on the hot plate in the wet bench nearest the mask aligner to 80 °C, measure with thermometer to 45 °C

   b) Immerse the substrate into the bath
   c) Let the substrate etch for about 45 s then immediately spray with DI-Water, then $N_2$ gas to dry it off
   d) For this mixture of etchant at this temperature the etch rate is about 3.2 µm per min so adjust the time as needed

11. Inspect under a microscope, etch more if needed
12. Spray with acetone to remove PR
13. Rinse with methanol, then DI-Water, then blow dry with $N_2$ gas

# APPENDIX H

# OPERATING THE PARKER MOTORIZED STAGE

## H.1 Introduction

This document gives step by step instructions on how to use the Parker Motorized XY Stage in the Terahertz System Lab as in Figure H.1.

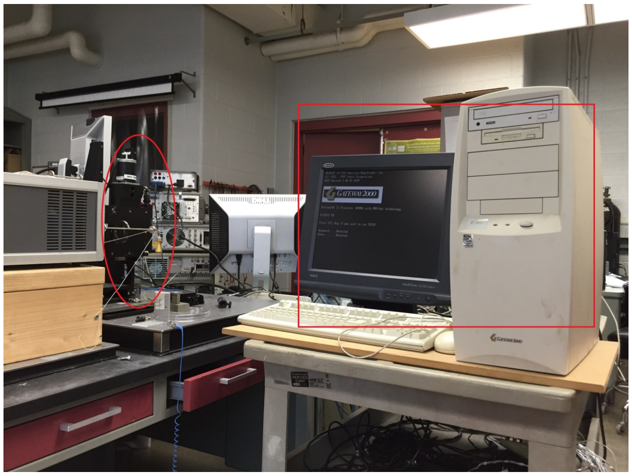

Figure H.1: Parker Motorized XY Stage in the Terahertz System Lab.

The stage is run using a Parker Compumotor AT6400 4-axis indexer from the Parker Positioning System Daedal Division. The stage is controlled by software installed on a desktop tower running Windows ME. The tower is old and slow but as long as it is used gently and patiently it is still perfectly operable.

## H.2 Procedure

1. Open up the CompuControl program to manually move the XY Stage. There is an icon on the desktop and a button on the taskbar. It should look as seen in Figure H.2.
2. First go to Motor → Motor Tools. You should see the pop-up screen in Figure H.3 and then click, in this order:

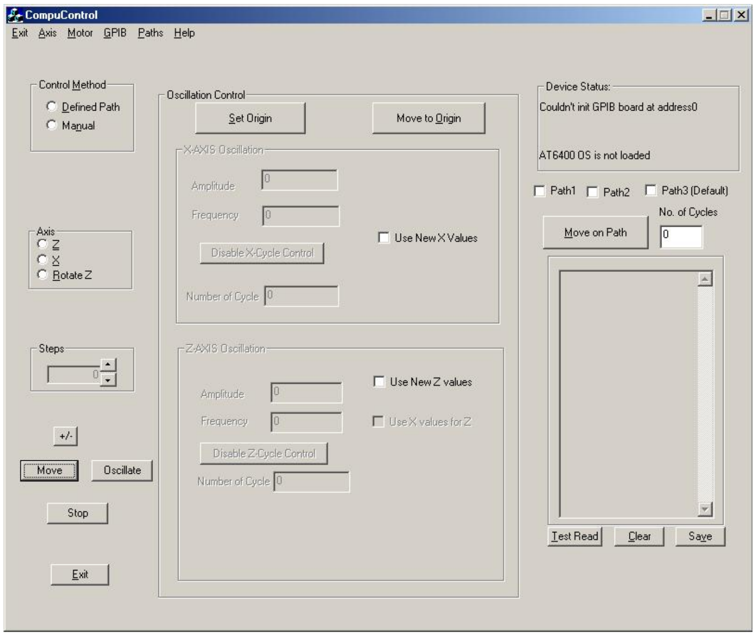

Couldn't init GPIB board at address0

AT6400 OS is not loaded

Figure H.2: CompuControl program.

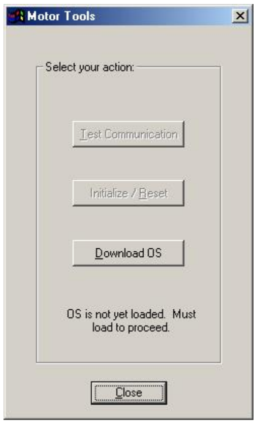

OS is not yet loaded. Must load to proceed.

Figure H.3: Motor Tools pop-up.

a) Test Communication

b) Initialize/Reset → OK

c) Download OS

3. After clicking the Download OS button Select AT6400.OPS from the pop-up file navigator window as shown in Figure H.4.

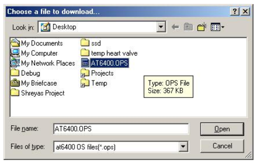

Choose a file to download...

Look in: Desktop

File name: AT6400.OPS

Files of type: at6400 OS files(*.ops)

Figure H.4: Download OS pop-up.

4. Once the system had loaded you'll see the pop-up in Figure H.5 and then click OK.

AT6400 OS Loader

Operating System is Loaded.

Figure H.5: AT6400 OS loader pop-up.

5. Now you can manually move the XY Stage. As noted by the colored boxes on the Compu-Control Screen below all you need to do is:
   a) Select "Manual" for your "Control Method"
   b) Select an axis to move, the Z axis will move the stage vertically and the X axis will move the stage horizontally.
   c) Select the number of steps to move, in the manual setting each step is 1 mm. 1 mm is NOT the smallest step size it is just what is programmed into the manual movement program (previous users have reported programming steps as small as 100 µm).
   d) Select a direction of movement, the button denoted by the green box will change the direction, by default the direction is +. For reference on direction see the diagram in Figure H.6.

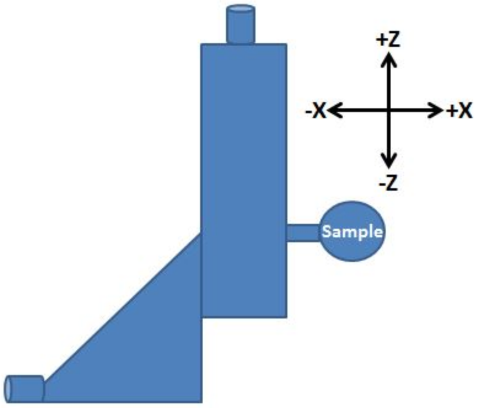

Figure H.6: Motion direction reference.

e) Press “Move” as seen in Figure H.7.

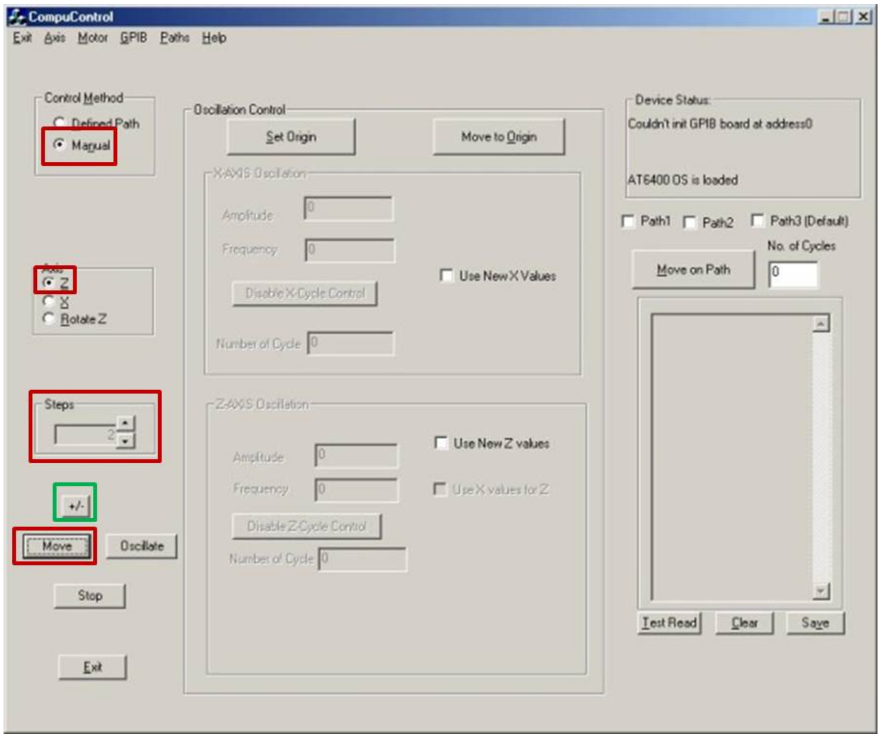

Control Method
○ Defined Path
● Manual

Axis
● Z
○ X
○ Rotate Z

Steps: 2

No. of Cycles: 0

Device Status:
Couldn't init GPIB board at address0

AT6400 OS is loaded

Figure H.7: CompuControl screen annotated.

6. It is a good idea to manually move the stage to a “Home” position, like either the bottom most or top most point on your sample.

7. Next, open up the “Motion Architect Program” by clicking on the icon on the desktop. This program has an editor program where you can create a new or modify an existing program and a terminal program where you can execute a program. When you open the program you should see the screen in Figure H.8.

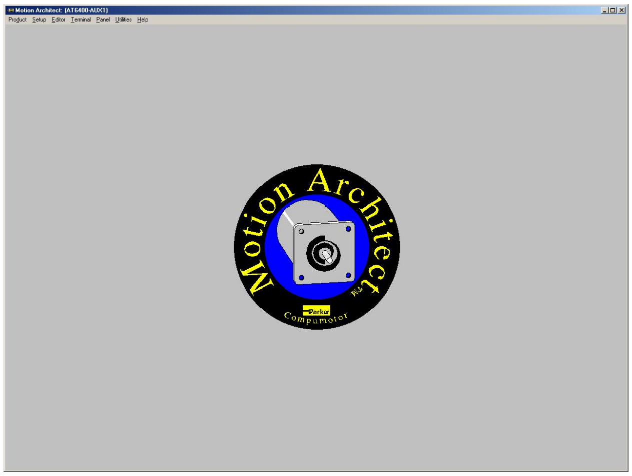

Figure H.8: Motion Architect screen.

8. First open up the editor program from the “Editor” item on the menu bar. You should see the screen in Figure H.9.

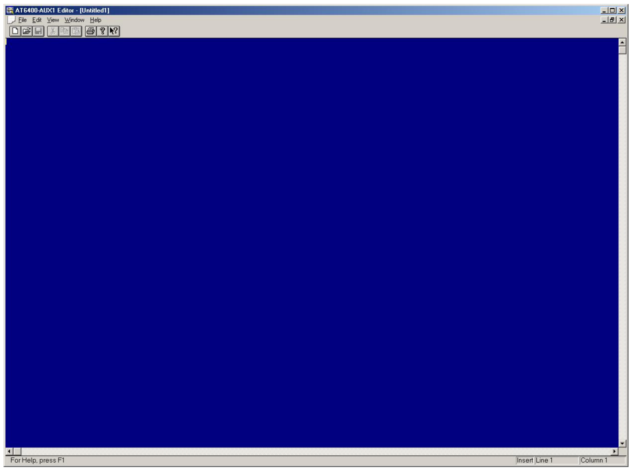

Figure H.9: Motion Architect editor screen.

9. Then go to open a program and you should see the pop-up in Figure H.10.

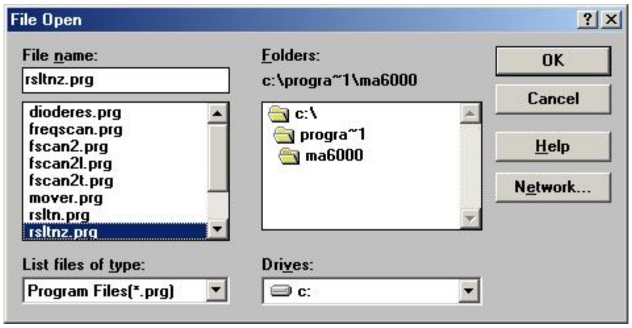

File name: rsltnz.prg

Folders: c:\progra~1\ma6000

List files of type: Program Files(*.prg)

Drives: c:

Figure H.10: Motion Architect editor open pop-up.

10. The rstlnz.prg program does a vertical scan (by moving downward), the rsltn.prg program does a horizontal scan (moving inwards) and the fscan2.prg program does an XY scan. The motion across a sample of these programs is shown in Figure H.11.

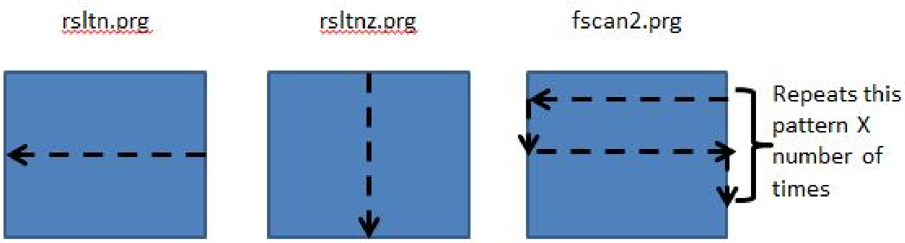

Figure H.11: Illustration of different programs scanning patterns.

11. Once you've opened a program you want to modify you should see it open in the editor window as seen in Figure H.12. If you want to use or modify one of the original programs mentioned above you should *keep a copy of the original*. That way there is always a working version to fall back on as this program does not have built in version control.

12. Once you're ready to run a program, open up the "Terminal" from the top menu bar and go to Transfers → Send Motion Program, as shown in Figure H.13.

13. Select a program to run and click OK, as seen in Figure H.14.

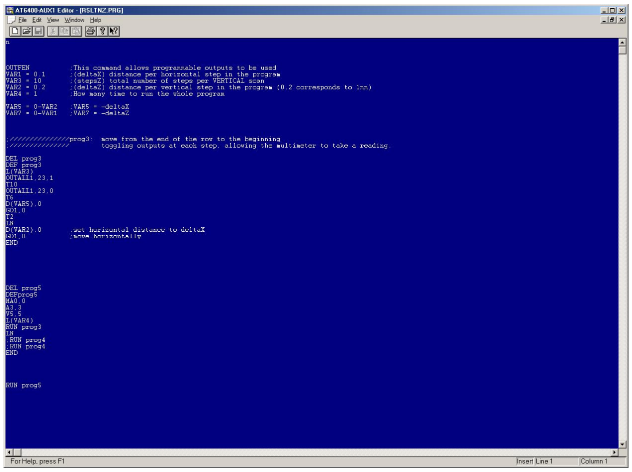

```
n



OUTFEN          ;This command allows programmable outputs to be used
VAR1 = 0.1      ;(deltaX) distance per horizontal step in the program
VAR3 = 10       ;(stepsZ) total number of steps per VERTICAL scan
VAR2 = 0.2      ;(deltaZ) distance per vertical step in the program (0.2 corresponds to 1mm)
VAR4 = 1        ;How many time to run the whole program

VAR5 = 0-VAR2   ;VAR5 = -deltaX
VAR7 = 0-VAR1   ;VAR7 = -deltaZ



;////////////////prog3:  move from the end of the row to the beginning
;////////////////        toggling outputs at each step, allowing the multimeter to take a reading.

DEL prog3
DEF prog3
L(VAR3)
OUTALL1,23,1
T10
OUTALL1,23,0
T6
D(VAR5),0
GO1,0
T2
LN
D(VAR2),0       ;set horizontal distance to deltaX
GO1,0           ;move horizontally
END






DEL prog5
DEFprog5
MA0,0
A3,3
V5,5
L(VAR4)
RUN prog3
LN
;RUN prog4
;RUN prog4
END




RUN prog5
```

Figure H.12: Motion Architect editor screen with a program loaded to edit.

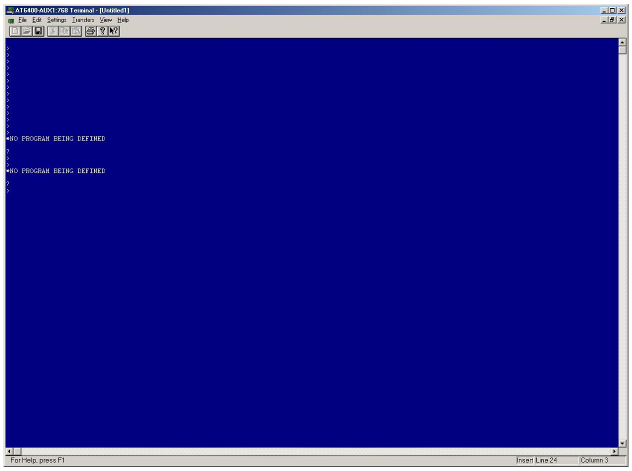

```
>
>
>
>
>
>
>
>
>
>
>
>
>
>
*NO PROGRAM BEING DEFINED

?
>
>
*NO PROGRAM BEING DEFINED

?
>
```

Figure H.13: Terminal screen.

14. You will then see a window to abort the operation as it's running which will go away once it has stopped running, as seen in Figure H.15. If you hear a clicking from the stepper motors then they have reached their maximum position and you should abort the program in order to not damage them. Make sure when you originally home the stage to a position on your sample that you do so in a way that leaves lots of room for the motors to run you program.

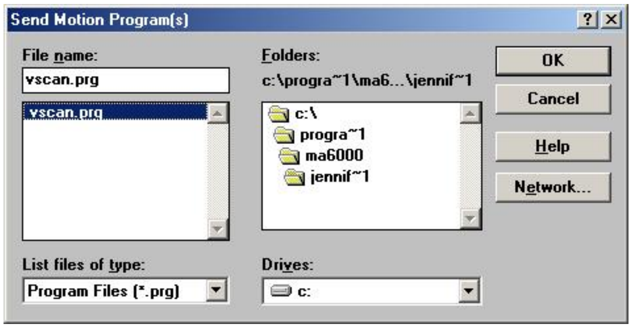

Send Motion Program(s)

File name: vscan.prg

Folders: c:\progra~1\ma6...\jennif~1

List files of type: Program Files (*.prg)

Drives: c:

Figure H.14: Send motion program pop-up.

Sending Motion Program(s)

Filename: C:\PROGRA~1\MA6000\JENNIF~1\VSCAN.PRG

Waiting for 6000 command processing...

Figure H.15: Send motion program pop-up abort option.

## H.3 Modifying Programs

In the event something happens to the original programs saved on the computer system that controls the motorized stage an annotated code can be found in Appendix I which could be used and easily modified by a novice the use the stage.

# APPENDIX I

# PARKER MOTORIZED STAGE CODE

```
OUTFEN          ;This command allows programmable outputs to be used
VAR1 = −0.6     ;(deltaZ) distance per vertical step in the program
VAR3 = 2        ;(stepsX) total number of steps per HORIZONTAL
VAR2 = −0.6     ;(deltaX) distance per horizontal step in the program
   (0.2 corresponds to 1mm)
VAR4 = 1                ;How many time to run the whole program

VAR5 = 0−VAR2           ;VAR5 = −deltaX
VAR7 = 0−VAR1           ;VAR7 = −deltaZ

;///////////////prog1: Move to the next row (vertical move)
DEL prog1       ;deletes any existing program 1
DEF prog1       ;defines prog1 from here to END
;T1             ;wait one second, previously was four seconds
D(VAR1)         ;set vertical distance to deltaZ
GO1             ;move the vertical axis deltaZ
T1              ;wait one second, previously was four seconds
END

;///////////////prog2: move from the beginning of the row to the end,
;///////////////toggling outputs at each step, allowing the multimeter to
    take a reading.
DEL prog2
DEF prog2
```

```
MA0,0           ;set both axes in relative mode
L(VAR3)         ;repeat the following stepsX times
OUTALL1,23,1    ;set programmable outputs 1–24 to 1 (low)
T2              ;wait 2 seconds, previously was 4 seconds
OUTALL1,23,0    ;set programmable outputs 1–24 to 0 (high)
T1              ;wait 1 seconds, previously was 2 seconds
D0,(VAR2)       ;set horizontal distance to deltaX
GO0,1           ;move horizontally
T1              ;wait one seconds
LN              ;end loop
OUTALL1,23,1
T2
OUTALL1,23,0
T1
;///D0,(VAR5)           ;Step back to rest on last point data was taken
;//GO0,1
END

;//////////////prog3: move from the end of the row to the beginning
;//////////////toggling outputs at each step, allowing the multimeter to take a reading.
DEL prog3
DEF prog3
L(VAR3)
OUTALL1,23,1
T2
OUTALL1,23,0
```

```
T1
D0,(VAR5)
GO0,1
T1
LN
OUTALL1,23,1
T2
OUTALL1,23,0
T1
;///D0,(VAR2)           ;set horizontal distance to deltaX
;//GO0,1                ;move horizontally
END

;///////////////prog4: after scan is completed, move −deltaZ∗stepsZ (back to beginning)
DEL prog4
DEFprog4
L(VAR4)
D0,(VAR7)               ;set vertical distance to −deltaZ
GO0,1
LN
END

DEL prog5
DEFprog5
MA0,0
A3,3
```

```
V5,5
L(VAR4)
T1              ;wait one second
RUN prog2
RUN prog1
RUN prog3
RUN prog1
LN
RUN prog2
;RUN prog4
;RUN prog4
END

RUN prog5
```

# BIBLIOGRAPHY

# BIBLIOGRAPHY

[1] E. Corporation, “MODEL PB7200 THz Frequency Domain Spectrometer,” Emcore Corporation, Tech. Rep., 2013.

[2] S. Ltd., “10 Reasons Why Multi-Material 3D Printing is Better for your Product Design and Development,” Stratasys, Tech. Rep., Date-Accessed = 10/1/2018. [Online]. Available: usglobalimages.stratasys.com

[3] E. V. Loewenstein, “The history and current status of fourier transform spectroscopy,” Applied Optics, vol. 5, no. 5, pp. 845–854, 1966.

[4] J. Connes and P. Connes, “Near-infrared planetary spectra by fourier spectroscopy. i. instruments and results,” JOSA, vol. 56, no. 7, pp. 896–910, 1966.

[5] M. Van Exter, C. Fattinger, and D. Grischkowsky, “Terahertz time-domain spectroscopy of water vapor,” Optics letters, vol. 14, no. 20, pp. 1128–1130, 1989.

[6] P. Jepsen, D. Cooke, and M. Koch, “Terahertz spectroscopy and imaging - Modern techniques and applications,” Laser & Photonics Reviews, vol. 5, no. 1, pp. 124–166, jan 2011.

[7] S. L. Dexheimer, Terahertz spectroscopy: principles and applications. CRC press, 2007.

[8] M. Tonouchi, “Cutting-edge terahertz technology,” Nature Photonics, vol. 1, no. 2, pp. 97–105, 2007.

[9] A. G. Davies, A. D. Burnett, W. Fan, E. H. Linfield, and J. E. Cunningham, “Terahertz spectroscopy of explosives and drugs,” Materials today, vol. 11, no. 3, pp. 18–26, 2008.

[10] B. Fischer, M. Walther, and P. U. Jepsen, “Far-infrared vibrational modes of dna components studied by terahertz time-domain spectroscopy,” Physics in Medicine & Biology, vol. 47, no. 21, p. 3807, 2002.

[11] K. Fukunaga and M. Picollo, “Terahertz spectroscopy applied to the analysis of artists’ materials,” Applied Physics A, vol. 100, no. 3, pp. 591–597, 2010.

[12] K. Fukunaga, Y. Ogawa, S. Hayashi, and I. Hosako, “Terahertz spectroscopy for art conservation,” IEICE Electronics Express, vol. 4, no. 8, pp. 258–263, 2007.

[13] C. D. Benzant, “Applications of THz pulses in semiconductor relaxation and biomedical imaging studies,” Ph.D. dissertation, University of Nottingham, 2000.

[14] D. B. Bennett, W. Li, Z. D. Taylor, W. S. Grundfest, and E. R. Brown, “Stratified Media Model for Terahertz Reflectometry of the Skin,” IEEE Sensors Journal, vol. 11, no. 5, pp. 1253–1262, may 2011.

[15] C. Y. Tan, B. Statham, R. Marks, and P. a. Payne, "Skin thickness measurement by pulsed ultrasound: its reproducibility, validation and variability." The British Journal of Dermatology, vol. 106, no. 6, pp. 657–667, 1982.

[16] J. T. Whitton and J. D. Everall, "The thickness of the epidermis," The British Journal of Dermatology, vol. 89, no. 5, pp. 467–476, 1973.

[17] E. Pickwell and V. P. Wallace, "TOPICAL REVIEW: Biomedical applications of terahertz technology," Journal of Physics D: Applied Physics, vol. 39, no. 17, pp. R301–R310, sep 2006.

[18] A. J. Fitzgerald, V. P. Wallace, M. Jimenez-linan, L. Bobrow, R. J. Pye, and A. D. Purushotham, "Terahertz Pulsed Imaging of Human Breast Tumors," Radiology, vol. 239, no. 2, pp. 533–540, 2006.

[19] P. C. Ashworth, E. Pickwell-MacPherson, E. Provenzano, S. E. Pinder, A. D. Purushotham, M. Pepper, and V. P. Wallace, "Terahertz pulsed spectroscopy of freshly excised human breast cancer," Optics Express, vol. 17, no. 15, p. 12444, jul 2009.

[20] R. M. Woodward, V. P. Wallace, R. J. Pye, B. E. Cole, D. D. Arnone, E. H. Linfield, and M. Pepper, "Terahertz pulse imaging of ex vivo basal cell carcinoma," Journal of Investigative Dermatology, vol. 120, no. 1, pp. 72–78, 2003.

[21] V. P. Wallace, P. F. Taday, A. J. Fitzgerald, R. M. Woodward, J. Cluff, R. J. Pye, and D. D. Arnone, "Terahertz pulsed imaging and spectroscopy for biomedical and pharmaceutical applications." Faraday Discussions, vol. 126, pp. 255–263, 2004.

[22] C. S. Joseph, R. Patel, V. a. Neel, R. H. Giles, and A. N. Yaroslavsky, "Imaging of ex vivo nonmelanoma skin cancers in the optical and terahertz spectral regions optical and terahertz skin cancers imaging." Journal of Biophotonics, vol. 7, no. 5, pp. 295–303, may 2014.

[23] R. M. Woodward, B. E. Cole, V. P. Wallace, R. J. Pye, D. D. Arnone, E. H. Linfield, and M. Pepper, "Terahertz pulse imaging in reflection geometry of human skin cancer and skin tissue," Physics in Medicine and Biology, vol. 47, no. 21, pp. 3853–3863, nov 2002.

[24] K. W. Kim, K.-S. Kim, H. Kim, S. H. Lee, J.-H. Park, J.-H. Han, S.-H. Seok, J. Park, Y. Choi, Y. I. Kim, J. K. Han, and J.-H. Son, "Terahertz dynamic imaging of skin drug absorption." Optics Express, vol. 20, no. 9, pp. 9476–9484, apr 2012.

[25] Z. D. Taylor, R. S. Singh, M. O. Culjat, J. Y. Suen, W. S. Grundfest, H. Lee, and E. R. Brown, "Reflective terahertz imaging of porcine skin burns," Optics Letters, vol. 33, no. 11, p. 1258, may 2008.

[26] S. Y. Huang, E. Macpherson, and Y. T. Zhang, "A Feasibility Study of Burn Wound Depth Assessment Using Terahertz Pulsed Imaging," in Medical Devices and Biosensors, 2007. ISSS-MDBS 2007. 4th IEEE/EMBS International Summer School and Symposium on, 2007, pp. 132–135.

[27] M. H. Arbab, T. C. Dickey, D. P. Winebrenner, A. Chen, M. B. Klein, and P. D. Mourad, "Terahertz reflectometry of burn wounds in a rat model." Biomedical optics express, vol. 2, no. 8, pp. 2339–47, aug 2011.

[28] E. Pickwell, B. E. Cole, A. J. Fitzgerald, V. P. Wallace, and M. Pepper, "Simulation of terahertz pulse propagation in biological systems," Applied Physics Letters, vol. 84, no. 12, pp. 2190–2192, 2004.

[29] S. Nashima, O. Morikawa, K. Takata, and M. Hangyo, "Temperature dependence of optical and electronic properties of moderately doped silicon at terahertz frequencies," Journal of applied physics, vol. 90, no. 2, pp. 837–842, 2001.

[30] J. A. Hejase, P. R. Paladhi, and P. Chahal, "Terahertz characterization of dielectric substrates for component design and nondestructive evaluation of packages," IEEE Transactions on Components, Packaging and Manufacturing Technology, vol. 1, no. 11, pp. 1685–1694, 2011.

[31] C. D. Stoik, M. J. Bohn, and J. L. Blackshire, "Nondestructive evaluation of aircraft composites using transmissive terahertz time domain spectroscopy," Optics express, vol. 16, no. 21, pp. 17 039–17 051, 2008.

[32] C. Stoik, M. Bohn, and J. Blackshire, "Nondestructive evaluation of aircraft composites using reflective terahertz time domain spectroscopy," Ndt & E International, vol. 43, no. 2, pp. 106–115, 2010.

[33] Y. L. Hor, J. F. Federici, and R. L. Wample, "Nondestructive evaluation of cork enclosures using terahertz/millimeter wave spectroscopy and imaging," Applied Optics, vol. 47, no. 1, pp. 72–78, 2008.

[34] D. Zimdars, J. Valdmanis, J. S. White, G. Stuk, S. Williamson, W. P. Winfree, and E. I. Madaras, "Technology and applications of terahertz imaging non-destructive examination: inspection of space shuttle sprayed on foam insulation," in AIP Conference Proceedings, vol. 760. AIP, 2005, pp. 570–577.

[35] Y.-C. Shen and P. F. Taday, "Development and application of terahertz pulsed imaging for nondestructive inspection of pharmaceutical tablet," IEEE Journal of Selected Topics in Quantum Electronics, vol. 14, no. 2, pp. 407–415, 2008.

[36] C. Jördens and M. Koch, "Detection of foreign bodies in chocolate with pulsed terahertz spectroscopy," Optical Engineering, vol. 47, no. 3, p. 037003, 2008.

[37] T. Nagatsuma, S. Horiguchi, Y. Minamikata, Y. Yoshimizu, S. Hisatake, S. Kuwano, N. Yoshimoto, J. Terada, and H. Takahashi, "Terahertz wireless communications based on photonics technologies," Opt. Express, vol. 21, no. 20, pp. 23 736–23 747, Oct 2013.

[38] A. Kanno, T. Kuri, I. Morohashi, I. Hosako, T. Kawanishi, Y. Yoshida, and K.-i. Kitayama, "Coherent terahertz wireless signal transmission using advanced optical fiber communication technology," Journal of Infrared, Millimeter, and Terahertz Waves, vol. 36, no. 2, pp. 180–197, 2015.

[39] I. A. Ibraheem, N. Krumbholz, D. Mittleman, and M. Koch, "Low-dispersive dielectric mirrors for future wireless terahertz communication systems," IEEE microwave and wireless components letters, vol. 18, no. 1, pp. 67–69, 2008.

[40] E. Seok, D. Shim, C. Mao, R. Han, S. Sankaran, C. Cao, W. Knap et al., "Progress and challenges towards terahertz cmos integrated circuits," IEEE Journal of Solid-State Circuits, vol. 45, no. 8, pp. 1554–1564, 2010.

[41] S. Boppel, A. Lisauskas, M. Mundt, D. Seliuta, L. Minkevicius, I. Kasalynas, G. Valusis, M. Mittendorff, S. Winnerl, V. Krozer et al., "Cmos integrated antenna-coupled field-effect transistors for the detection of radiation from 0.2 to 4.3 thz," IEEE Transactions on Microwave Theory and Techniques, vol. 60, no. 12, pp. 3834–3843, 2012.

[42] P. Chen, G. a. Blake, M. C. Gaidis, E. R. Brown, K. a. McIntosh, S. Y. Chou, M. I. Nathan, and F. Williamson, "Spectroscopic applications and frequency locking of THz photomixing with distributed-Bragg-reflector diode lasers in low-temperature-grown GaAs," Applied Physics Letters, vol. 71, no. 12, p. 1601, 1997.

[43] J. B. Baxter and G. W. Guglietta, "Terahertz Spectroscopy," Analytical Chemistry, vol. 83, no. 12, pp. 4342–4368, 2011.

[44] CTIA, "CTIA's Wireless Industry Survey," Cellular Telecommunications and Internet Association, Tech. Rep., 2017. [Online]. Available: www.ctia.org

[45] ——, "Wireless Snapshot 2017," Cellular Telecommunications and Internet Association, Tech. Rep., 2017. [Online]. Available: www.ctia.org

[46] D. R. Stauffer and D. Ph, "Overview of the Common Electrical Interface ( CEI ) Specification for Next Generation 25 Gb / s Serial Interfaces," Forum American Bar Association, pp. 23–25, 2012.

[47] T. Eckart, H.-J. Gotz, T. Ziselsberger, and K.-H. Otto, "The Migration of the Optical Internetworking Forum Common Electrical Interface Standardization to Optical Intra-System Interconnects Beyond 25 Gb/s," Bell Labs Technical Journal, vol. 18, no. 3, pp. 267–283, 2013.

[48] D. Porchivina, "OIF Launches CEI-112G Project for 100G Serial Electrical Links," aug 2016. [Online]. Available: http://www.businesswire.com/news/home/20160830005339/en/OIF-Launches-CEI-112G-Project-100G-Serial-Electrical

[49] Y. Zheng, Z. He, Y. Gao, and J. Liu, "Direct desktop Printed-Circuits-on-Paper flexible electronics." Scientific reports, vol. 3, p. 1786, 2013.

[50] J. H. Lee, I. Shubin, J. Yao, J. Bickford, Y. Luo, S. Lin, S. S. Djordjevic, H. D. Thacker, J. E. Cunningham, K. Raj, X. Zheng, and A. V. Krishnamoorthy, "High power and widely tunable Si hybrid external-cavity laser for power efficient Si photonics WDM links," Optics Express, vol. 22, no. 7, p. 7678, 2014.

[51] S. Rumley, D. Nikolova, R. Hendry, Q. Li, D. Calhoun, and K. Bergman, “Silicon Photonics for Exascale Systems,” Journal of Lightwave Technology, vol. 33, no. 3, pp. 547–562, 2015.

[52] D. L. Butler, M. J. Li, S. Li, K. I. Matthews, V. N. Nazarov, A. Koklyushkin, R. L. McCollum, Y. Geng, and J. P. Luther, “Multicore optical fiber and connectors for high bandwidth density, short reach optical links,” 2013 Optical Interconnects Conference, OI 2013, vol. 2, pp. 9–10, 2013.

[53] K. Szczerba, P. Westbergh, M. Karlsson, P. A. Andrekson, and A. Larsson, “70 Gbps 4-PAM and 56 Gbps 8-PAM using an 850 nm VCSEL,” Journal of Lightwave Technology, vol. 33, no. 7, pp. 1395–1401, 2015.

[54] D. M. Kuchta, C. L. Schow, A. V. Rylyakov, J. E. Proesel, F. E. Doany, and C. Baks, “A 56.1Gb/s NRZ Modulated 850nm VCSEL-Based Optical Link,” in IEEE Optical Fiber Communication Conference and Exposition and the National Fiber Optic Engineers Conference (OFC/NFOEC), 2013.

[55] N. Ophir, C. Mineo, D. Mountain, and K. Bergman, “Silicon photonic microring links for high-bandwidth-density, low-power chip I/O,” IEEE Micro, vol. 33, no. 1, pp. 54–67, 2013.

[56] T. S. Wang, K. S. Choi, H. S. Jang, A. W. Morales, and S. J. Ko, “Enhanced frame rate up-conversion method for UHD video,” IEEE Transactions on Consumer Electronics, vol. 56, no. 2, pp. 1108–1114, 2010.

[57] W. Zhu, A. Agrawal, and A. Nahata, “Planar plasmonic terahertz guided-wave devices.” Optics express, vol. 16, no. 9, pp. 6216–6226, 2008.

[58] G. Gallot, S. P. Jamison, R. W. McGowan, and D. Grischkowsky, “Terahertz waveguides,” Journal Of The Optical Society Of America B Optical Physics, vol. 17, no. 5, pp. 851–863, 2000.

[59] R. Mendis and D. Grischkowsky, “Plastic ribbon THz waveguides,” Journal of Applied Physics, vol. 88, no. 2000, pp. 4449–4451, 2000.

[60] K. Y. Park, N. Wiwatcharagoses, and P. Chahal, “Plastic injection micromachining of millimeter and sub-millimeter rectangular waveguide filters,” IRMMW-THz 2011 - 36th International Conference on Infrared, Millimeter, and Terahertz Waves, pp. 11–12, 2011.

[61] X. Yang and P. P. Chahal, “On-wafer terahertz ribbon waveguides using polymer-ceramic nanocomposites,” IEEE Transactions on Components, Packaging and Manufacturing Technology, vol. 5, no. 2, pp. 245–255, 2015.

[62] C. Yeh, F. Shimabukuro, and P. H. Siegel, “Low-loss terahertz ribbon waveguides.” Applied optics, vol. 44, no. 28, pp. 5937–5946, 2005.

[63] P. L. Kirby, D. Pukala, H. Manohara, I. Mehdi, and J. Papapolymerou, “Characterization of Micromachined Silicon Rectangular Waveguide at 400 GHz,” Components, vol. 16, no. 6, pp. 366–368, 2006.

[64] P. Doradla, C. S. Joseph, J. Kumar, and R. H. Giles, "Characterization of bending loss in hollow flexible terahertz waveguides," Optics Express, vol. 20, no. 17, p. 19176, 2012.

[65] B. M. A. Rahman, A. Quadir, H. Tanvir, and K. T. V. Grattan, "Characterization of Plasmonic Modes in a Low-Loss Dielectric-Coated Hollow Core Rectangular Waveguide at Terahertz Frequency," IEEE Photonics Journal, vol. 3, no. 6, pp. 1054–1066, 2011.

[66] J. A. Byford, Z. Purtill, and P. Chahal, "Fabrication of Terahertz Components using 3D Printed Templates," in Electronic Components and Technology Conference (ECTC) , 2016 IEEE 66th, 2016.

[67] C. Yeh, F. I. Shimabukuro, and J. Chu, "Ultralow loss dielectric ribbon waveguide for millimeter/submillimeter waves," Applied Physics Letters, vol. 54, no. 12, pp. 1183–1185, 1989.

[68] E. G. Neumann and H. D. Rudolph, "Radiation from Bends in Dielectric Rod Transmission Lines," IEEE Transactions on Microwave Theory and Techniques, vol. 23, no. 1, pp. 142–149, 1975.

[69] J. Castro, E. A. Rojas-Nastrucci, A. Ross, T. M. Weller, and J. Wang, "Fabrication , Modeling , and Application of Ceramic- Thermoplastic Composites for Fused Deposition Modeling of Microwave Components," IEEE Transactions on Microwave Theory and Techniques, 2017.

[70] J. A. Byford and P. Chahal, "Ultra-Wideband Hybrid Substrate Integrated Ribbon Waveguides Using 3D Printing," in IEEE International Microwave Symposium, San Francisco, CA, 2016, pp. 3–6.

[71] ——, "Broad-band dielectric probes for on-wafer characterization of terahertz devices," in 2018 IEEE 68th Electronic Components and Technology Conference (ECTC). IEEE, 2018, pp. 2367–2373.

[72] J. Coonrod, "Circuit Materials and High-Frequency Losses of PCBs," The PCB Magazine, 2012.

[73] R. Harrington, Time-Harmonic Electromagnetic Fields. John Wiley & Sons, 2001.

[74] E. J. Rothwell, "A study of slow-wave propagation in a lossy dielectric/ferrite-lined waveguide," Ph.D. dissertation, Stanford University, 1982.

[75] E. J. Rothwell and L. L. Frasch, "Propagation Characteristics of Dielectric Rod-Loaded Waveguides," IEEE Transactions on Microwave Theory and Techniques, vol. 36, no. 3, pp. 594–600, 2013.

[76] K. A. Zaki and A. E. Atia, "Modes in Dielectric-Loaded Waveguides and Resonators," IEEE Transactions on Microwave Theory and Techniques, vol. 31, no. 12, pp. 1039–1045, 1983.

[77] L. G. Chambers, "Propagation in waveguides filled longitudinally with two or more dielectrics," British Journal of Applied Physics, vol. 4, no. February, 1953.

[78] S. Chatterjee and R. Chatterjee, "Dielectric Loaded Waveguides - A review of Theoretical Solutions," Radio and Electronic Engineer, vol. 30, no. 4, pp. 195–205, 1965.

[79] ——, "Dielectric Loaded Waveguides - A review of Theoretical Solutions," Radio and Electronic Engineer, vol. 30, no. 4, pp. 195–205, 1965.

[80] L. Xiao, W. Gai, and X. Sun, "Field analysis of a dielectric-loaded rectangular waveguide accelerating structure," Physical Review E - Statistical, Nonlinear, and Soft Matter Physics, vol. 65, no. 1, pp. 1–9, 2002.

[81] C. Yeh, F. I. Shimabukuro, and J. Chu, "Dielectric Ribbon Waveguide: An Optimum Configuration for Ultra-Low-Low-Loss Millimeter / Submillimeter Dielectric Waveguide," IEEE Transactions on Microwave Theory and Techniques, vol. 38, no. 6, pp. 691–702, 1990.

[82] K. Wu, D. Deslandes, and Y. Cassivi, "The substrate integrated circuits-a new concept for high-frequency electronics and optoelectronics," in Telecommunications in Modern Satellite, Cable and Broadcasting Service, 2003. TELSIKS 2003. 6th International Conference on, vol. 1. IEEE, 2003, pp. P–III.

[83] C. A. Balanis, Adavnced Enigneering Electromagnetics. John Wiley & Sons, 1999.

[84] ——, Antenna Theory Analysis and Design, 3rd ed. John Wiley & Sons, 2012.

[85] X. Yang and P. Chahal, "On-wafer terahertz ribbon waveguides using polymer-ceramic nanocomposites," IEEE Transactions on Components, Packaging and Manufacturing Technology, vol. 5, no. 2, pp. 245–255, may 2015.

[86] E. S. Rosker, R. Sandhu, J. Hester, M. S. Goorsky, and J. Tice, "Printable materials for the realization of high performance rf components: Challenges and opportunities," International Journal of Antennas and Propagation, vol. 2018, 2018.

[87] J. A. Byford, M. I. M. Ghazali, S. Karuppuswami, B. L. Wright, and P. Chahal, "Demonstration of RF and microwave passive circuits through 3-D printing and selective metalization," IEEE Transactions on Components, Packaging and Manufacturing Technology, vol. 7, no. 3, pp. 463–471, 2017.

[88] K. Y. Park, N. Wiwatcharagoses, and P. Chahal, "Wafer-level integration of micro-lens for THz focal plane array application," in IEEE 63rd Electronic Components and Technology Conference, 2013, pp. 1912–1919.

[89] M. Ghazali, J. Byford, S. Karuppuswami, A. Kaur, J. Lennon, and P. Chahal, "3D Printed Out-of-Plane Antennas for Use on High Density Boards," in Proceedings - Electronic Components and Technology Conference, 2017.

[90] P. I. Deffenbaugh, T. M. Weller, and K. H. Church, "Fabrication and Microwave Characterization of 3-D Printed Transmission Lines," IEEE Microwave and Wireless Components Letters, vol. 25, no. 12, pp. 823–825, 2015.

[91] A. M. Nicolson and G. F. Ross, “Measurement of the Intrinsic Properties of Materials by Time-Domain Techniques,” IEEE Transactions on Instrumentation and Measurement, vol. 19, no. 4, pp. 377–382, 1970.

[92] W. B. Weir, “Automatic Measurement of Complex Dielectric Constant and Permeability at Microwave Frequencies,” Proceedings of the IEEE, vol. 62, no. 1, pp. 33–36, 1974.

[93] L.-F. Chen, C. Ong, C. Neo, V. Varadan, and V. K. Varadan, Microwave electronics: measurement and materials characterization. John Wiley & Sons, 2004.

[94] J. Sheen, “Comparisons of microwave dielectric property measurements by transmission-/reflection techniques and resonance techniques,” Measurement Science and Technology, vol. 20, p. 042001, 2009.

[95] S. Johann, F. William, P. Aurélien, T. Olivier, D. Nicolas, S. Bila, V. Serge, P. Jean-Baptiste, and R.-P. Gramond, “Plastic and metal additive manufacturing technologies for hyperfrequency passive components up to ka band,” in Microwave Conference (EuMC), 2016 46th European. IEEE, 2016, pp. 373–376.

[96] J. A. Byford, C. Oakley, and P. Chahal, “Additively manufactured frequency selective structures on curved surfaces,” in European Microwave Conference (EuMC), 2018 48th. IEEE, 2018.

[97] P. H. Siegel, “Terahertz technology in biology and medicine,” IEEE Microwave Symposium Digest, vol. 3, pp. 1575–1578, 2004.

[98] C. M. Mann, “Fabrication technologies for Terahertz waveguide,” in The Ninety Eight - 1998 Ieee Sixth International Conference on Terahertz Electronics Proceedings, 1996, pp. 46–49.

[99] S. Biber, J. Schur, A. Hofmann, and L.-P. Schmidt, “Design of new passive THz devices based on micromachining techniques,” Physics and Engineering of Microwaves, Millimeter,, pp. 26–31, 2004.

[100] C. Collins, R. Miles, J. Digby, G. Parkhurst, R. Pollard, J. Chamberlain, D. Steenson, N. Cronin, S. Davies, and J. Bowen, “A new micro-machined millimeter-wave and terahertz snap-together\nrectangular waveguide technology,” IEEE Microwave and Guided Wave Letters, vol. 9, no. 2, pp. 63–65, 1999.

[101] J. W. Digby, C. E. McIntosh, G. M. Parkhurst, B. M. Towlson, S. Hadjiloucas, J. W. Bowen, J. Martyn Chamberlain, R. D. Pollard, R. E. Miles, D. Paul Steenson, L. S. Karatzas, N. J. Cronin, and S. R. Davies, “Fabrication and characterization of micromachined rectangular waveguide components for use at millimeter-wave and terahertz frequencies,” IEEE Transactions on Microwave Theory and Techniques, vol. 48, no. 8, pp. 1293–1302, 2000.

[102] W. R. McGrath, C. Walker, M. Yap, and Y. C. Tai, “Silicon Micromachined Waveguides for Millimeter-Wave and Submillimeter-Wave Frequencies,” IEEE Microwave and Guided Wave Letters, vol. 3, no. 3, pp. 61–63, 1993.

[103] B. A. Shenouda, L. W. Pearson, and J. E. Harriss, “Etched-Silicon micromachined W-band waveguides and horn antennas,” IEEE Transactions on Microwave Theory and Techniques, vol. 49, no. 4 I, pp. 724–727, 2001.

[104] J. H. Kim, B. C. Kim, Y. T. Byun, Y. M. Jhon, S. Lee, D. H. Woo, and S. H. Kim, “All-Optical AND Gate Using Cross-Gain Modulation in Semiconductor Optical Amplifiers,” Japanese Journal of Applied Physics, Part 1: Regular Papers and Short Notes and Review Papers, vol. 43, no. 2, pp. 608–610, 2004.

[105] J. A. Hejase, B. Schulte, and P. Chahal, “Design and test of wide-band terahertz dielectric sub-wavelength focusing probes,” Proceedings - Electronic Components and Technology Conference, pp. 1035–1040, 2011.

[106] Y. Cai, F. Sammoura, C.-Y. Chi, L. Lin, and J.-C. Chiao, “Micro hot embossed plastic millimeter-wave systems,” Proceedings of SPIE, pp. 60 350S–60 350S–10, 2005.

[107] K. Y. Park, N. Wiwatcharagoses, C. A. Silveira, and P. Chahal, “Plastic injection micromolding of THz circuits and microfluidic sensors,” Proceedings - Electronic Components and Technology Conference, pp. 1562–1566, 2012.

[108] A. Kaur, J. C. Myers, M. Ifwat, M. Ghazali, J. Byford, and P. Chahal, “Affordable Terahertz Components using 3D Printing,” in Electronic Components and Technology Conference (ECTC) , 2015 IEEE 65th, San Diego, CA, 2015, pp. 2071–2076.

[109] M. I. M. Ghazali, E. Gutierrez, J. C. Myers, A. Kaur, B. Wright, and P. Chahal, “Affordable 3D printed microwave antennas,” in Proceedings - Electronic Components and Technology Conference, 2015, pp. 240–246.

[110] J. D. Joannopoulos, S. G. Johnson, J. N. Winn, and R. D. Meade, Photonic crystals: molding the flow of light. Princeton university press, 2011.

[111] A. Kaur, J. Myers, M. Ghazali, J. Byford, and P. Chahal, “Affordable terahertz components using 3D printing,” in Proceedings - Electronic Components and Technology Conference, vol. 2015-July, 2015.

[112] L. C. A. Silveira, Terahertz photonic crystal microfluidic sensors. Michigan State University. Electrical Engineering, 2014.

[113] D. M. Pozar, Microwave Engineering. John Wiley & Sons, 2009.

[114] M. I. M. Ghazali, S. Karuppuswami, A. Kaur, and P. Chahal, “3-d printed air substrates for the design and fabrication of rf components,” IEEE Transactions on Components, Packaging and Manufacturing Technology, vol. 7, no. 6, pp. 982–989, 2017.

[115] N. Ghassemi and K. Wu, “Planar dielectric rod antenna for gigabyte chip-to-chip communication,” IEEE Transactions on Antennas and Propagation, vol. 60, no. 10, pp. 4924–4928, 2012.

[116] M. Bozzi, a. Georgiadis, and K. Wu, “Review of substrate-integrated waveguide circuits and antennas,” IET Microwaves, Antennas & Propagation, vol. 5, no. 8, p. 909, 2011.

[117] W. M. Abdel-Wahab, D. Busuioc, and S. Safavi-Naeini, "Millimeter-wave high radiation efficiency planar waveguide series-fed dielectric resonator antenna (DRA) array: Analysis, design, and measurements," IEEE Transactions on Antennas and Propagation, vol. 59, no. 8, pp. 2834–2843, 2011.

[118] D. Guha, A. Banerjee, C. Kumar, and Y. M. Antar, "Higher order mode excitation for high-gain broadside radiation from cylindrical dielectric resonator antennas," IEEE Transactions on Antennas and Propagation, vol. 60, no. 1, pp. 71–77, 2012.

[119] A. Perron, T. Denidni, and A.-R. Sebak, "High-Gain Hybrid Dielectric Resonator Antenna for Millimeter-Wave Applications: Design and Implementation," IEEE Transactions on Antennas and Propagation, vol. 57, no. 10, pp. 2882–2892, 2009.

[120] A. Petosa and S. Thirakoune, "Rectangular dielectric resonator antennas with enhanced gain," IEEE Transactions on Antennas and Propagation, vol. 59, no. 4, pp. 1385–1389, 2011.

[121] J. Y. Chung and C. C. Chen, "Two-layer dielectric rod antenna," IEEE Transactions on Antennas and Propagation, vol. 56, no. 6, pp. 1541–1547, 2008.

[122] C. W. Liu and C. C. Chen, "A UWB three-layer dielectric rod antenna with constant gain, pattern and phase center," IEEE Transactions on Antennas and Propagation, vol. 60, no. 10, pp. 4500–4508, 2012.

[123] D. C. Lugo, R. A. Ramirez, J. Castro, J. Wang, and T. M. Weller, "3D printed multilayer mm-wave dielectric rod antenna with enhanced gain," 2017 IEEE Antennas and Propagation Society International Symposium, Proceedings, vol. 2017-Janua, no. July 2018, pp. 1247–1248, 2017.

[124] J. P. Pousi, S. N. Dudorov, D. Lioubtchenko, and A. V. Räisänen, "Dielectric Rod Waveguide Antenna Array Element for Millimeter Waves," in URSI FINNISH XXXI CONVENTION ON RADIO SCIENCE AND ELECTROMAGNETICS 2008 MEETING, 2008.

[125] J. P. Pousi, D. V. Lioubtchenko, S. N. Dudorov, and A. V. Räisänen, "High permittivity dielectric rod waveguide as an antenna array element for millimeter waves," IEEE Transactions on Antennas and Propagation, vol. 58, no. 3, pp. 714–719, 2010.

[126] N. Dolatsha and A. Arbabian, "Wideband Dual-mode Dielectric Waveguide with Applications in Millimeter-wave Interconnects and Wireless Links," in Progress in Electromagnetics Research Symposium Proceedings. Prague, Czech Republic: PIERS, 2015, pp. 203–206.

[127] A. A. Generalov, J. A. Haimakainen, D. V. Lioubtchenko, and A. V. Raisanen, "Wide band mm-and sub-mm-wave dielectric rod waveguide antenna," IEEE Transactions on Terahertz Science and Technology, vol. 4, no. 5, pp. 568–574, 2014.

[128] S. M. Hanham, T. S. Bird, A. D. Hellicar, R. A. Minasian, and Ieee, "Optimized Dielectric Rod Antennas for Terahertz Applications," 2009 34th International Conference on Infrared, Millimeter, and Terahertz Waves, Vols 1 and 2, pp. 872–873, 2009.

[129] S. M. Hanham, T. S. Bird, B. F. Johnston, A. D. Hellicar, R. A. Minasian, and Ieee, “A 600 GHz Dielectric Rod Antenna,” 2009 3rd European Conference on Antennas and Propagation, Vols 1-6, pp. 1565–1567, 2009.

[130] N. Klein, P. Lahl, U. Poppe, F. Kadlec, and P. Kužel, “A metal-dielectric antenna for terahertz near-field imaging,” Journal of Applied Physics, vol. 98, no. 1, pp. 1–5, 2005.

[131] S. Kobayashi, R. Mittra, and R. Lampe, “Dielectric tapered rod antennas for millimeter-wave applications,” IEEE Transactions on Antennas and Propagation, vol. 30, no. 1, pp. 54–58, 1982.

[132] D. V. Lioubtchenko, S. N. Dudorov, J. A. Mallat, and A. V. Räisänea, “Dielectric rod waveguide antenna for W band with good input match,” IEEE Microwave and Wireless Components Letters, vol. 15, no. 1, pp. 4–6, 2005.

[133] R. Kazemi and A. Fathy, “Dielectric rod antenna with substrate integrated waveguide planar feed for wide band applications,” IEEE Antennas and Propagation Society, AP-S International Symposium (Digest), pp. 12–13, 2012.

[134] J. H. Qiu and N. N. Wang, “Optimized dielectric rod antenna for millimeter wave FPA imaging system,” in 2009 IEEE International Workshop on Imaging Systems and Techniques, IST 2009 - Proceedings, 2009, pp. 151–154.

[135] K. Y. Park, A THz Focal Plane Imaging Array using Metamaterial-inspired Bolometer and Wafer-level Integrated Focusing Elements. Michigan State University. Electrical Engineering, 2014.

[136] A. J. L. Adam, “Review of near-field Terahertz measurement methods and their applications: How to achieve sub-wavelength resolution at THz frequencies,” Journal of Infrared, Millimeter, and Terahertz Waves, vol. 32, no. 8-9, pp. 976–1019, 2011.

[137] Z. Chen, W. Hong, and J. X. Chen, “High-Q planar active resonator based on substrate integrated waveguide technique,” Electronics Letters, vol. 48, no. 10, p. 575, 2012.

[138] A. J. Huber, F. Keilmann, J. Wittborn, J. Aizpurua, and R. Hillenbrand, “Terahertz Near-Field Nanoscopy of Mobile Carriers in Single Semiconductor Nanodevices,” Nano Letters, vol. 8, no. 11, pp. 3766–3770, 2008.

[139] J. A. Deibel, K. Wang, M. D. Escarra, and D. M. Mittleman, “Enhanced coupling of terahertz radiation to cylindrical wire waveguides,” Optics Express, vol. 14, no. 1, pp. 511–518, 2006.

[140] K. Wang and D. M. Mittleman, “Guided propagation of terahertz pulses on metal wires,” NATO Science for Peace and Security Series B: Physics and Biophysics, vol. 22, no. 9, pp. 55–68, 2007.

[141] O. Mitrofanov, C. Renaud, and A. Seeds, “Terahertz probe for spectroscopy of sub-wavelength objects,” Optics Express, vol. 20, no. 6, pp. 6197–6202, 2012.

[142] F. Keilmann, B. Knoll, and A. Kramer, “Long-Wave-Infrared Near-Field Microscopy,” physica status solidi (b), vol. 215, no. 1, pp. 849–854, 1999.

[143] M. A. Seo, A. J. L. Adam, J. H. Kang, J. W. Lee, K. J. Ahn, Q. H. Park, P. C. M. Planken, and D. S. Kim, "Near field imaging of terahertz focusing onto rectangular apertures," Opt. Express, vol. 16, no. 25, pp. 20 484–20 489, 2008.

[144] M. A. Seo, H. R. Park, S. M. Koo, D. J. Park, J. H. Kang, O. K. Suwal, S. S. Choi, P. C. Planken, G. S. Park, N. K. Park, Q. H. Park, and D. S. Kim, "Terahertz field enhancement by a metallic nano slit operating beyond the skin-depth limit," Nature Photonics, vol. 3, no. 3, pp. 152–156, 2009.

[145] H. R. Park, Y. M. Park, H. S. Kim, J. S. Kyoung, M. A. Seo, D. J. Park, Y. H. Ahn, K. J. Ahn, and D. S. Kim, "Terahertz nanoresonators: Giant field enhancement and ultrabroadband performance," Applied Physics Letters, vol. 96, no. 12, pp. 98–101, 2010.

[146] S. Hunsche, M. Koch, I. Brener, and M. Nuss, "THz near-field imaging," Optics Communications, vol. 150, no. 1, pp. 22–26, 1998.

[147] T. I. Kuznetsova, V. S. Lebedev, and a. M. Tsvelik, "Optical fields inside a conical waveguide with a subwavelength-sized exit hole," Journal of Optics A: Pure and Applied Optics, vol. 6, pp. 338–348, 2004.

[148] A. Basu and T. Itoh, "A New Field-Probing Technique For Millimeter-wave Components," in IEEE MTT-S International Microwave Symposium Digest, 1997, pp. 1667–1670.

[149] P. Chahal, J. A. Hejase, S. Shane, K. Y. Park, A. Kaur, and J. Byford, "Millimeter wave and terahertz dielectric probe microfluidic sensors," in International Conference on Infrared, Millimeter, and Terahertz Waves, IRMMW-THz, 2014.

[150] E. Kume and S. Sakai, "Properties of a dielectric probe for scanning near-field millimeter-wave microscopy," Journal of Applied Physics, vol. 99, no. 5, p. 056105, 2006.

[151] ——, "Millimeter-wave radiation from a Teflon dielectric probe and its imaging application," Measurement Science and Technology, vol. 19, no. 11, p. 115501, 2008.

[152] M. D. Weiss, B. Zadler, S. Schafer, and J. Scales, "Near field millimeter wave microscopy with conical Teflon probes," Journal of Applied Physics, vol. 106, no. 4, 2009.

[153] J. Myers, A. Kaur, J. Byford, and P. Chahal, "Investigation of Modulation-Capable Silicon Waveguides for Efficient On-Wafer Terahertz Interconnects," in Proceedings - Electronic Components and Technology Conference, 2015.

[154] W. L. Chan, K. Charan, D. Takhar, K. F. Kelly, R. G. Baraniuk, and D. M. Mittleman, "A single-pixel terahertz imaging system based on compressed sensing," Applied Physics Letters, vol. 93, no. 12, p. 121105, 2008.

[155] Y. C. Shen, L. Gan, M. Stringer, a. Burnett, K. Tych, H. Shen, J. E. Cunningham, E. P. J. Parrott, J. a. Zeitler, L. F. Gladden, E. H. Linfield, and a. G. Davies, "Terahertz pulsed spectroscopic imaging using optimized binary masks," Applied Physics Letters, vol. 95, no. 23, p. 231112, 2009.

[156] Z. Zhang and T. Buma, "Terahertz Impulse Imaging With Sparse Arrays and Adaptive Reconstruction," IEEE Journal of Selected Topics in Quantum Electronics, vol. 17, no. 1, pp. 169–176, jan 2011.

[157] Z. Liu, K. Su, D. E. Gary, J. F. Federici, R. B. Barat, and Z.-H. Michalopoulou, "Video-rate terahertz interferometric and synthetic aperture imaging," Applied Optics, vol. 48, no. 19, p. 3788, jun 2009.

[158] Z. Taylor, R. Singh, E. Brown, J. Bjarnason, M. Hanson, and a.C. Gossard, "Analysis of Pulsed THz Imaging Using Optical Character Recognition," IEEE Sensors Journal, vol. 9, no. 1, pp. 3–8, jan 2009.

[159] N. van der Valk and P. Planken, "Measurement of THz Spot Sizes with a $\lambda$ / 200 Diameter in the Near-Field of a Metal Tip," Journal of Biological Physics, vol. 29, no. 2-3, pp. 239–245, 2003.

[160] T. Löffler, K. Siebert, S. Czasch, T. Bauer, and H. G. Roskos, "Visualization and classification in biomedical terahertz pulsed imaging." Physics in Medicine and Biology, vol. 47, no. 21, pp. 3847–3852, 2002.

[161] T. Löffler, T. Bauer, K. Siebert, H. Roskos, A. J. Fitzgerald, and S. Czasch, "Terahertz dark-field imaging of biomedical tissue." Optics Express, vol. 9, no. 12, pp. 616–621, 2001.

[162] N. C. J. van der Valk, W. a. M. van der Marel, and P. C. M. Planken, "Terahertz polarization imaging," Optics Letters, vol. 30, no. 20, pp. 2802–2804, 2005.

[163] B. R. Crowgey, "Rectangular waveguide material characterization: anisotropic property extraction and measurement validation," Doctoral, Michigan State University, 2013.